AN EXPERIMENTAL STUDY OF VIBRATIONS IN THE GERBIL MIDDLE EAR UNDER STATIC PRESSURE

Department of BioMedical Engineering
McGill University
Montréal, Québec

April 2014

A thesis submitted to McGill University in partial fulfillment of the requirements of the degree of

Master of Engineering

ABSTRACT / RÉSUMÉ

The Mongolian gerbil has become widely used in middle-ear research, because it is low in cost and its middle-ear structures are relatively accessible. This study presents the effects of static pressurization on the vibration response of the gerbil eardrum. A single-point laser Doppler vibrometer is used to acquire frequency responses in eight *post mortem* gerbil ears. Magnitudes of vibration are normalized with respect to sound pressure level measured near the eardrum and are presented over the range of 0.2 to 10 or 11 kHz. In each gerbil, measurements on the manubrium and on the pars tensa are presented using one of two pressurization protocols. For the unpressurized measurements the inter-specimen variability was small and measurements were more or less repeatable from cycle to cycle. Pressurized responses exhibited magnitude reductions at lower frequencies, then rose to a peak and exhibited sharp features at higher frequencies. As pressure increased, magnitudes decreased and the peak was shifted to higher frequencies. The eardrum break-up frequency was shifted beyond the frequency range of our measurements. On the manubrium we did not observe any viscoelastic or temporal changes. On the pars tensa, changes were observed from cycle to cycle but the reasons are not clear. Our results are compared with previous data in the literature. Understanding the vibration response of the eardrum to pressurization, as well as the roles of viscoelastic and temporal effects, will lead to a better understanding of clinical tympanometry, which is particularly important in infants where the response to tympanometry is not well understood.

La gerbille de Mongolie est devenu de plus en plus utilisée dans la recherche de l'oreille moyenne, parce qu'elle n'est pas trop coûteuse et les structures sont assez facilement accessibles. Cette étude présente les effets de la pression statique sur la réponse de vibration du tympan de la gerbille. Un vibromètre à laser Doppler est utilisé pour acquérir des réponses fréquentielles dans huit oreilles de gerbille. Les amplitudes de vibration sont normalisés par le niveau de pression acoustique mesuré à proximité du tympan, et sont présentés sur la gamme de fréquence de 0.2 à 10 ou 11 kHz. Dans chaque gerbille, des mesures sur le manubrium et sur le pars tensa sont présentés en utilisant un des deux protocoles de pressurisation. Pour les mesures sans pression la variabilité entre les gerbilles était petit et les mesures sont plus ou moins reproductible d'un cycle à l'autre. Les mesures sous pression présentaient des réductions d'amplitude à des fréquences inférieures, puis ont augmenté à un sommet et présentaient des caractéristiques pointues à des fréquences plus élevées. Lorsque la pression a augmenté, les amplitudes ont diminué et le sommet a été déplacé aux fréquences plus élevées. Le fréquence « break-up » du tympan a été déplacé au-delà de la gamme de fréquence de nos mesures. Sur le manubrium nous n'avons pas observé de changements temporels ou viscoélastique. Sur le pars tensa, des changements ont été observés d'un cycle à l'autre, mais les raisons ne sont pas claires. Nos résultats sont comparés avec des études précèdent dans la littérature. Comprendre la réponse du tympan aux vibrations sous pressurisation, ainsi que les rôles des effets viscoélastique et temporels, conduira à une meilleure compréhension de la tympanométrie clinique, qui est particulièrement important chez les nouveau-nés où la réponse à la tympanométrie n'est pas bien comprise.

ACKNOWLEDGEMENTS

TABLE OF CONTENTS

CHAPTER 1
INTRODUCTION

1.1 Background and motivation

Hearing loss is defined as the complete or partial inability to perceive sound in one or both ears. Research from the Hearing Foundation of Canada indicates that ten percent of the Canadian population is affected by hearing loss (www.thfc.ca, retrieved 2012 May 1). It is ranked the fastest growing and third largest chronic disability in Canada, behind arthritis and hypertension. Hearing loss is also one of the most common birth defects, given that approximately 3 to 4 in 1000 children are born with some level of hearing loss that requires medical attention (e.g., Akinpelu et al. 2014). It is recommended that hearing loss be identified as soon as one month after birth, so that a proper diagnosis can be made by three months of age (Joint Committee on Infant Hearing 2007). Otherwise, even a mild uncorrected loss can seriously delay language development, resulting in subsequent behavioural or educational difficulties. Newborn hearing screening can quickly detect hearing loss in newborns using non-invasive and relatively inexpensive tests. Historically, babies were screened for hearing loss only if certain high-risk factors were evident. However, Universal Newborn Hearing Screening (UNHS) is becoming the standard of care in many countries worldwide. In Canada, it has been mandated in many provinces, most recently in Québec. Without screening, the average age of detection of hearing loss in infants is just under 3 years old, well past the critical stage for the development of social skills and speech (www.thfc.ca, retrieved 2012 May 1).

The middle ear plays a significant role in hearing, often being the site of infections, congenital disorders, and other pathologies that result in hearing loss. A better understanding of middle-ear mechanics will allow for advances in the diagnosis and treatment of middle-ear abnormalities that contribute to hearing loss. For this reason, many research groups have studied mammalian middle ears, in particular gerbils. Gerbils are advantageous as they have relatively large eardrums for their body size, with an easily

approachable middle ear, and are low in cost.

Experimental studies and mathematical modelling techniques complement one another in developing a quantitative understanding of middle-ear mechanics. In order to make experimental measurements, laser Doppler vibrometry (LDV) is a very popular method that allows for the real-time acquisition of velocity and displacement vibration measurements of the middle ear. The use of LDV has been used in animal subjects such as gerbils and cats by several groups (e.g., Decraemer et al. 2007; Ravicz et al. 2008; Maftoon et al. 2013). Other studies discuss the use of LDV in human cadavers as well the possible diagnostic applications of LDV (e.g., Whittemore Jr. et al. 2004; Rosowski et al. 2008). Some of these studies are discussed in Chapter 3.

1.2 Research objectives

The research reported here forms part of a research programme which has as a goal an improved understanding of tympanometry, a promising clinical tool that relies on a combination of sounds and static pressures to assess middle-ear function. The gerbil middle ear will be characterized by exposing the gerbil eardrum and acquiring LDV measurements at various points on the eardrum in the presence of static pressure. The resulting frequency response functions give insight into the mechanics of the middle-ear system. The specific goals of this work were as follows:

1. Make a number of improvements to the mechanical and electrical components of an existing pressurization device.

2. Generate a new design for an acoustic coupler to be used in the experimental measurements. The coupler establishes a closed sound chamber between the sound source and the ear. The new design aims to reduce laser-beam reflections, provide a better view of the eardrum, and be easy to remove and replace during experiments.

3. Perform eardrum vibration measurements on the gerbil middle ear in the presence of static pressures, using the pressurization device and new acoustic coupler from points 1 and 2. The static pressure and the acoustic stimuli are comparable to those of tympanometry.

1.3 Thesis plan

Chapter 2 of the thesis is a basic overview of hearing, the auditory system, and the mechanics of the middle ear. Chapter 3 consists of a review of previous studies related to the present work. The methods and materials used are presented in Chapter 4, followed by results and a discussion in Chapter 5. A summary of the work and a discussion of possible future work are presented in Chapter 6.

CHAPTER 2
THE AUDITORY SYSTEM

2.1 Introduction

In this chapter the auditory system is discussed . An overview of the basics of hearing physiology and the perception of sound is presented in Section 2.2. The anatomy of the human middle ear is discussed in Section 2.3, and the anatomy of the gerbil middle ear is discussed in Section 2.4 with emphasis on differences from the human ear. Finally, the mechanics of the middle ear are presented in Section 2.5.

2.2 Overview of hearing

Sound is generated by the mechanical vibrations of an object, such as the human vocal cords. As the sound source vibrates, it stimulates displacements of the particles of the surrounding medium and the particle displacements propagate, causing the sound to travel through the medium.

The general anatomy of the human ear is shown in Figure 2.1. The outer ear consists of the externally visible portion (pinna) as well as the auditory canal. The middle ear is an air-filled compartment, also known as the tympanic cavity, which is bounded by the eardrum and contains a chain of the three smallest bones in the body (ossicles), namely the malleus, incus and stapes. The inner ear includes the vestibular system and the cochlea, which are both filled with liquid. The function of the vestibular system is related to the perception of gravity and acceleration while the function of the cochlea is related to hearing.

The propagating sound waves reach the pinna, which has a number of curves and folds that help in the perception of the direction from which sounds are coming. The waves are propagated through the external ear canal and strike the thin tympanic membrane, more commonly referred to as the eardrum. The pressure waves cause the eardrum to vibrate.

The vibrations are mechanically transferred across the middle ear by means of the three ossicles. The stapes exhibits a more or less piston-like motion in the oval window, sending waves into the liquid of the inner ear. This movement of liquid induces a motion of hair cells inside the cochlea, resulting in the generation of electrical signals, or action potentials, that are sent along the cochlear nerve and travel to the brain.
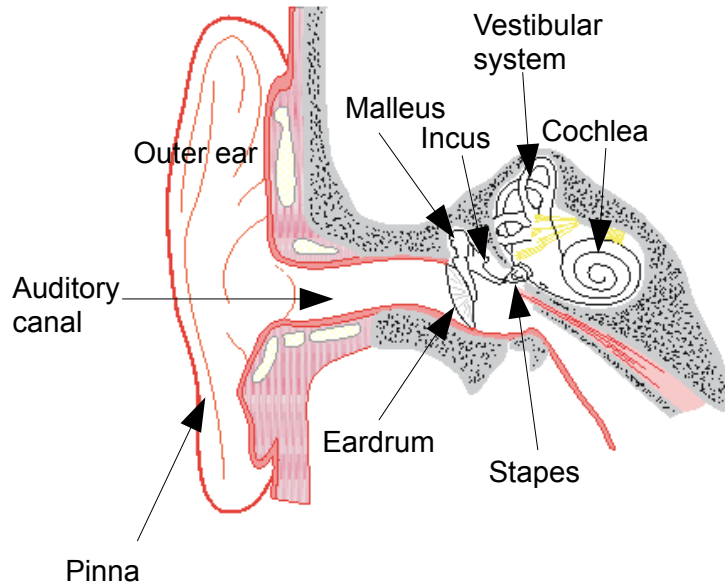
Figure 2.1: General anatomy of the human ear
(After http://audilab.bme.mcgill.ca/Audilab/teach/me_saf/me_saf.html,
retrieved 2013 Aug 1)

2.3 Human middle ear

2.3.1 Eardrum

The eardrum separates the tympanic cavity from the external auditory canal. It is roughly conical in shape with the umbo located at the apex of the cone, which points towards the inner ear. The umbo is often used as a landmark for eardrum vibration measurements, as will be seen in later chapters. The eardrum consists of a pars tensa and a pars flaccida. As shown in Figure 2.2, the pars tensa occupies most of the eardrum, and the pars flaccida is the remaining small portion that is located superior to the pars tensa. The manubrium, or

handle, of the malleus is attached to the eardrum and therefore provides a coupling of the eardrum to the ossicles.

Using fluorescence images taken perpendicularly through human eardrums with a confocal microscope, Kuypers et al. (2006) found that the mean thickness at the umbo varied between 40 and 120 μm. The maximum thickness of the eardrum is observed at its periphery, and the edge of the membrane is continuous with the fibrocartilaginous ring, which in turn is attached to the tympanic annulus (part of the temporal bone).
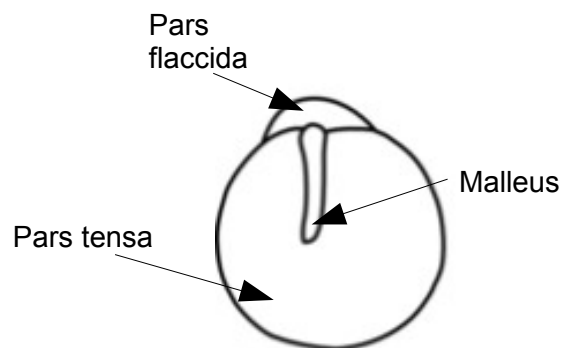
Figure 2.2: Human eardrum
(After http://audilab.bme.mcgill.ca/AudiLab/teach/me_saf/me_saf.html,
retrieved 2013 Aug 1)

As shown in Figure 2.3 the pars tensa is composed of multiple layers, including a mucosal layer on the medial side, an intermediate lamina propria, and an epidermal layer on the lateral side (e.g., Lim 1968). The lamina propria is made up of four layers: two outer layers of connective tissue, a layer of radial fibres that radiate away from the manubrium and a layer of circular fibres organized more or less concentrically about the umbo. Although it is thicker than the pars tensa, the pars flaccida lacks the layers of organized fibres and is therefore more flaccid.
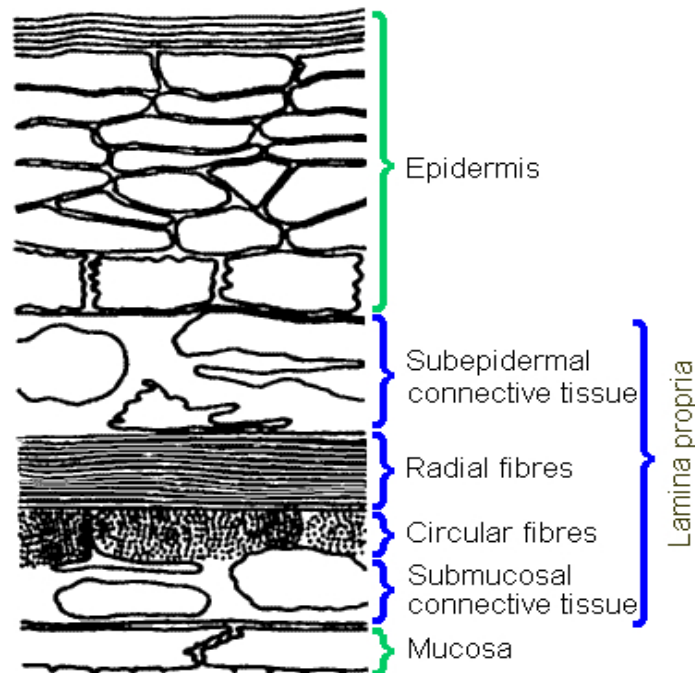
Figure 2.3: Pars flaccida layers
(Source: http://audilab.bme.mcgill.ca/~funnell/AudiLab/tech/me_saf/me_saf.html,
retrieved 2013 Aug 1)

2.3.2 Ossicles

The malleus, shown in Figure 2.4, is named after its supposed resemblance to a hammer. It is made up of a head, neck and and three processes: the lateral process, the anterior process and the manubrium. The head is the large, oval-shaped upper part the malleus, articulating with the incus. The manubrium projects inferiorly from the neck. The lateral process is a small projection from the superior end of the manubrium. Both the lateral process and the inferior tip of the manubrium are tightly connected to the eardrum.

The incus, also shown in Figure 2.4, is named after its supposed resemblance to an anvil and consists of a body and two processes. The body articulates with the head of the malleus. The short process projects horizontally and is approximately conical in shape while the long process projects vertically, more or less parallel to the manubrium, with a rounded lenticular process at its tip that articulates with the stapes. The short and long

processes are approximately at right angles to one another.

The stapes, also shown in Figure 2.4, is named after its resemblance to a stirrup. It consists of a head, neck, base and two crura. The head articulates with the lenticular process at the end of the incus. The two crura diverge from the neck and connect at either end of the flat oval base (footplate), which is attached to the oval window by an annular ligament.
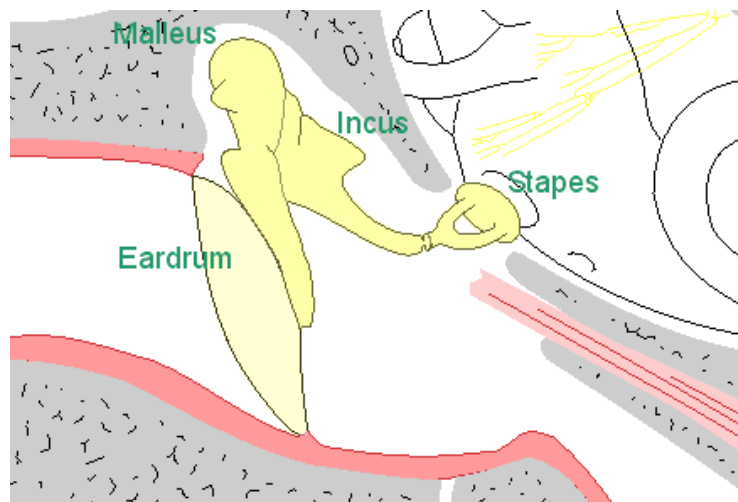
Figure 2.4: Human middle ear. Eardrum and ossicles are labelled.
(Source: http://audilab.bme.mcgill.ca/AudiLab/teach/me_saf/me_saf.html,
retrieved 2013 Aug 1)

2.3.3 Other middle-ear structures

Other structures in the middle ear such as ligaments, joints and muscles are important contributors to the transfer of sound. Two synovial joints are responsible for the articulations of the middle-ear ossicles with one another.

The ossicles are secured to the tympanic cavity walls by a number of ligaments. In humans, the malleus is suspended by an anterior, a superior and a lateral ligament. The incus is attached to the tympanic cavity wall by a posterior and a superior ligament. The annular ligament of the stapes provides its connection to the oval window.

The tensor tympani and stapedius are two muscles located in the middle ear. The larger tensor tympani is contained within the anterior wall of the tympanic cavity, and its tendon is secured to a portion of the neck of the malleus as well as to the manubrium. The stapedius is the smallest muscle in the human body. Its tendon extends to the posterior portion of the neck of the stapes. Both muscles work together to reduce the response of the middle ear (e.g., Borg & Counter 1989). While chewing, for example, the muscles contract and reduce the vibrations of the ossicles. In addition to these two striated muscles, smooth-muscle fibres have been found in the fibrocartilaginous ring (Kuypers et al. 1999; Yang & Henson Jr. 2002). It has been suggested that these fibres may "regulate tympanic membrane tension and control blood flow" (Yang & Henson Jr. 2002).

The tympanic cavity is anatomically divided into three sections: the epitympanum, the mesotympanum, and the hypotympanum. The epitympanum (attic) is the superior part of the cavity, containing the head of the malleus and the body of the incus. Situated medial to the eardrum, the mesotympanum contains parts of the malleus and incus, and the stapes. The hypotympanum is inferior to the eardrum and is the site of the opening to the Eustachian tube, which functions to regulate the pressure within the middle ear and to permit drainage of liquids.

2.4 Gerbil middle ear

The use of animals in research is advantageous for a number of reasons: animals are fresher than human cadavers; the use of animals allows for a variety of experimental approaches such as invasive surgery; and there is less inter-subject variability than in humans. Over the last few decades, Mongolian gerbils (*Meriones unguiculatus*) have become increasingly popular in auditory research (e.g., von Unge et al. 1991; Ravicz et al. 1992; Zheng et al. 1997; Dirckx et al. 1998; Rosowski et al. 1999; Dong & Olson 2006; Elkhouri et al. 2006; Maftoon et al. 2013). Gerbils are excellent candidates for this field of research because they are low in cost and have easily approachable middle-ear structures and relatively large

eardrums for their size.

The anatomy and function of the middle ear is generally similar in gerbils and humans, although they differ considerably in size. The gerbil middle ear is encased by an inflated bony shell called the bulla. Békésy (1949) measured the volume of the human middle-ear space to be approximately 2 cm^3. The air space within the gerbil bulla occupies a volume of approximately 0.2 cm^3, much larger than other rodents of similar body size such as rats (Ravicz et al. 1992). The enlarged bulla increases sensitivity to sounds below a frequency of about 3 kHz. This feature is common in many smaller desert animals, facilitating the detection of frequencies produced by approaching predators (Rosowski et al. 1999). Another specialization of the gerbil middle ear is that the eardrum has a relatively large pars flaccida. The pars flaccida to pars tensa surface-area ratio is estimated to be 0.11, much larger than its value of 0.027 in humans (Teoh et al. 1997). Although the function of the pars flaccida is unclear, it has been observed that an elevated surface-area ratio in the gerbil contributes to reduced sensitivity to sounds below 500 Hz (Rosowski et al. 1999).

2.5 Mechanics of the middle ear

2.5.1 Rotation of the incudomallear complex

Helmholtz (1868) suggested that the incudomallear (malleus-incus) complex of the middle ear rotates about an axis that involves both the anterior mallear ligament (AML) and the posterior incudal ligament (PIL). Later, Békésy (1960) concluded that this model with a single axis of rotation is only valid at low frequencies, where mass effects are negligible. At higher frequencies the motion becomes more complex. A number of studies have investigated this motion, concluding that the complications include bending of the manubrium, a shift in the axis of rotation, and changes in the relative motion between the incus and the malleus. (e.g., Decraemer et al. 1991).

2.5.2 Middle-ear impedance-matching mechanisms

The role of the middle ear as an acoustical impedance-matching system is extremely important. Acoustical impedance Z is defined by

$$Z = \frac{P}{U}$$
(Equation 2.1)

where P is the sound pressure and U is the volume velocity. Acoustical admittance is defined as the inverse of impedance. The acoustical impedance of the air in the middle ear is very different from the impedance of the liquid in the cochlea. As the sound travels from air to liquid, the waves are partially reflected due to the difference between the acoustical impedances of the two media. For instance, the high impedance ratio of an air-water boundary means that only 0.1% of sound energy is transmitted to the liquid, most of the energy being reflected back from the boundary (e.g., Wever et al. 1948). The middle ear is designed as a transformer mechanism to reduce the sound energy lost between the middle ear and the cochlea. Three mechanical factors that contribute to the operation of the transformer mechanism include an eardrum-to-footplate surface-area ratio, an ossicular lever ratio and the curvature of the eardrum. These factors are discussed in the following sections, but because they are closely related it is difficult to separate their effects (Funnell 1996).

2.5.2.1 Surface-area ratio

The pressure P exerted by a force F directed perpendicularly onto a surface of area A is given by the ratio

$$P = \frac{F}{A} \quad .$$
(Equation 2.2)

The surface-area ratio is the primary contributor to the transformer mechanism. As sound waves travel towards the inner ear, equal and opposite forces are imposed on the surface of

the eardrum and on the footplate of the stapes. When the same force acts on two surfaces with different sizes, the pressure is multiplied by the ratio of the two surface areas. Due to the surface-area ratio between the larger eardrum and smaller stapes footplate, the pressure is larger at the footplate. Many groups have investigated these surface-area ratios: in gerbils, the ratio was calculated by (Lay 1972) to be 27.6. The ratio was estimated to be between 15 and 26 in humans (Wever & Lawrence 1954; Békésy 1960). However, only the effective area (defined as the fraction of the eardrum that is effectively coupled to the ossicles) contributes to sound transmission to the cochlea. The contribution of the whole eardrum to the transformer ratio depends on the displacement distribution (e.g., Funnell 1996). Another complication is the question of whether to use the area circumscribed by the more or less planar circumference of the eardrum or to use the actual 3-D surface area (Hunt & Korth 1980).

2.5.2.2 Ossicular lever ratio

Assuming a fixed axis of rotation as mentioned above, and assuming that the sound pressure acts at the umbo, the ossicular lever ratio is considered to be a second contributor to the effectiveness of the transformer mechanism. It is defined as the ratio between (1) the orthogonal distance from the umbo to the axis of rotation, and (2) the orthogonal distance from the axis of rotation to the lenticular process of the incus. The ratio has been calculated to be approximately 1.3 for humans (Koike et al. 2002) and 3.3 for gerbils (Lay 1972).

2.5.2.3 Eardrum curvature

A final contributor to the transformer mechanism is the curvature of the eardrum and its corresponding amplification of sound pressure. The theory was first proposed by Helmholtz (1868), who attributed an increased force at the umbo to the curvature, and attributed the curvature to the organization of the fibres. Based on a finite-element model, Funnell (1996) was able to investigate a number of issues regarding the displacements of the cat eardrum. He demonstrated that certain regions of the eardrum produce greater driving forces on the

manubrium than other regions, in part due to the curvature of the membrane. The contribution of eardrum curvature to the transformer mechanism is the least important of the three factors discussed here.

CHAPTER 3
PREVIOUS STUDIES

3.1 Introduction

A variety of experimental measurement techniques have been used to study middle-ear mechanics in both *post mortem* and live ears. Our research entails the *post mortem* study of eardrum vibrations in gerbils in the presence of static pressure in the middle ear. A review of the previous studies pertinent to our research is presented in this chapter. In Section 3.2, a review of human studies and other non-gerbil studies is presented. A review of experimental studies conducted on the gerbil eardrum using only sound pressure as the stimulus is presented in Section 3.3. Studies that also used static pressures are presented in Section 3.4, and a review of studies involving pressurized vibration measurements are presented in Section 3.5. A brief summary is given in Section 3.6.

3.2 Non-gerbil studies

3.2.1 Introduction

A comprehensive review of experimental observations of normal eardrum vibrations was presented by Funnell & Laszlo (1982). The review includes work as far back as 1874, when visual observations of eardrum displacements were first reported by Kessel in human cadaver ears, using a magnifying lens with applied variations of static pressure. More recently, groups have used optical interferometric techniques to visualize and quantify the vibration patterns of the eardrum. One such technique, used by several groups, is laser Doppler vibrometry (LDV). Further discussed in Chapter 4, LDV permits vibration velocity and displacement measurements over a broad range of frequencies. In this section, we present studies of eardrum vibrations and ossicular motions in non-gerbil species. The studies incorporate a variety of techniques, including LDV.

3.2.2 Eardrum vibration patterns

After Kessel (1874), techniques used in early studies included stroboscopic illumination, high-speed cinematography and mechanical probes. As suggested by Kessel (1874), Dahmann (1929) fixed a number of tiny mirrors to the surface of human cadaver eardrums, calculating the motion of the mirror based on the angle of reflection of a beam of light. Békésy (1941) used a capacitive probe to map magnitudes of vibration over the surface of the human eardrum, and Manley & Johnstone (1974) used the Mössbauer technique with a very small gamma-ray source at various locations of the guinea-pig eardrum. Since then, optical interferometric techniques have become the primary means of investigating eardrum vibration patterns. Time-averaged laser holography is one such method that was used by Tondorf & Khanna (1972) to characterize vibrations of the human eardrum in the range of 0.4 to 6 kHz. The technique is based on holographic interference, "producing dark and bright lines that define iso-amplitude contours of vibration" (Tondorf & Khanna 1972). They observed that the contours at low frequencies showed a maximum magnitude of vibration in the posterior region and another maximum of lower magnitude just anterior to the manubrium. At higher frequencies, the contours appeared to break up into sectional zones of vibration that increased in complexity as the frequency increased. In a similar study performed in cats, Tondorf & Khanna (1972) concluded that the transition from simple to complex vibration patterns occurred at approximately the same frequency as in human ears. These results were confirmed by Decraemer et al. (1989) in their study of the vibration pattern of the cat eardrum with a homodyne laser interferometer.

LDV measurements in 7 rats at multiple locations on the eardrum and the manubrium were reported by our group (Akache et al. 2007). They observed simple vibration patterns of the eardrum up to about 6 or 7 kHz, with magnitudes of vibration that were smallest at the manubrium and largest in the posterior regions of the eardrum. Rosowski et al. (2009) used computer-assisted opto-electronic holography to measure the eardrum vibration patterns in four specimens: cadaveric human, cadaveric chinchilla, live chinchilla and cadaveric cat. Time-averaged holograms were produced for each specimen, allowing for fast characterization of frequency-dependent eardrum vibration patterns at frequencies as high as 25 kHz. At the lowest frequencies, a fairly simple vibration pattern was observed in each species. At higher frequencies the specimens show a "transition from complex to ordered patterns where a large number of local displacement maxima are orderly arranged on the membrane surface." The same group later extended their method to include phase measurements using stroboscopy (Cheng et al. 2010) and eardrum shape measurements using two laser wavelengths (Rosowski et al. 2013).

3.2.3 Ossicular motion

As mentioned is Section 2.3.3, the motion of the incudo-mallear complex was traditionally described as a simple rigid rotation about a fixed axis, becoming more complex at higher frequencies. Using time-averaged holography on human cadaver temporal bones, Gundersen & Høgmoen (1976) observed that the ossicular chain moves like a lever around a frequency-dependent axis of rotation. Later, Gyo et al. (1987) noted a dependence of the lever ratio on frequency that they attributed to translational movements of the rotational axis. Decraemer et al. (1991) used heterodyne laser interferometry to investigate the motion of the malleus in anaesthetized cats. Vibrations were measured at four points along the manubrium, and reflectivity was improved by placing glass micro beads at each point. The frequency responses from one experiment are shown in Figure 3.1. Below 8 kHz, the magnitude at the bead located on the umbo was highest and all four points vibrated nearly in phase, but the pattern changed at higher frequencies. They concluded that the "malleus
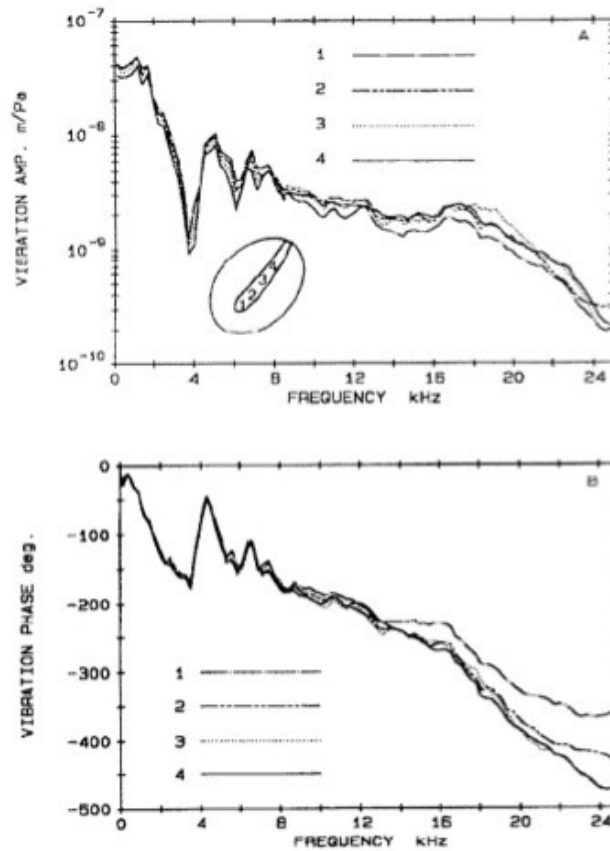
Figure 3.1: Frequency responses at 4 points along the
manubrium measured by Decraemer et al. (1991). Line styles at
each measurement location are shown in the upper panel.

vibration at some frequencies is purely translational, it is rotational at others and mixed at
most" and that even with rotational motion there can be large shifts in the position of the
rotational axis with frequency. They also suggested a possible bending of the tip of the
manubrium at higher frequencies. From the simulation results of a finite-element model
that included manubrial thickness data from histological sections, Funnell et al. (1992)
provided theoretical evidence for bending of the manubrial tip. Using a more sophisticated
experimental setup, Decraemer & Khanna (1994) measured 3-D vibrations at the umbo.
They observed that the motion of the manubrial tip followed an elliptical path that varied in
shape and inclination with frequency. Later, Decraemer et al. (1994) measured the 3-D
motion of the malleus at multiple points on the manubrium and confirmed a frequency-

dependent mix of rotational and translational motion. Their results again suggested a bending of the tip of the manubrium, and further investigations by Decraemer et al. (1995) demonstrated that bending does occur at both low and high frequencies. Decraemer & Khanna (1997) continued their investigation of manubrial motion with 3-D measurements at multiple points along the cat manubrium. They concluded that "the instantaneous axis of rotation changes within each cycle of oscillation and the pattern of change is different for each frequency".

3.2.4 Eardrum viscoelasticity

The viscoelasticity of the eardrum was discussed by Decraemer et al. (1980), demonstrating that, like many other soft biological tissues, the eardrum exhibits viscoelastic behaviour upon deformation. They applied sinusoidal stimuli (0.01 to 100 Hz) to strips of eardrum and measured response phases indicative of viscoelasticity.

Fung discussed the viscoelasticity of soft tissue in terms of two phenomena: hysteresis and preconditioning. If a piece of tissue is subjected to cyclic loading, then the "stress-strain relationship in the loading process is usually somewhat different from that in the unloading process, and the phenomenon is called hysteresis" (Fung 1996, p. 41). The stress-strain curves from repeated cyclic loading typically change from cycle to cycle, with the differences between successive cycles decreasing and eventually disappearing, at which point "the specimen is said to have been preconditioned" (Fung 1996, p. 261).

Cheng et al. (2007) performed uniaxial tensile, stress relaxation, and failure tests on specimens taken from human cadaver eardrums under quasistatic loading conditions. They cut a rectangular strip from the posterior side of the eardrum, clamped it at both ends and mounted it in the material testing system. Curves of stress vs. stretch ratio for three eardrum specimens are shown in Figures 3.2. The hysteresis phenomenon was observed in all three specimens, with the unloading curve being lower than the loading curve. Repeated cycles of load-displacement curves of three eardrum specimens are presented in Figure 3.3. The

phenomenon of preconditioning is observed, with the curves decreasing during repeated
loading-unloading cycles, and with a more or less steady pre-conditioned state observed by
the third cycle.
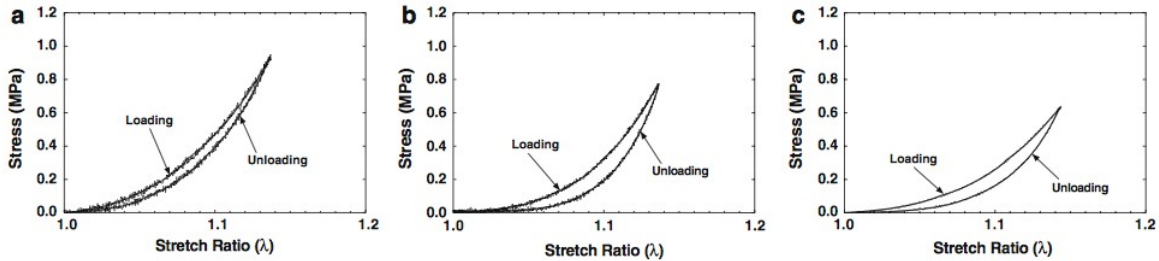
Figure 3.2: Curves of stress vs. stretch ratio for three eardrum specimens obtained from uniaxial tensile tests. The wave-like lines were the original experimental stress-stretch ratio curves, and the smooth lines were obtained after the Ogden model fitting process. Hysteresis between the loading and unloading curves was seen on each specimen. (Source: Cheng et al. 2007)
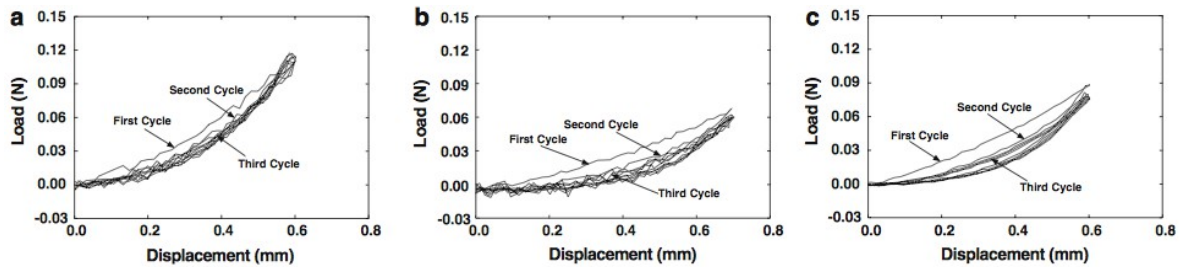
Figure 3.3: Load-displacement curves of the first, second and third cycle of three eardrum specimens. A steady state is observed by the third cycle. (Source: Cheng et al. 2007)

Luo et al. (2009) also investigated the mechanical behaviour of strips of human eardrum but with higher strain rates. They used a newly developed miniature split Hopkinson tension bar to measure the mechanical properties with emphasis on the Young's modulus at high strain rates (300–2000 s^{-1}). In order to provide a consistent preconditioning, each eardrum specimen was subjected to multiple "to-and-fro reflected waves" to load and unload the specimens with small amplitudes. They observed an increase in the Young's modulus with increasing strain rate, indicating a rate-dependence of the viscoelastic behaviour of the eardrum.

Motallebzadeh et al. (2013) combined modelling of the non-linear and viscoelastic effects

in the eardrum for the first time. Their model could reproduce the hysteresis curves of Cheng et al. that are discussed above, which is an important step toward understanding the viscoelastic phenomena of the eardrum under conditions that are comparable to those involved in tympanometry.

3.3 Gerbil Studies

3.3.1 Early gerbil studies

The earliest studies of the gerbil ear focused primarily on measurements pertaining to auditory sensitivity. Finck and Sofouglu (1966) measured the auditory sensitivity of the Mongolian gerbil by recording the cochlear microphonic response at the round window. They measured from 0.2 to 30 kHz and reported good sensitivity in the low-to-mid frequency range, with maximum sensitivity at approximately 4 kHz. The same technique was used by Lay (1972), who reported similar findings. Webster & Webster (1972) reported that the enlarged middle-ear cavity of the gerbil contributes to an increase in low-frequency sensitivity. Ryan (1976) reported that gerbils respond to frequencies between 0.1 and 60 kHz with high sensitivity between 1 and 16 kHz, which is consistent with the range of auditory sensitivity reported by Finck and Sofouglu and by Lay. Henry et al. (1980) tested the auditory nerve function of Mongolian gerbils at five different ages and reported an age-related increase in the auditory-nerve isoelectric thresholds at all frequencies below 64 kHz.

3.3.2 Unpressurized vibration measurements

Some groups have indirectly studied vibrations in the gerbil middle ear by investigating the input admittance at the eardrum (e.g., Ravicz et al. 1992; Ravicz & Rosowski 1997; Teoh et al. 1997). Although admittance is easy to measure, it does not give the actual amplitudes of vibration on the eardrum. Other groups have used LDV to perform single-point vibration measurements at the umbo (e.g., Cohen et al. 1993; Rosowski et al. 1999; Rosowski & Lee 2002). Neither admittance measurements nor vibration measurements at the umbo provide

information about the spatial vibration patterns of the eardrum, which are important to gain a better understanding of middle-ear mechanics.

De La Rochefoucauld & Olson (2010) measured the vibration of the gerbil eardrum at a few points on the pars tensa near the umbo as well as along the manubrium. Aside from these measurements, only our group has published studies that investigate the vibration pattern of the gerbil eardrum. Measurements at multiple points were first reported by Ellaham et al. (2007) in five *post mortem* gerbils. Magnitudes of displacement were measured at points along the manubrium as well as on the pars tensa over a frequency range from 0.15 to 10 kHz. The study included a detailed investigation of the effects of drying of middle-ear structures on the recorded frequency responses. Figure 3.4 is a spectrogram tracking the eardrum frequency shifts over time at the mid-manubrium level. Magnitudes are expressed with a logarithmic colour scale normalized to 90 nm/Pa (near maximal displacement). They observed that, with time, the peaks of the magnitude responses shifted to higher frequencies. Passive rehydration of the middle-ear structures was performed by placing moist cotton on the exposed bulla, indicated in the spectrogram by red triangular markers next to the plot. Immediately following rehydration, a shift to lower frequencies was observed in the magnitude response, bringing the peak closer to its initial frequency. Nambiar (2010) performed *post mortem* studies similar to those of Ellaham et al. but with much better hydration of the middle-ear structures.
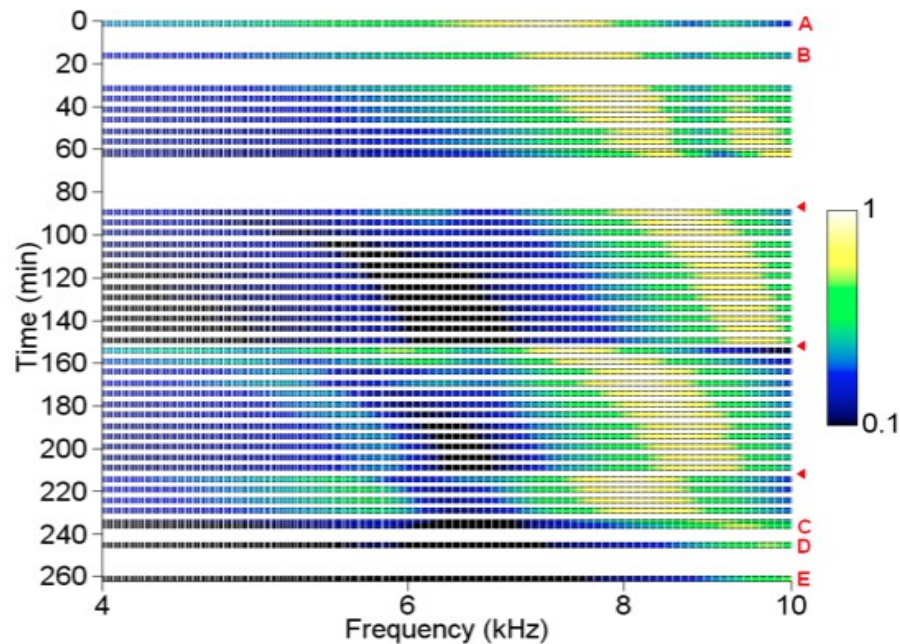
Figure 3.4: Spectrogram assessing frequency shifts over time at the mid-manubrium level. The colour scale is normalized to 90 nm/Pa. Red markers indicate the times of passive rehydration. (Source: Ellaham et al. 2007)

In a more recent study in our group, Maftoon et al. (2012, 2013) used LDV to perform *in vivo* vibration measurements of the gerbil eardrum at several points on the pars tensa, along the manubrium and on the pars flaccida. Data were presented for two pars-flaccida conditions: naturally flat, and retracted into the middle-ear cavity. They reported a minimum and a shallow maximum in the magnitude responses of the manubrium and pars tensa at low frequencies, resulting from a resonance of the pars flaccida when in its flat condition. A retracted pars flaccida resulted in reduced magnitudes at low frequencies on the manubrium and pars tensa. At higher frequencies, they observed a roll-off of the magnitude responses on the manubrium with some irregularities. Based on their measurements at multiple points on the pars tensa in each gerbil, they reported that the break-up of the simple low-frequency pattern into more complex patterns occurs between 1.8 and 2.8 kHz. Our group has also developed a method to more widely expose the eardrum, so as to be able to perform measurements on a larger area and ultimately to better characterize the vibration pattern (He 2012).

3.4 Static pressure deformations

It has been well established that middle-ear function is affected by variations of static pressure. During the acute stages of chronic inflammatory middle-ear disease, inward or outward bulging of the eardrum due to pressure variations is observed (von Unge et al. 1993). The resulting changes in the stiffness of the eardrum are important factors in the pathophysiology of the disease (Falk 1982). As mentioned in Chapter 1, static pressures are also involved in tympanometry, a useful clinical tool for assessing the condition of the middle ear. However, this technique only provides a single admittance measurement for the entire eardrum. In a number of studies, Decraemers' group has used the optical technique of moiré topography to obtain full-field measurements of the shape of the eardrum and of its deformations in response to static pressure variations. Over the years, the implementation of the moiré technique has evolved from real-time differential moiré topography to phase-shift moiré topography and most recently to high resolution phase-shift moiré topography.

Dirckx & Decraemer (1991) studied the effect of static pressure on the shape of the human eardrum. After recording the shape in an unpressurized state, multiple measurements were taken for positive and negative middle-ear pressures ranging from −1.6 kPa to +1.6 kPa. As shown in Figure 3.5, they determined the umbo displacement as a function of the applied middle-ear pressure. The experimental data are represented with circles and a smooth curve is fitted through the points. Measurements presented by Kobrak (1948) and Huttenbrink (1988) are given by triangular and square markers, respectively. The strong S-shape of the curve for both positive and negative pressures demonstrates that the movement of the malleus is highly nonlinear. They found that the displacement of the umbo was asymmetrical, being much larger for positive pressures than for the corresponding negative pressures. Their measurements were in agreement with those of Huttenbrink (1988), suggesting that their specimen responded normally to pressure changes. The displacements presented by Kobrak (1948) are much smaller: Dirckx & Decraemer suggested that the discrepancy was because Kobrak "calculated the umbo movement from measurements of

the rotation of the malleus head."
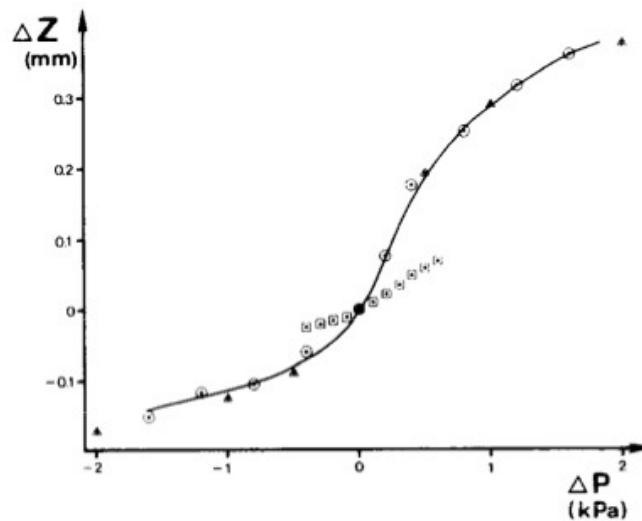
Figure 3.5: Umbo displacement ΔZ versus the applied middle-ear pressure ΔP. The experimental data are given by circles and a smooth curve is fitted through the points. Data presented by Huttenbrink (1988) and by Kobrak (1948) are given by triangles and squares, respectively. (Source: Dirckx & Decraemer 1991)

Von Unge et al. (1993) measured the shape and displacement of the gerbil eardrum in response to static pressure variations. A compressor with a U-tube manometer was used to apply positive and negative middle-ear pressures up to 20 cm H_2O (2.0 kPa). Two areas of maximum magnitude were observed at approximately the same level, one on the anterior side and one on the posterior side. The locations of the areas remained constant as the pressure increased. Figure 3.6 shows the displacement of a point on the pars tensa as a function of pressure for two cycles of positive and negative pressures. In each cycle, the loading curves were sampled at eight pressure levels, stopping for 20 s at each new level. After recording at the maximum level, the pressure was returned to zero, stopping for 20 s at 10 and 4 cm H_2O. They observed smaller displacements during the loading part than during the unloading part for a given pressure. These differences in displacement decreased as the absolute value of the applied pressure increases, and the loading and unloading curves formed a hysteresis loop. von Unge et al. also observed that the loading

displacements of the second cycle were larger than those of the first cycle for a given positive pressure, and that displacements of the second and third run were approximately the same, "indicating that the hysteresis curves tend rapidly to reach a steady 'pre-conditioned' state."
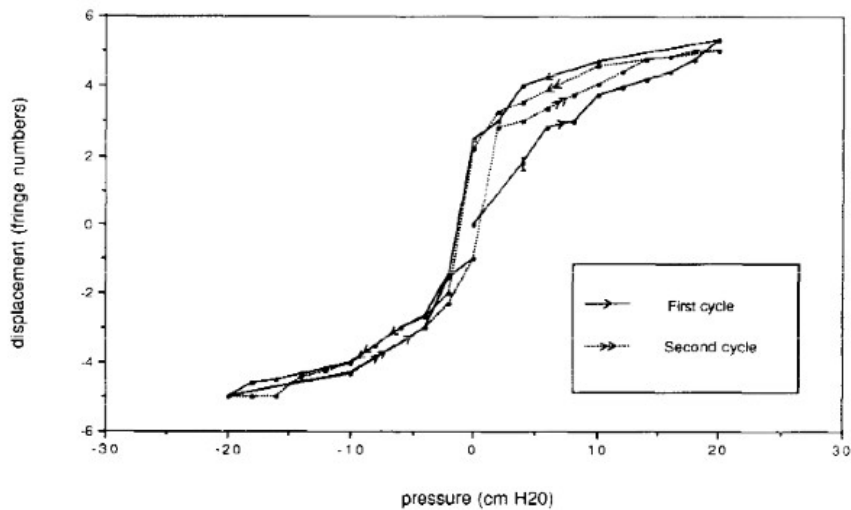
Figure 3.6: Displacement plot as a function of time at a point on the posterior region of the pars tensa during two complete cycles of positive and negative pressures. (Source: von Unge et al. 1993)

Funnell & Decraemer (1996) measured the shape of the cat eardrum under static pressures as high as ±220 mm H_2O (2.2 kPa). The goal was to more clearly determine the boundaries of the pars tensa, manubrium and pars flaccida; during the application of large static pressures, the displacements at the periphery of the eardrum and on the manubrium are much smaller than on the neighbouring pars tensa. The pressure-displacement curves at a point on the posterior side of the pars tensa are shown in Figure 3.7. Although the unloading curves were not actually measured in this study, they observed the effect of hysteresis in the curves. They imported the moiré shapes into finite-element models to quantify how much the shape of the eardrum affects its mechanical behaviour, as reflected in its vibration amplitudes. They also suggested that the eardrum must reach a steady pre-conditioned state before repeatable measurements can be obtained.
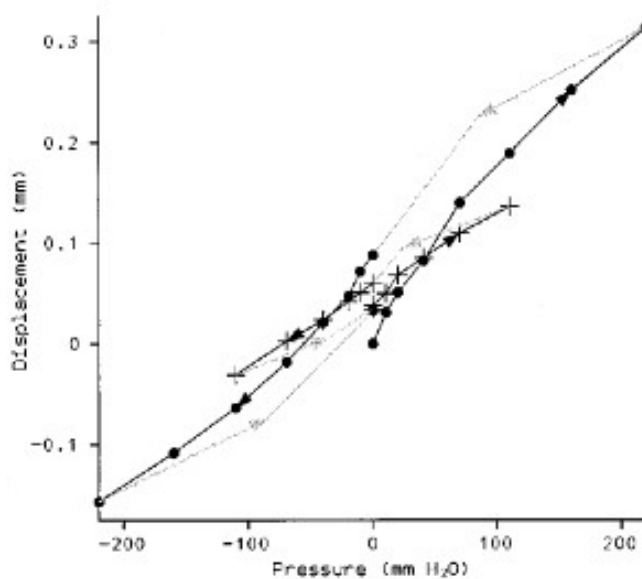
Figure 3.7: Pressure-displacement curves for a location in the posterior region of the pars tensa. Circles correspond to measurements from the first cycle of pressures and crosses correspond to measurements from the second. Arrows indicate the temporal order of the measurements. (Source: Funnell & Decraemer 1996)

Dirckx & Decraemer (2001) measured the deformation of the eardrum in response to quasi-static middle-ear pressures. After an initial unpressurized measurement, eight positive pressures ranging from 0.1 kPa to 2 kPa were applied to the middle ear, and then the ear was unloaded by applying the same pressures in the reverse order, followed by another zero pressure. Unlike the case in previous static pressure deformation studies, the unloading curve is fully sampled. They obtained shape profiles at various stages of dissection of the middle ear. Measurements with an intact middle ear were used as a baseline and the measurements at other stages of dissection were compared with it. Figure 3.8 shows the mean deformation as a function of pressure for an intact ear (stage 0) as well as following the removal of the cochlea (stage 1). The curves for each stage are very similar; only at negative pressures is there a small difference. They concluded that the cochlea, stapes and tensor tympani have little or no influence on static eardrum deformations. Hysteresis in the curves is evident: for positive pressures the unloading curves are higher than the loading curves, and for negative pressures the loading curves are more negative.
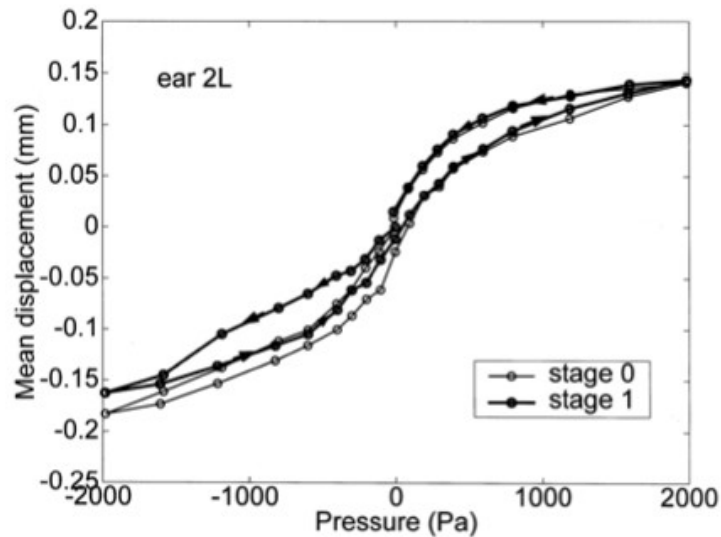
Figure 3.8: Mean deformation as a function of pressure. Stage 0 corresponds to the curve obtained in an intact ear and stage 1 corresponds to the curve obtained after removal of the cochlea. Only at negative pressures is there a small difference. (Source: Dirckx & Decraemer 2001)

Ladak et al. (2004) studied the effect of static pressure on the shape of the cat eardrum with both a mobile manubrium and a fixed manubrium. As for Dirckx & Decraemer (2001), the full loading and unloading curves were measured. After an initial unpressurized measurement, seven positive pressures ranging from 0.1 to 2.2 kPa were applied to the middle ear, and then the ear was unloaded by applying the same pressures in the reverse order, followed by another zero pressure. The process was repeated for negative pressures. Three of these pressure cycles were applied to the eardrum over the course of the experiment. Mobile-manubrium measurements were performed in five cat ears. Magnitudes on the pars tensa were larger than on the manubrium, and in all cats except one the magnitude maximum on the pars tensa occurred on the posterior side. The pressure-displacement curves for all three pressure cycles in one cat at a single point on the pars tensa are shown in Figure 3.9. The effect of hysteresis is exhibited: the displacements during unloading are larger than the displacements during loading within each cycle. In addition, they observed that magnitudes varied from cycle to cycle, and that the variation was systematic. The direction of the cycle-to-cycle change is the opposite of what is expected for conditioning.
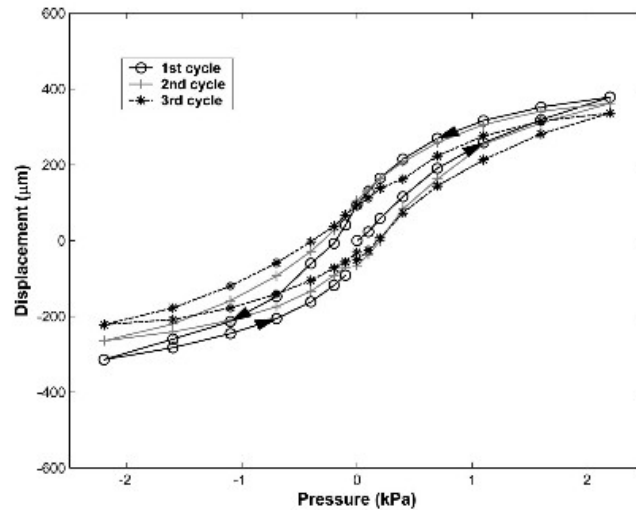
Figure 3.9: Pressure-displacement curves at a point in the posterior region of the cat pars tensa. The three cycles are indicated by different symbols, as shown in the legend. (Source: Ladak et al. 2004)

Charlebois et al. (2004), in an investigation of the nonlinear tensile properties of bovine articular cartilage, found that viscoelastic behaviour of the soft tissue was still present even a few hours after each large static-pressure application. This finding suggests that in the Decraemer protocol, as well as in our study, possible viscoelastic effects may not dissipate in the time interval (10 to 20 s in the Decraemer protocol and in our study) between the application of the static pressure and the start of a measurement, which will affect interpretation of our results.

3.5 Pressurized eardrum vibrations

3.5.1 Tympanometric measurements

Osguthorpe & Lam (1981) studied the effects of the rate and direction of pressure change on tympanometry in cats. They measured both the susceptance and conductance components of admittance. In 13 cat ears, ascending and descending pressure runs between +400 and −600 mm H_2O (+3.9 kPa and −5.9 kPa) were compared, with rates of pressure

change of 12.5 and 50 mm H_2O/sec (0.1 and 0.5 kPa/sec). The resulting tympanograms for the acoustic susceptance are shown in Figures 3.10. They observed that the tympanograms for descending runs were simple, characterized by a single peak, but that the ascending runs produced notched tympanograms. For both ascending and descending runs, they observed that a decreased rate of pressure change corresponds to a lower maximum of the tympanogram curve. For ascending runs they observed a smaller pressure interval over which the notch occurred compared with descending runs.
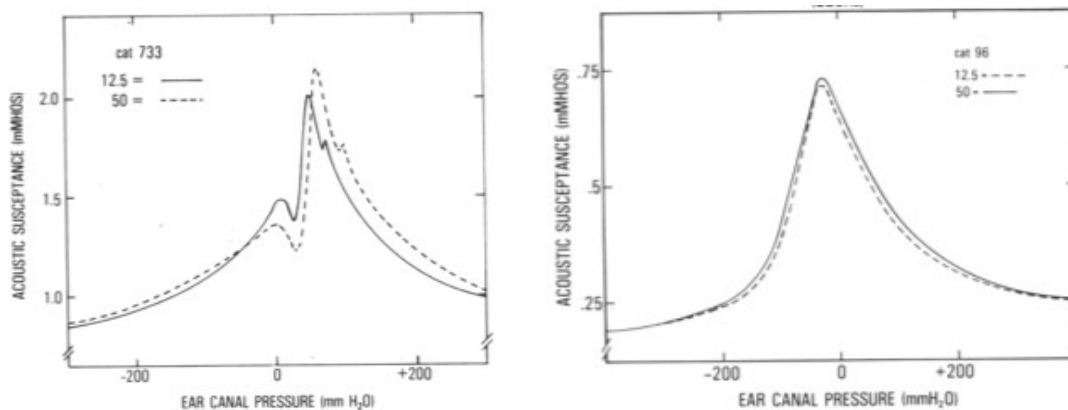
Figure 3.10: Ascending (left) and descending (right) tympanograms in a typical cat ear at rates of pressure change of 12.5 and 50 mm H_2O. (Source: Osguthorpe & Lam 1981)

Osguthorpe & Lam also investigated the stability of tympanograms in response to repetitive testing, in both cats and human subjects. They subjected each ear to 30 descending pressure runs within a 20 min period. The resulting susceptance and conductance tympanograms of the first, third and tenth descending runs in a typical human subject are shown in Figures 3.11. In most subjects they observed an increase in admittance between the first and the tenth runs, with the rate of the increase decreasing with each run. They also observed shifts of the admittance both at the peak (zero pressure) and at the tails (positive and negative pressure extremes). They also reported that in one human ear the tympanogram changed from a single-peaked curve to a notched curve on the third descending run, indicating that "tympanogram morphology can change during a sequence of pressure sweeps."
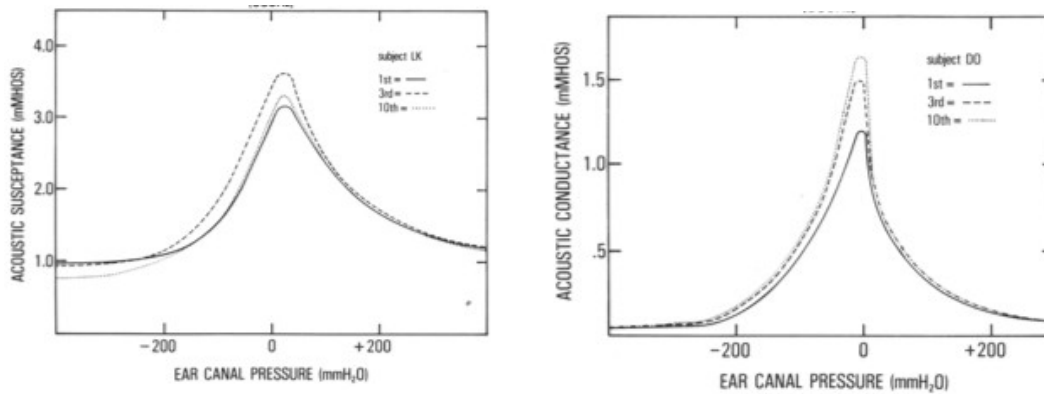
Figure 3.11: Susceptance and conductance tympanograms from repetitive testing in a typical human subject. The first, third and tenth descending runs are shown. (Source: Osguthorpe & Lam 1981)

von Unge et al. (1991) used probe tones of 220 and 660 Hz to obtain tympanometric measurements in isolated temporal bones of healthy Mongolian gerbils. Susceptance curves with a probe tone of 660 Hz obtained from a normal ear with a ventilation hole in the bulla are shown in Figure 3.12. A single-peaked curve was obtained during the increasing pressure sweep but a W shape was obtained for the decreasing pressure sweep. They also reported the effects of various interventions in the middle ear.
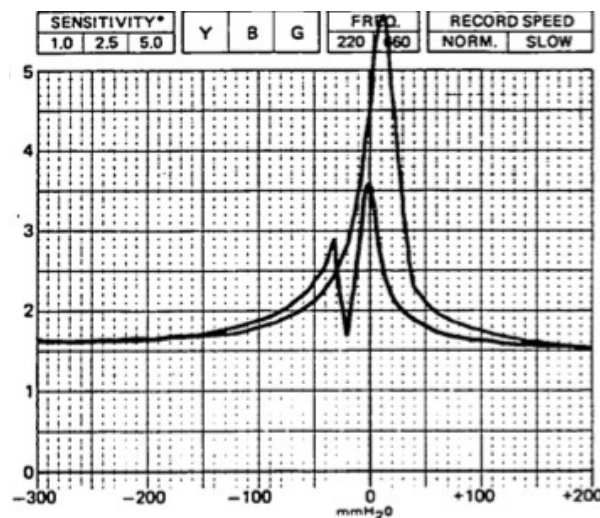
Figure 3.12: Susceptance curves from a normal gerbil termporal bone recorded with a probe tone of 660 Hz. A single-peaked curve is obtained during the increasing pressure sweep and a W-shaped curve is obtained during the decreasing pressure sweep. (Source: von Unge et al. 1991)

Gaihede (1996) investigated the effects of the rate of pressure change on the increased compliance that occurs as a result of repetitive loading-unloading experiments (e.g. Osguthorpe & Lam 1981). He performed 9 tympanometric measurements in each of 103 ears of 53 healthy adults. (In 3 subjects, a sealed condition could only be obtained in one ear.) The subjects were assigned different rates of ear-canal pressure change: 50, 100, 200 and 400 daPa/s. The mean compliance in each group is plotted as a function of the tympanometric trial number in Figure 3.13. For each group he observed a similar increase in compliance for the early trials, reaching a steady pre-conditioned state for later trials. Tympanometric measurements at 50 daPa/s showed the lowest mean compliances and measurements at 400 daPa/s showed the highest.
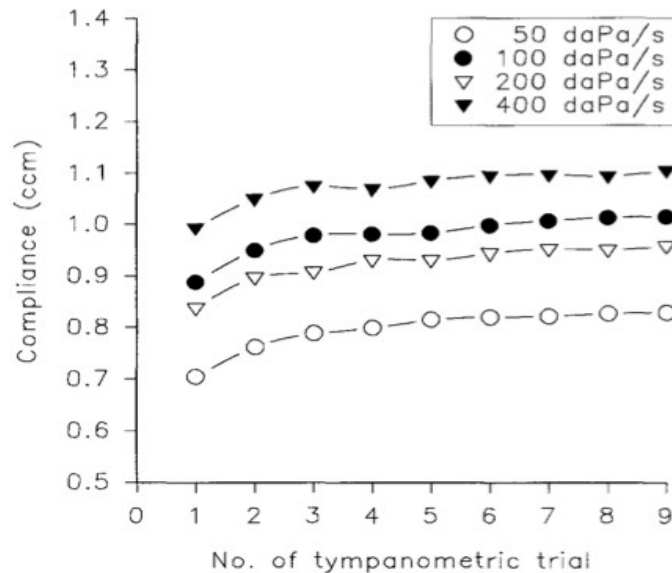
Figure 3.13: Average compliance for each rate of pressure change plotted as a function of the tympnaometric trial. An increase in compliance is observed for the early trials, reaching a steady state for the later trials. (Source: Gaihede 1996)

3.5.2 Laser Doppler vibrometry measurements

The middle-ear disease of otitis media with effusion is diagnosed when there is fluid behind the eardrum, in the middle-ear cavity, often with a difference between the middle-ear pressure and atmospheric pressure. Gan et al. (2006) used two laser vibrometers to simultaneously measure the eardrum and stapes vibrations in human temporal bones with various middle-ear pressures and with different levels of liquid. Their displacement responses of the eardrum (umbo) from seven temporal bones, recorded over the frequency range from 0.2 to 8 kHz in response to positive and negative middle-ear pressures ranging from 0 to ±20 cm H_2O (±2.0 kPa), are shown in Figures 3.14. They found that the umbo displacements were similar for both positive and negative pressures, being reduced by approximately 10 dB at frequencies below 1.5 kHz for pressures of 2 kPa.
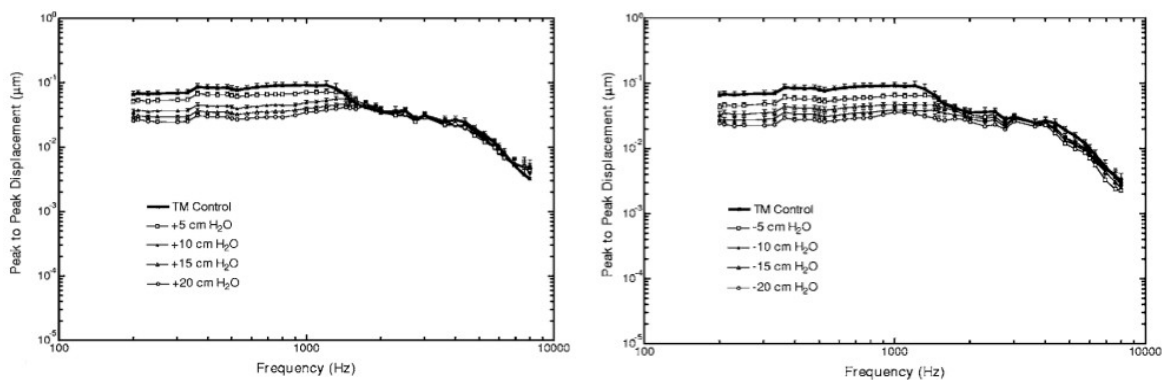
Figure 3.14: Displacement responses of the eardrum (umbo) from seven temporal bones in response to positive (left) and negative (right) middle ear pressures. (Source: Gan et al. 2006, Figure 3a (left) and Figure 4a (right))

Homma et al. (2010) used laser Doppler vibrometry to measure middle-ear ossicular velocities under static pressure in human cadaver ears in response to both air-conduction and bone-conduction excitations. They used an air pump with a U-tube manometer to apply static pressures of ±200 mm H_2O (2.0 kPa) and ±400 mm H_2O (3.9 kPa) in the ear canal. Figure 3.15 shows the effects of static pressurization on the middle-ear air-conduction responses obtained at the umbo. They found a reduction by about 10–12 dB for ear-canal pressures of ±200 mm H_2O and 15–18 dB for ear canal pressures of ±400 mm H_2O over the

frequency range from 0.3 to 1.5 kHz, with smaller reductions at higher frequencies. Magnitudes of the pressurized responses were found to be similar for both positive and negative pressures. They also observed that the responses peaks are shifted to higher frequencies with an increase in pressure, with the magnitudes rising above those of the unpressurized responses at the highest frequencies.
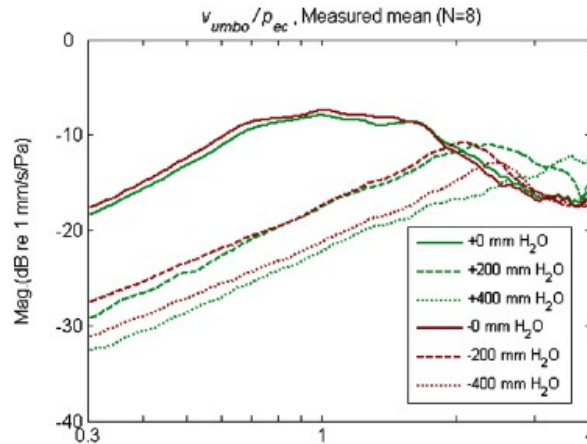
Figure 3.15: Effects of ear-canal pressurization on the air-conduction umbo responses. (Source: Homma et al. 2010)

3.6 Summary

In summary, we have reviewed a number of eardrum studies that are related to our work, including unpressurized vibration patterns, pressurized shape measurements, and admittance and umbo vibration measurements. However, there have been no studies involving pressurized eardrum vibrations; this will be discussed in the remainder of this thesis.

CHAPTER 4
MATERIALS AND METHODS

4.1 Introduction

The experimental materials and methods employed in our work are presented in this chapter. The preparation of the gerbil is presented in Section 4.2, followed by a description of the experimental setup in Section 4.3. Details regarding the acoustical system are presented in Section 4.4. The reflective properties of the eardrum and the measures taken to improve reflectivity are presented in Section 4.5. The design and manufacture of a new acoustic coupler are discussed in Sections 4.6 and 4.7 respectively. The pressurization device developed to establish a static pressure in the middle-ear cavity is discussed in Section 4.8. Details regarding the two experimental protocols used in this study are presented in Section 4.9. Finally, the basic principles of LDV are presented in Section 4.10.

4.2 Animal preparation

The measurements were performed on Mongolian gerbils (*Meriones unguiculatus*) provided by Charles River Laboratories (St-Constant, Québec). Eight gerbils were used, with body weights ranging from 75 to 102 g, as shown in Table 4.1. A schematic illustration of the preparation is shown in Figure 4.1.

Prior to surgery, the gerbil is euthanized by anaesthetic overdose with CO_2 gas. An ultrasonic humidifier is used during the surgical procedure in order to reduce the *post mortem* drying of the eardrum. An incision is made between the shoulder and the jaw, followed by the careful removal of the skin and soft tissue in order to expose the bulla. The surgical procedure is performed with caution in order to avoid cutting nearby blood vessels and to prevent physical damage to the bulla; the exposed bulla and surrounding blood vessels are shown in Figure 4.2. The bony ear canal is drilled away to create an opening through which to access the eardrum. A black membrane that lines the bony ear canal

Table 4.1: Weights of all gerbils

Gerbil	Weight (g)
A	96.8
B	76.3
C	77.4
D	75.0
E	77.0
F	98.7
G	101.2
H	101.8

(Figure 4.2b) is useful for trapping the bone chips that are created during drilling and that would otherwise fall onto the eardrum. Once the drilling is complete, this membrane is cut and folded over the outer walls of the bulla, exposing the eardrum.
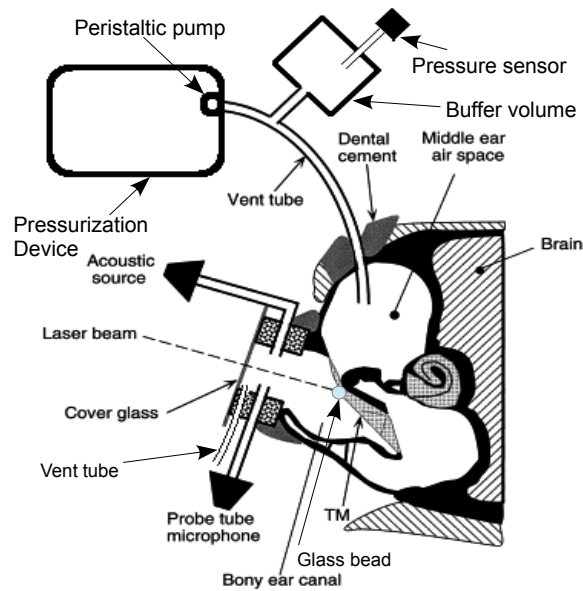
*Figure 4.1: Schematic illustration of the gerbil middle ear and
the experimental preparation. (After Lee and Rosowski 2001)*

In order for the eardrum to vibrate normally, the air pressure in the middle ear must be the same as atmospheric pressure. For instance, a middle-ear pressure that is lower than atmospheric will cause the eardrum to be sucked inward, reducing the mobility of the eardrum and ossicles. This pressure is normally regulated by the opening of the Eustachian

tube, supplying air to the middle-ear cavity (e.g., Sadé & Am 1997). When the animal is euthanized, the muscles of the Eustachian tube are disabled, potentially causing a build-up of negative middle-ear pressure and a subsequent accumulation of liquid in the middle-ear cavity (e.g., Maftoon et al. 2013). To prevent this, a 1-mm-diameter ventilation hole is drilled into the inferior part of the bulla, as shown in Figure 4.3. The hole must be located far enough from the opening of the ear canal to avoid interference with the base of the coupler. A ventilation hole in the bulla results in a change in the acoustical properties of the system. In order to minimize these effects, a 12-cm-long flexible plastic tube (inner diameter = 0.58 mm, outer diameter = 0.96 mm) is inserted into the hole, effectively blocking it in the audible frequency range.

Small glass-coated plastic micro beads are then placed at the two locations on the eardrum where measurements are desired: on the manubrium and on the posterior part of the pars tensa, both at the mid-manubrium level. (We avoid measurements at the umbo due to previous reports of bending, as discussed in Chapter 3. The use of micro beads as reflective targets is further discussed in Section 4.5.) A wooden block is secured with dental cement to the superior part of the gerbil skull after removal of the skin and soft tissue. Dental cement is also used to attach a custom-made washer to the walls of the bulla surrounding the opening of the ear canal.
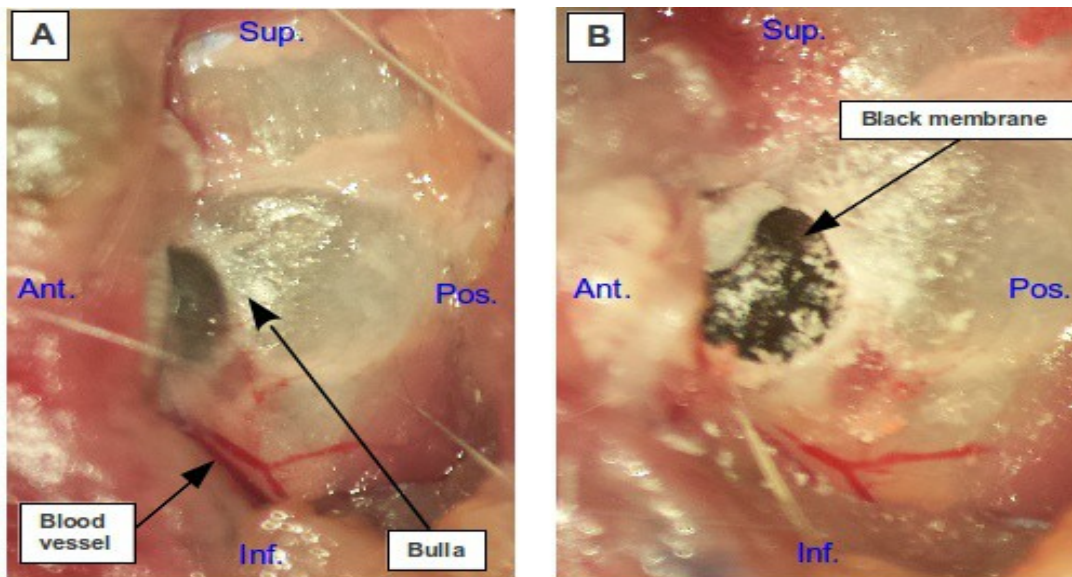
*Figure 4.2: **A.** Exposed bulla and surrounding blood vessels, before drilling.*
__B.__ The black membrane catches the falling bone chips during drilling.
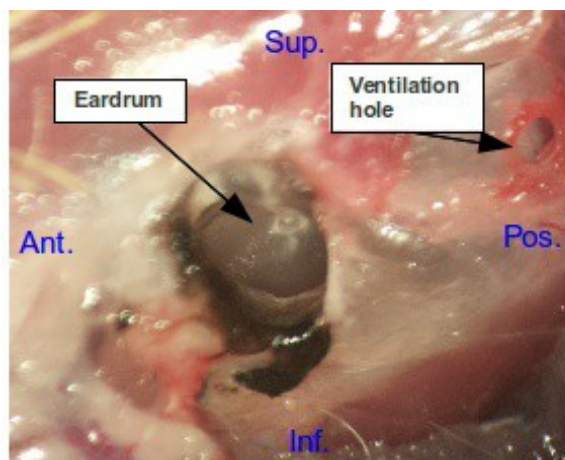
Figure 4.3: Exposed eardrum after removal of
the black membrane, and ventilation hole.

4.3 Experimental setup

After allowing 15–20 min for the dental cement to solidify, an acoustic coupler (discussed in Section 4.4) is threaded into the washer. An aluminum rod secured to the wooden block is connected to a fixation device that allows the user to manipulate the head of the gerbil in order to obtain an optimal viewing angle for the eardrum. The fixation device, shown in Figure 4.4, is held in place on the measurement table by virtue of its massive base. More dental cement is used to seal any remaining air gaps surrounding the ventilation tube at the interface with the ventilation hole. (Such gaps would prevent the maintenance of static pressures in the middle-ear cavity.) A pressurization system is then connected to the ventilation tube of the bulla. The prepared gerbil is placed under the operating microscope (OPM1-H, Zeiss, Oberkochen, Germany), to which a single-point laser Doppler vibrometer (discussed in Section 4.10) is attached. The gerbil is placed on a SnuggleSafe heating pad (Lenric C21 Ltd., West Sussex, United Kingdom). (In *in vivo* experiments it is used to keep the animal warm but here it is simply used as a platform for the gerbil.) The pad sits on several layers of air-bubble cushioning material in order to reduce low-frequency vibration transmission from the building. A photograph of the experimental setup is shown in Figure 4.4. The acoustical system, pressurization system and optical system of the setup are discussed in the following sections. In order to reduce dehydration of middle-ear structures over the course of the experiment, we continue to use the ultrasonic humidifier and we also place moist cotton onto the walls of the bulla.

Normally, the first measurements are performed approximately 120 minutes following the sacrifice of the gerbils. Experimental complications in gerbils B, F and G led to increased preparation times. In gerbil B some debris fell onto the eardrum and needed to be carefully removed, increasing the preparation time by nearly 45 min. In gerbil F the eardrum was cut with the surgical knife and in gerbil G it was perforated with the paint brush, forcing a restart of the preparation in the other ear, increasing the preparation time by nearly 120 min.
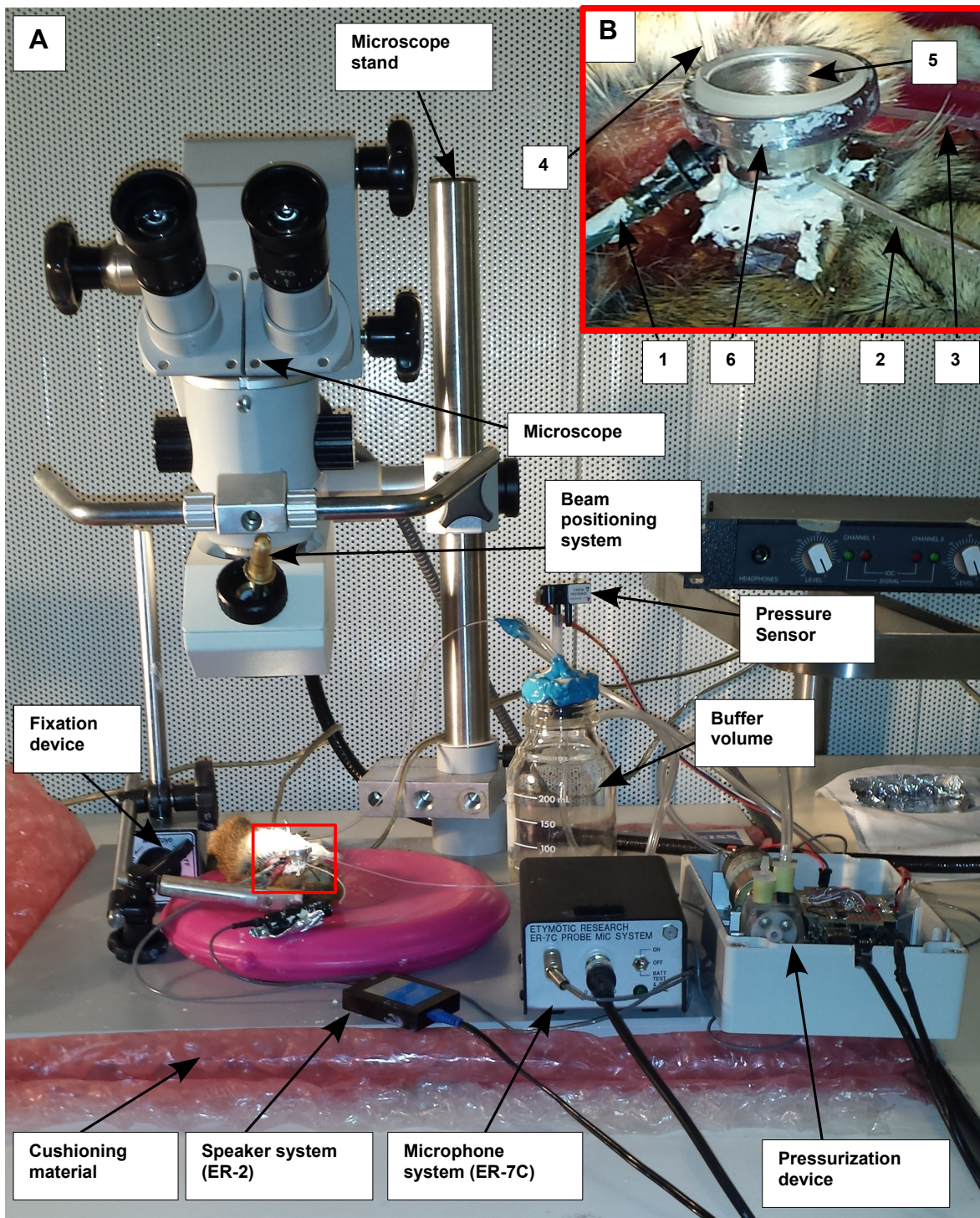
Figure 4.4: ***A.*** *Experimental setup.* ***B.*** *Close up of the preparation. (1) Tubephone (ER-2) tube. (2) Probe microphone (ER-7C) tube. (3) Ventilation tube of coupler. (4) Ventilation tube of middle ear. (5) Glass window. (6) Acoustic coupler secured to the bulla with dental cement.*

4.4 Acoustical system

During measurements the eardrum is stimulated by an ER-2 Tubephone (Etymōtic Research, Elk Grove Village, IL), shown in Figure 4.5. The resulting sound pressure level is recorded by a probe-microphone system (ER-7C, Etymōtic Research), shown in Figure 4.6. Both speaker and microphone have flat (± 3 dB) magnitude responses over the frequency range of interest. Given that the speaker is only capable of generating small volume velocities, the tubephone and probe microphone are connected to a small custom-made acoustical sound chamber or coupler. Its design is discussed in detail in Section 4.6. The coupler requires three holes, for insertion of the speaker tube, the probe-microphone tube and the ventilation tube. The tubes must be placed carefully to avoid obstructing the path of the laser beam projected from the vibrometer laser head. An anti-reflective glass window (NT49-139, Edmund Optics, Pike Barrington, NJ) is placed on the upper ledge of the coupler to acoustically seal the sound chamber. To attenuate noise from the surrounding environment, the vibration measurements are performed in a double-walled audiometric sound-proof chamber (C-24, Genie Audio, St-Laurent, QC), shown in Figure 4.7.
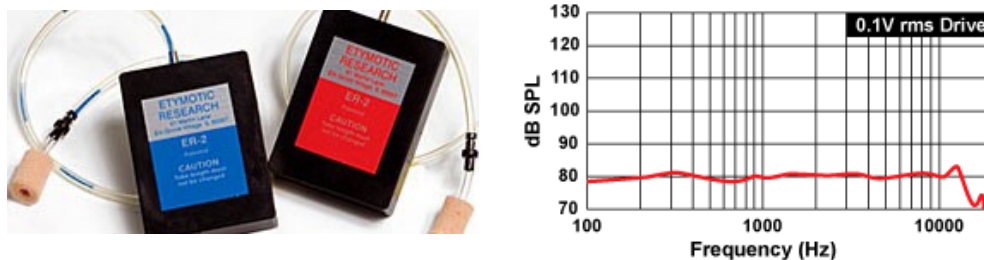
Figure 4.5: ER-2 Tubephone, and its frequency response.
(Source: http://www.etymotic.com/pro/er2-ts.aspx, retrieved 2013 May 30)

Figure 4.6: ER-7C probe microphone system.
(Source: http://www.etymotic.com/pro/er7c-acc.aspx,
retrieved 2013 May 30)

Figure 4.7: C-24 soundproof examination chamber.
Inside Dim. 66" x 77" x 78". Outside Dim. 90" x 101" x 97".
(Source: http://www.genieaudio.com/en/products/, retrieved 2013
May 30)

The signal-to-noise ratio (SNR) and the frequency resolution are highly dependent on the acoustical stimulus chosen. For example, a pure-tone sinusoidal excitation signal at a single frequency gives a high SNR. Repeating at multiple frequencies is very time-consuming, however, and obtaining a high frequency resolution is extremely difficult due to drying of the eardrum over time. Alternatively, sinusoidal sweep signals have a high bandwidth, 'sweeping' through the frequency range in just a single measurement and delivering a high frequency resolution. Without averaging, a sinusoidal sweep stimulus gives a fairly high quality signal with a high SNR. White noise is also rich in frequency content, containing many frequencies with equal intensities. Noise as an excitation stimulus must be used with averaging since a meaningful frequency response cannot be obtained from a single measurement. After testing each type of signal in a gerbil ear, we determined that burst random signals provide a better SNR than the other averaged signals available in the vibrometer software. Finally, a 128-ms burst random noise signal containing frequencies from 0.2 to 12.5 kHz was used as the stimulus. The durations of the silence periods before and after each burst of white noise were 51.2 ms and 76.8 ms respectively. The signal was averaged 20 times. The software of the vibrometer used a 1600-line FFT to transform the recorded time-domain signals of the microphone and vibrometer to the frequency domain. The resulting frequency resolution was 7.813 Hz. A two-pass moving-average filter with a window length of five was used to smooth the real and imaginary parts of the complex signal. (The filter uses forward and reverse passes in order to avoid phase distortion.) The magnitude and phase responses were then obtained from the filtered real and imaginary parts. The frequency-response function was estimated as the cross spectral density of the excitation and response signals divided by the power spectral density of the excitation signal.

4.5 Reflective targets

The operation of the vibrometer requires that the object surface reflect a sufficient quantity of light. However, biological tissues such as the eardrum are characterized by high

anisotropy coefficients, resulting in a loss of light due to forward scattering (Dirckx & Decraemer 1996). Consequently, reflective materials are applied to the surface of the eardrum to reduce the amount of forward-scattered light, increase the back-scattered light and improve the SNR. Materials such as white India ink, magnesium oxide powder, silver powder, reflective tape and individual glass micro beads have been used for this purpose.

In this study, we place glass-coated plastic microcarrier beads (Sigma-Aldrich, G4519) at the desired measurement locations on the eardrum. Micro beads are particularly useful for investigating the repeatability of a measurement at a desired location, thereby addressing a fundamental goal of this study as discussed in Chapter 5. According to the manufacturer, the beads range from 90-150 μm in diameter. The beads that appear rounder and more reflective under magnification are selected and placed onto the eardrum with a fine paint-brush reduced to a single bristle. No particular measures were taken to attach the beads to the eardrum. Decraemer et al. (1989) validated the use of glass micro beads by comparing the frequency response of a bead placed on the tip of the manubrium and the response of a bright reflective spot adjacent to that bead. They found that throughout the frequency range of 0.13 to 25 kHz the ratios between the two measurements remained between 0.85 and 1.15 and the phase differences remained between −10º and 25º. This indicates that the bead followed the underlying vibration pattern of the manubrium. The micro beads must be placed with caution to avoid perforating the eardrum with the tip of the bristle – even the slightest perforation will prevent the establishment of a static pressure in the middle-ear cavity. In this study, vibration measurements are performed on the manubrium and on the pars tensa at the level of the middle of the manubrium. A microphotograph of the the gerbil eardrum after the placement of beads is shown in Figure 4.8.
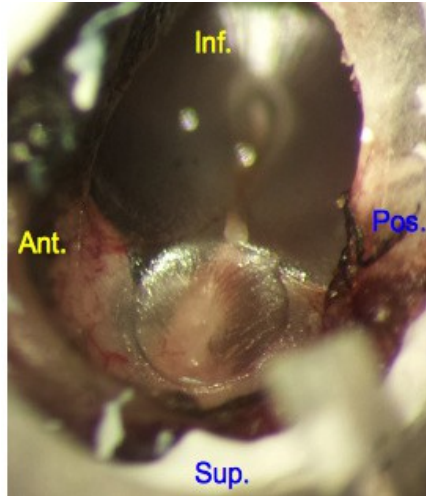
*Figure 4.8: Microphotograph of the
eardrum after placement of micro beads.*

4.6 Coupler design

4.6.1 Introduction

As mentioned above, the sound delivered to the middle ear is confined to the volume of a small coupler. A new coupler was designed and manufactured to improve upon the previous coupler designed in our lab (Ellaham 2007). 3-D computer-aided design (CAD) models of the previous and new couplers and their associated washers were created using SolidWorks (Dassault Systèmes, Waltham, MA) and are shown in Figure 4.9. The engineering drawings
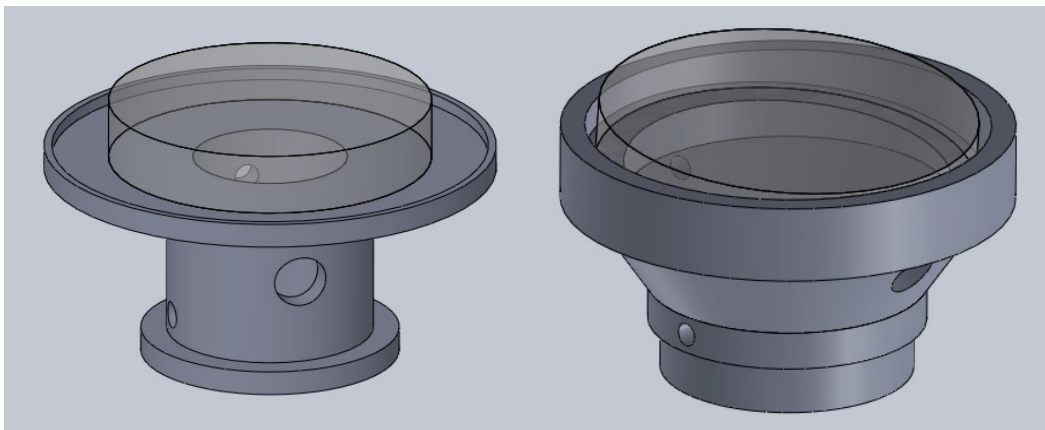
Figure 4.9: 3-D CAD models of the previous coupler and washer (left) and the newly designed coupler and washer (right) used in this study. Details of the new coupler and washer are shown in the engineering drawings of Figures 4.10 and 4.11, respectively.

of the new coupler and washer are shown in Figures 4.10 and 4.11 respectively. All dimensions shown are in millimetres.
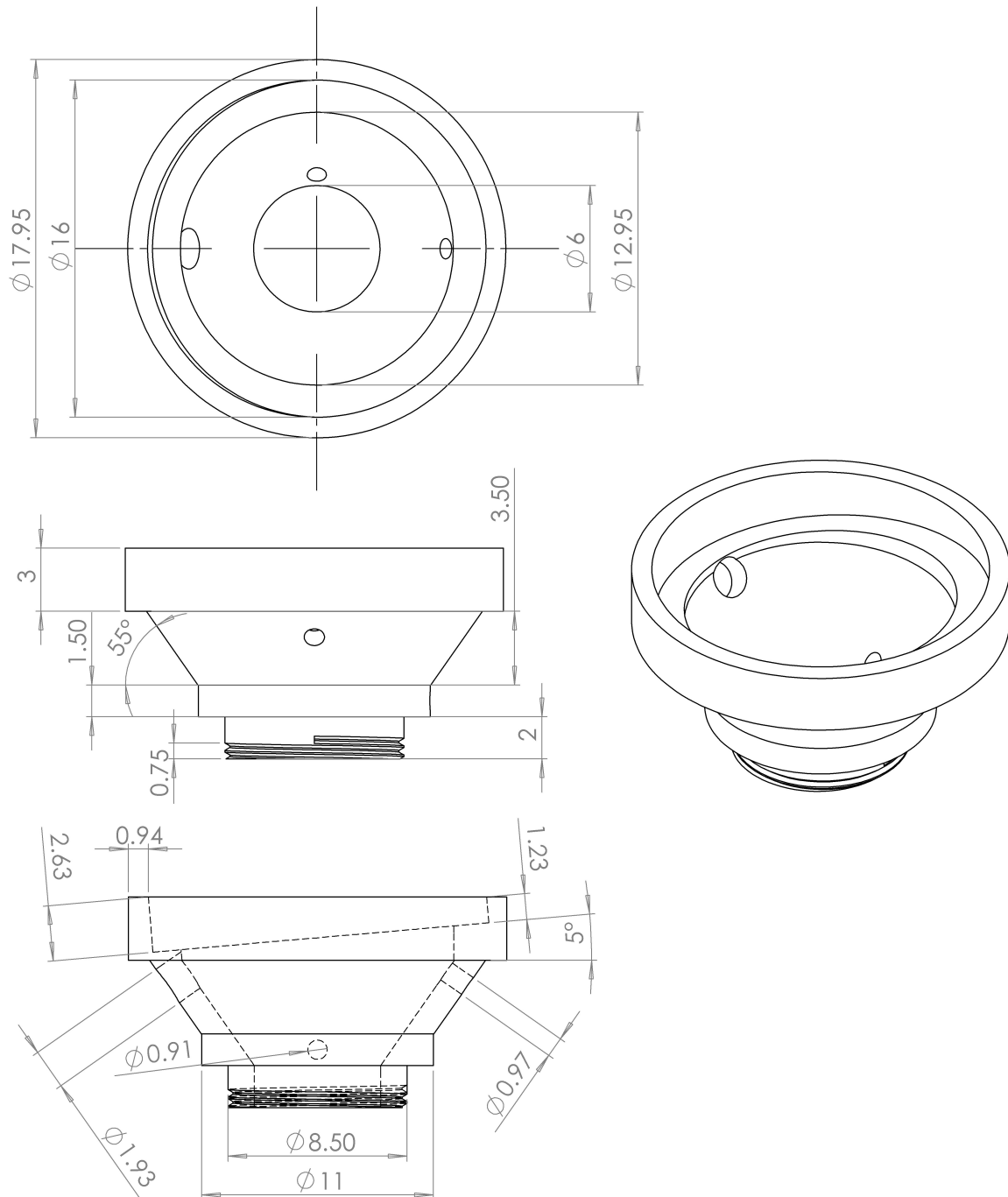
Figure 4.10: Engineering drawing of the coupler designed and manufactured for use in this study. All linear dimensions shown are in millimetres.
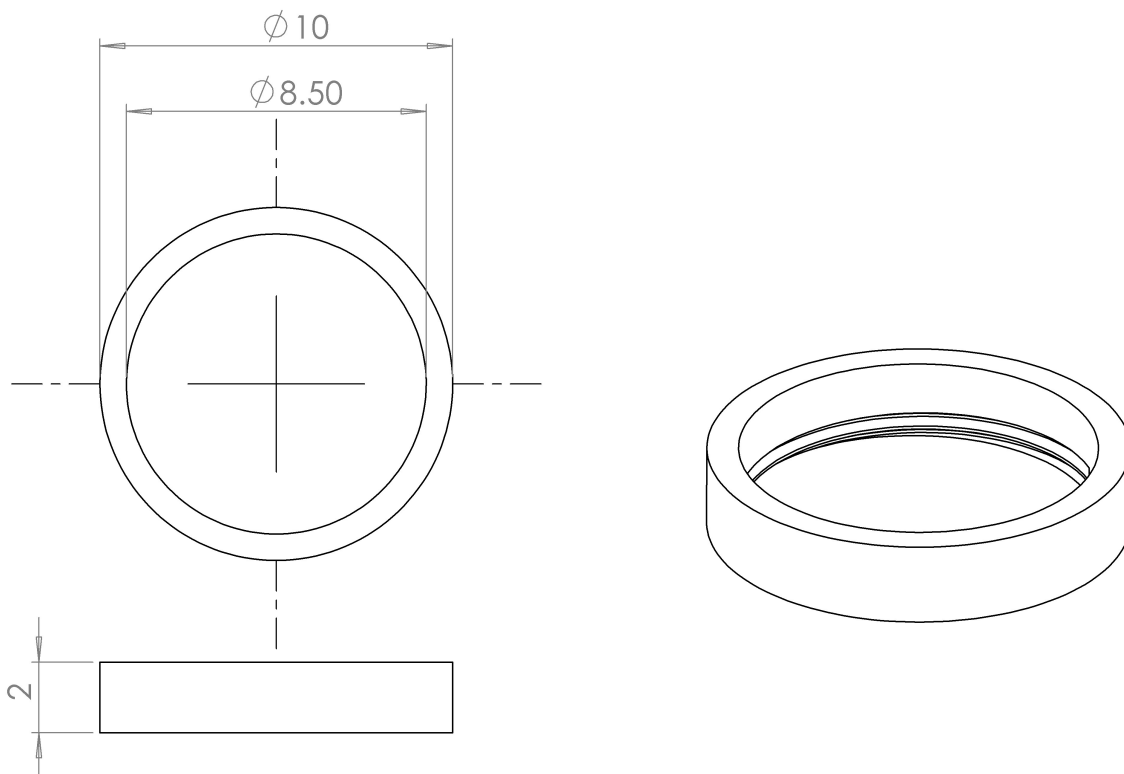
Figure 4.11: Engineering drawing of the washer designed and manufactured for use in this study. All dimensions shown are in millimetres. Threads are on the inside, at the bottom.

The previous coupler design includes a washer that is glued with dental cement to the wall of the bulla surrounding the opening of the ear canal. The base of the coupler is then attached to the upper surface of the washer with the same adhesive. The coupler is cylindrical in shape with a flat surface at the top for the anti-reflective glass window. The window is coated on both sides with a 633 nm anti-reflective V-coat (Edmund Optics) to reduce reflections. A ventilation tube is inserted into the coupler to regulate the pressure and to prevent an increase in humidity inside the coupler that would otherwise interfere with the signal of the laser. The design has a number of drawbacks. (1) From certain viewing angles, the edges of the eardrum are obstructed by the top inner edge of the coupler due to its narrow cylindrical shape. (2) No coating is 100% anti-reflective and residual reflections are directed back towards the laser head. (3) Finally, since the coupler is secured

to the washer with dental cement, it cannot easily be removed and replaced during the measurement process. This makes it difficult to perform a number of useful tasks, such as adding beads, re-hydrating the eardrum, changing the location of beads and investigating the use of alternative reflective materials. Removal of the coupler after the cement has dried can lead to small fragments falling onto the surface of the eardrum, introducing unwanted mass loading and damage to the membrane.

While addressing the limitations of the previous design, the new coupler must also satisfy other design criteria. The major issues are discussed in the following sections.

4.6.2 Resonance frequency

Acoustical resonance within an air-filled cavity involves the formation of standing waves corresponding to a set of 'natural' frequencies, resulting in amplitudes of vibration that are higher than at other frequencies. For the case of an air-filled rigid-walled tube at room temperature, open at one end, the nth longitudinal frequency f is related to the length of the tube L according to the equation

$$f = \frac{n \cdot v}{4 \cdot L} \qquad n = 1, 3, 5, ... \qquad \text{(Equation 4.1)}$$

(Beranek 1993) where v is the speed of sound in air at room temperature (340 m/s). (Frequencies obtained from Equation 4.1 are approximate because end effects are not considered.) Assuming that the first resonance ($n = 1$) occurs at the upper limit of our frequency range (10 kHz), we obtain a tube length of 8.5 mm. This means that, in order to avoid acoustical resonance within the sound chamber, the maximum length of the coupler must be less than 8.5 mm. However, we designed the coupler with an inside length of 8.2 mm, measured from the base to the glass window.

4.6.3 Residual reflections

The new coupler is designed with an angled slot for the glass window in order to prevent the residual reflection from being directed back into the vibrometer. We limit this angle to 5° in order to reduce the length of the upper cylindrical section of the coupler, thereby allowing the main conical section to be longer.

4.6.4 Eardrum visibility

The conical design of the coupler features an inside diameter of 16 mm at its upper end, converging to an inside diameter of 6 mm at its base. This base diameter is large enough to permit a full view of the opening of the ear canal but not so large as to obstruct the ventilation hole drilled into the bulla. As shown in Figure 4.12, the outer edges of the eardrum that were obstructed by the top inner edge of the previous coupler are now visible.

4.6.5 Removal and replacement

The design of the new coupler features a base with a set of fine threads machined onto the outer surface. The threads allow for removal and replacement to the same location during the experiment. As mentioned previously, once the dental cement has dried the coupler is threaded into the washer until the cylindrical rim of the coupler makes contact with the upper surface of the washer, creating an acoustic seal. (As shown in Figure 4.11, the washer is designed with threads on the bottom part of its inside surface.)
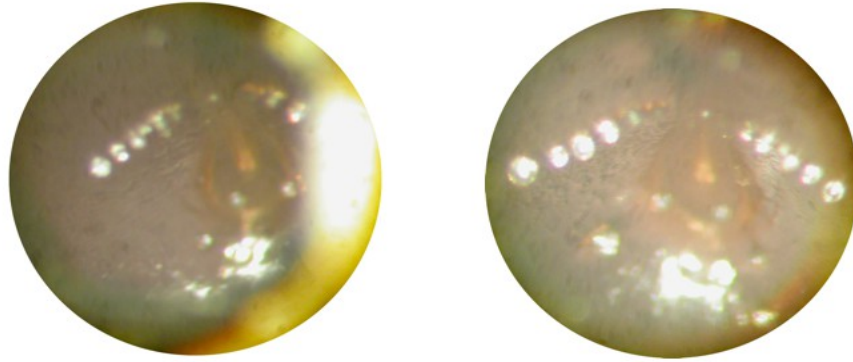
Figure 4.12: Microphotographs of the same eardrum with the previous coupler (left) and the newly designed conical coupler (right). Visibility of beads on the right side of the photograph of the previous coupler is obstructed, while all beads are clearly visible with the new coupler.

4.7 Coupler manufacture

4.7.1 Introduction

The new coupler was manufactured using both a computer numerical controlled (CNC) lathe (Quick Turn 20N, Mazak, Cambridge, Canada), shown in Figure 4.13, and a CNC vertical milling machine (VMC 4020, Fadal, Charlotte, NC), shown in Figure 4.14. Both machines are located at G. Industries in Montréal, Québec, where the machining was performed. The operations carried out on the two machines are described in the following sections.

Figure 4.13: CNC lathe machine with computer interface

Figure 4.14: CNC vertical milling machine with computer interface

4.7.2 Computer numerical controlled lathe

The G-code file exported directly from SolidWorks was uploaded to the computer of the CNC lathe. G-code is the numerical-control programming language that is used to specify the operations performed on the machine (type of motion, speed, feed mode etc.). The computer interface of the machine provides a simulated view of the process and also allows the user to modify the uploaded program.

The process of machining the outside of the coupler on the lathe is illustrated in the multiple panels of Figure 4.15. A 1-inch diameter aluminum bar is mounted in the chuck of the lathe and rotated at 1200 revolutions per minute (RPM) for roughing passes and at 1600 RPM for finishing passes. First, a facing pass is performed with a roughing tool: the material is removed from the end of the workpiece to produce a smooth even surface. The result of this operation is illustrated in Figure 4.15A. Multiple roughing contour passes are then performed with another roughing tool, shown in Figure 4.16. Material is removed with a maximum incremental depth of $0.15''$ until only about $0.1''$ of extra material is left to be removed. (Removal of more than $0.15''$ of material may lead to damage of the cutting tool.) Illustrations of the workpiece following a single pass and multiple passes are shown in Figure 4.15 panels B and C respectively. Multiple finishing contour passes are then performed with a finishing tool. Material is removed with a maximum incremental depth of $0.03''$ until the specified dimensions are obtained. The workpiece after this operation is illustrated in Figure 4.15D. After a cylindrical rim is created near the base of the coupler (Figure 4.15E), a threading tool is used to machine a set of threads at the base of the coupler with a pitch of 0.0275 in (0.7 mm) and a pitch diameter of 0.3250 in (8.25 mm). The threads are shown in Figure 4.15F. Throughout the process, a generous amount of aluminum cutting fluid (Relton 04Z-A9, Relton Corporation, Arcadia, CA) is continuously applied to the cutting tool and workpiece (Figure 4.16). The fluid provides lubrication in order to prevent damage to the cutting tool and to maintain a stable workpiece temperature.
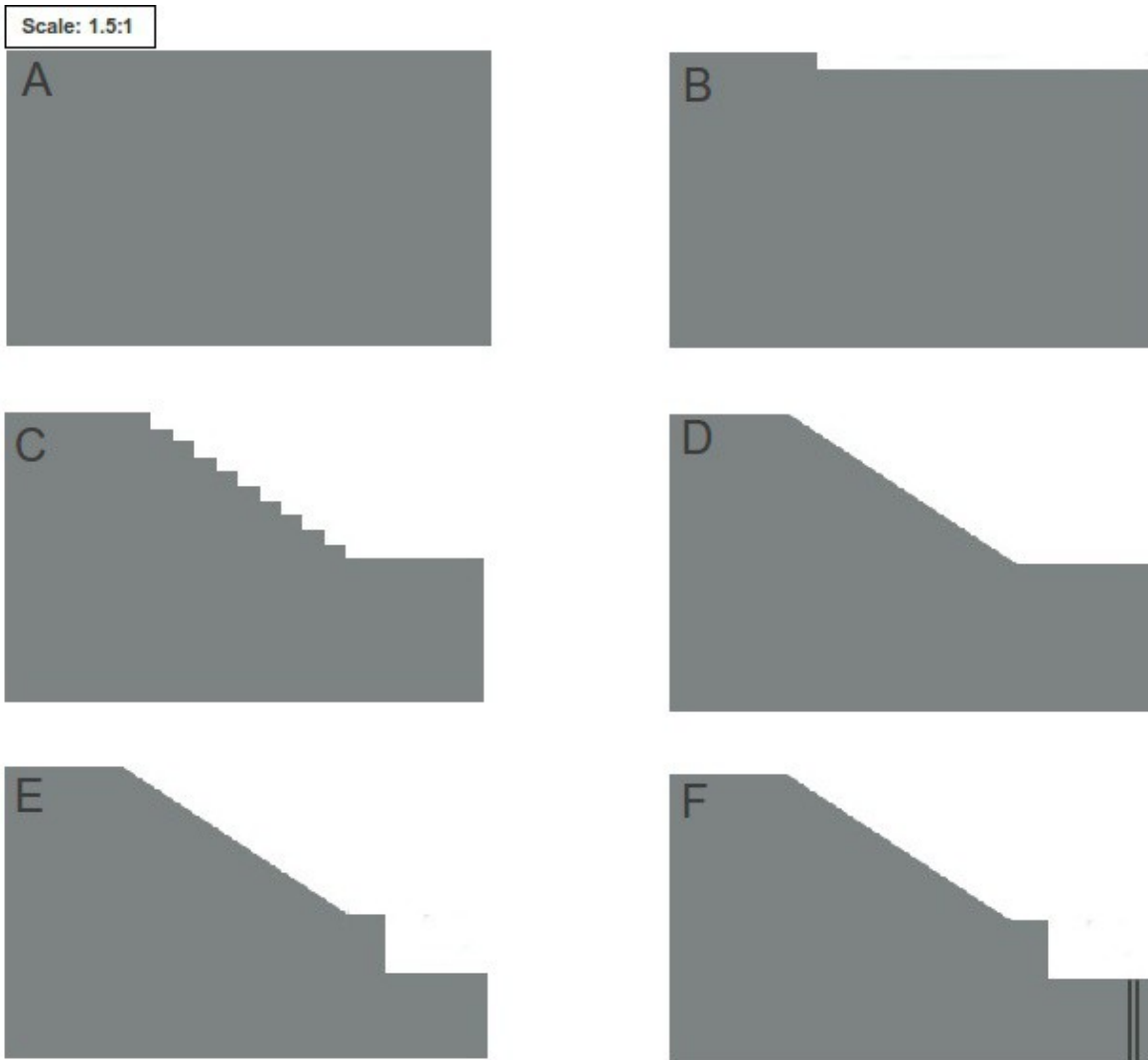
*Figure 4.15: Schematic diagrams of the workpiece at various stages of the CNC lathe operation (side view) **A.** Aluminum cylindrical workpiece after the facing pass. **B.** Workpiece following the first pass with the roughing tool. **C.** Workpiece following several passes with the roughing tool. After each pass the tool is translated a small distance to the right, resulting in a series of steps. **D**. Workpiece following multiple passes with the finishing tool, used to smooth the steps. **E.** Workpiece following the machining of a cylindrical rim at the base of the coupler. **F.** Workpiece following the machining of threads.*
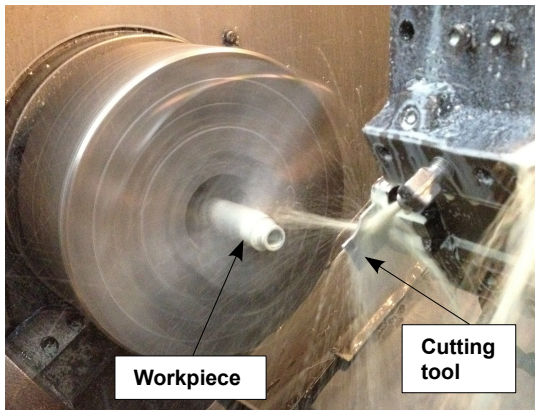
Figure 4.16: The roughing tool approaches the workpiece as it spins very rapidly about its long axis. Cutting fluid is applied to the cutting tool and workpiece continuously during the machining process.

Figure 4.17: Photograph of the workpiece mounted in the chuck (stationary) between lathe operations. The chuck is tilted to facilitate the mounting process and is untilted during machining.

For machining the inside surface of the coupler, the workpiece was held in the same chuck as used for the machining of the outer surface. The chuck is tilted to facilitate the mounting process as shown in Figure 4.17, but is untilted during machining. The cutting tools were mounted into a boring bar to enable machining from the inside. A ¼″ centre drill was used to create an opening in the coupler and thereby establish the clearance required for the cutting tools. (During machining of the outer surface, clearance was not an issue because there was no interference between the material and the tip of the holder.) A boring roughing pass was then performed with a roughing tool (Figure 4.18). Similar to the roughing contour pass on the outside, material was removed horizontally from the inside surface in 0.15″ increments, until 0.1″ of material was left to be removed. A single finishing boring pass was then performed to remove the remaining excess material. Finally, the workpiece was "parted-off" to the desired length using a grooving tool.

The washer was also manufactured on the CNC lathe. The threads on the inside surface of the washer match the thread size on the outside of the coupler.

*Figure 4.18: Boring tool used to remove material from the inside
surface of the coupler.*

4.7.3 Vertical milling machine

After completing the lathe operations on the coupler, the workpiece is brought to the
vertical milling machine for final operations. In this case the workpiece is held stationary in
a chuck and the cutting tool is spinning rapidly. Due to the thin, malleable walls of the
coupler, the ordinary chuck of the milling machine would result in warping of the coupler.
A specialized chuck of unknown manufacturer, more commonly known as a collet, was
therefore used to support the coupler over a large part of the circumference, rather than at a
small number of points. Top and bottom views of the collet are shown in Figure 4.19. The
collet is cut radially and threaded on the inside. With the bolt loosened, the coupler is
mounted around the upper portion of the collet. Tightening of the bolt results in the
expansion of the upper portion of the collet, resulting in a firm hold on the inside walls of
the coupler. The collet is then tilted 5° and a circular pocket is cut for the glass window.
Drill bits of different sizes are then used to drill three holes: #62 (0.965 mm) for the
ventilation tube, #57 (1.092 mm) for the microphone tube and #45 (2.083 mm) for the
speaker tube. The hole for the microphone is located at the bottom end of the coupler in
order to record the sound pressure as close as possible to the vibrating eardrum. During
drilling, the coupler is oriented such that each hole is drilled perpendicular to the surface.
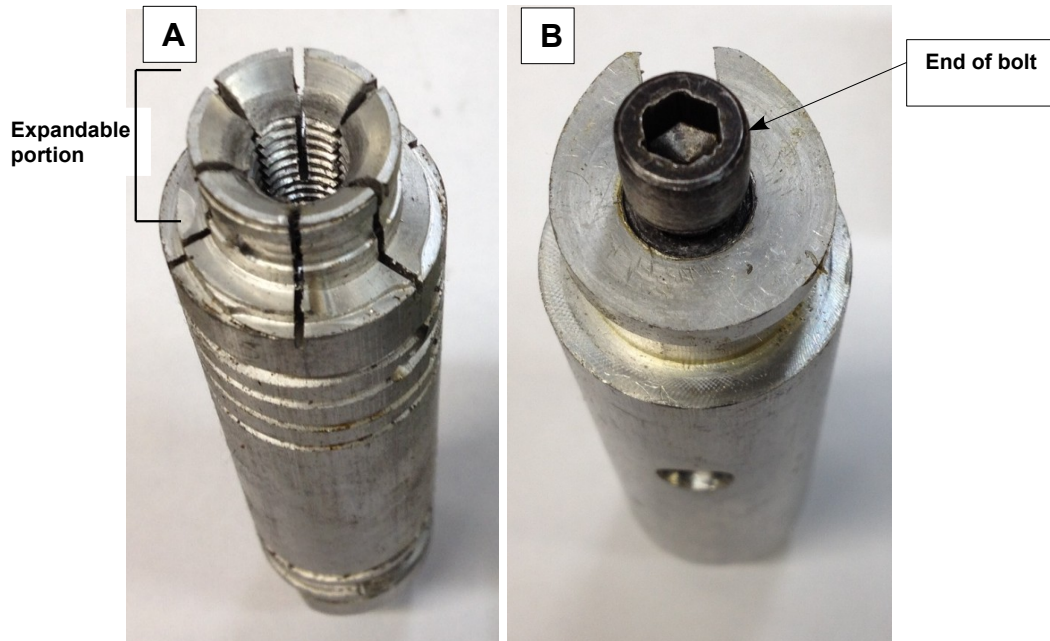
Figure 4.19: **A.** *Top view of the specialized chuck or collet used to hold the coupler during milling operations. The coupler is mounted around the top expandable portion.* **B.** *Bottom view of the collet. A bolt is tightened to expand the upper walls.*

4.8 Pressurization device

4.8.1 Background

One of the objectives of this study was to improve an existing pressurization device in order to perform middle-ear vibration measurements in the presence of static pressures. The device was started as a student project (Ding, 2011), but it required a number of improvements and modifications for this study. The final pressurization device used in experiments is shown in Figure 4.20. The various components are discussed in detail in the following sections.
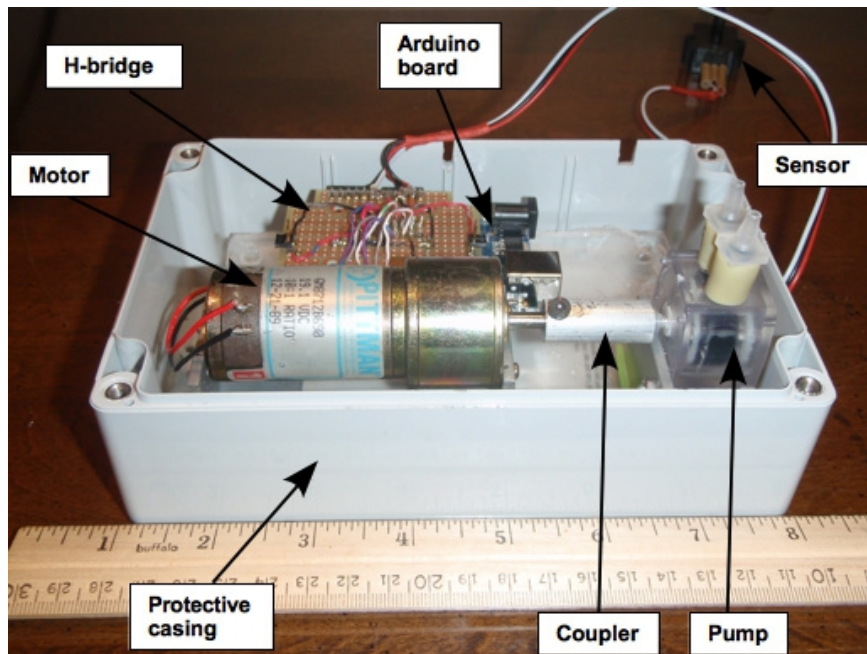
Figure 4.20: Pressurization device including sensor, controller, motor and pump.

4.8.2 Hardware components

4.8.2.1 Electronic components

The pressurization device is based on an Arduino Uno (SmartProjects, Strambino, Italy) micro-controller board, shown in Figure 4.21. Arduino is an open-source development kit. The original printed circuit board (PCB) design files (Eagle PCB, http://www.cadsoftusa.com, retrieved 2012 June 1) for the Arduino hardware are licensed under a Creative Commons Attribution Share-Alike licence, allowing for both personal and commercial derivative works. The Arduino software is also open-source, licenced under the GNU Lesser General Public License. This means that the source code is included with the compiled version, and modification is not only possible but also encouraged. The Arduino software includes libraries with functions for many common tasks.

Attached to the Arduino board is an H-bridge (L298HN, STMicroelectronics, Geneva, Switzerland) for the motor control. An H-bridge is an electronic circuit that, as shown in

Figure 4.22, consists of transistor switches located in the vertical branches of the 'H'. Modifying the configuration of the switches (open/closed) allows voltage to be applied across the load (DC motor), giving control of forward and reverse operation of the motor. An H-bridge can also be used to start and stop the motor. If either the 'low-side' or 'high-side' switches are open simultaneously on the vertical branches, the terminals are shorted and the motor ceases operation.

The amplified low-pressure sensor (20 INCH-D-4V, ALLSENSORS, Morgan Hill, CA) shown in Figure 4.23 was chosen based on the pressure ranges that are investigated in this study. The pressure range of the sensor is 0 to ±30 in H_2O (0 to ±7.5 kPa) with a 0 to 4 V output. The claimed linearity of the sensor is 0.05% of full scale (http://allsensors.com, retrieved 2012 June 1).

Figure 4.21: Arduino Uno micro-controller board (Source: http://www.arduino.cc, retrieved 2012 June 1)
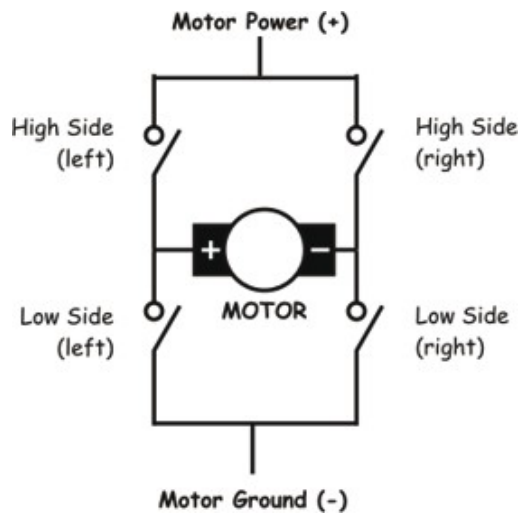
Figure 4.22: Simplified schematic
diagram of an H-bridge
(Source: http://www.mcmanis.com,
retrieved 2013 December 1)
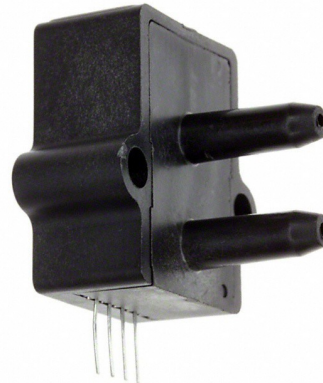
Figure 4.23: 20 INCH-D-4V
amplified low-pressure sensor
(Source: http://www.allsensors.com,
retrieved 2012 June 1)

4.8.2.2 Mechanical components

The mechanical components of the system consist of a brushless DC motor (GM8712D690, Pittman Motors, Harleysville, PA) and a peristaltic pump of unknown manufacturer that was obtained from Caswell Inc. (Lyons, NY). The motor rotates at a fixed speed of approximately 240 rpm and its shaft is connected to the pump by means of a custom-manufactured cylindrical link. Although no flexibility is built into the motor-pump link, the pump is mounted onto a rubber pad to achieve the same effect. A schematic diagram of a bi-directional peristaltic pump is shown in Figure 4.24. The fluid (air) is pumped through a flexible hose inside the pump casing. The pumping principle of peristalsis is based on alternating compression and relaxation, forcing the fluid through the tube. The pump is capable of generating either positive or negative pressures, determined by the direction of rotation of the motor shaft. The peristaltic pump is also self-sealed, capable of maintaining a desired static pressure without operating. This allows us to perform vibration measurements without interference from noise due to the operation of the mechanical components. The pumps of Figure 4.25 were considered but were not used in this study.

Given that each pump is uni-directional, both pumps would be required. They are advantageous due to their mechanical simplicity, eliminating the need for a separate motor-to-pump coupler. However, a special arbitration valve would be required to maintain a desired pressure without pump operation, making the peristaltic pump a more practical choice for this study.
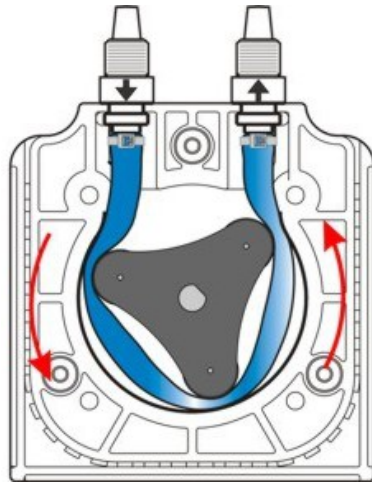
Figure 4.24: Schematic diagram of a peristaltic pump (Source: http://www.bluwhite.com, retrieved 2013 December 1)

Figure 4.25: Two uni-directional pressure pumps that were considered but finally were not used in this study.

4.8.3 Software components

An Arduino 'sketch' (or short piece of software code) was written to control the microcontroller interaction with the motor-pump mechanism. The program contains two variables, 'maintenance_limit' and 'half_rotate_limit', that can be modified by the user. 'Maintenance_limit' defines a range for an acceptable change in pressure. If the pressure falls outside of this range, the motor and pump will resume operation in order to achieve the specified pressure. The purpose is to avoid the occurrence of motor and pump noise during data acquisition. In this study the system was able to accurately maintain the desired pressure for long enough (± 5 Pa over > 90 s) that the pump never needed to be activated during a measurement. The variable 'half_rotate_limit' is used to prevent an overshoot of the specified pressure value. For instance, for a 'half_rotate_limit' of 25, once the pressure

comes to within 25 Pa of the target pressure the controller will use half rotations of the motor to slowly reach the desired pressure. Using 'half_rotate_limit' is slightly more time-consuming than manually obtaining a pressure, so it was not used for parts of the study where many measurements were desired and time was an important constraint.

Python is a general-purpose high-level programming language. A Python function was developed that sends commands from a laptop computer to the microcontroller. It requires two inputs: 'masterPause' and 'pressureVal'. 'masterPause' is a Boolean variable that controls the operation of the motor. A value of 0 indicates that the motor shaft rotates and a value of 1 indicates that the motor shaft does not rotate. 'pressureVal' is an integer variable ranging from 0 to 255. Once the specified value is sent to the Arduino sketch, a 10-bit analog-to-digital converter outputs a pressure value ranging from 0 to 1020 integer pressure-sensor units. The relationship between these integer units and a standard pressure unit (Pascal) was determined by a calibration procedure.

4.8.4 Pressurization device calibration

Based on the integer pressure-sensor values ranging from 0 to 1020, we determined experimentally that a value of 460 corresponds to ambient pressure. Values less than 460 correspond to negative or under-pressures in the cavity and values greater than 460 correspond to positive or over-pressures. Prior to its use in this study, the pressurization device was calibrated with a U-tube water manometer. The setup is presented in Figure 4.26: one end of the manometer tube was connected by means of a Y-adaptor to the pressure sensor and to a second tube that extends to the nozzle of the peristaltic pump. Multiple pressures were then applied to the U-tube manometer, ranging from 120 to 780 integer-pressure units. For each pressure, the difference in water level between the left and right sides of the U-tube manometer was recorded. The pressure P in Pascals was then calculated according to the equation

$$P = \rho \, g \, h \qquad\qquad \text{(Equation 4.2)}$$

where ρ is the density of water in kg/m^3, g is the acceleration due to gravity in m/s^2 and h is the liquid-level difference in m. The resulting calibration curve is presented in Figure 4.27 and the result of a linear regression analysis of the curve is

$$y = 12.0\,x - 5525 \qquad\qquad \text{(Equation 4.3)}$$

where x is the pressure-sensor value and y is the corresponding pressure in Pascals.

4.8.5 Buffer volume

The volume of the middle-ear cavity in the Mongolian gerbil is approximately 0.2 ml (Ravicz et al. 1992). For the air displacement of our pump, one complete rotation of the motor shaft would correspond to a pressure change of over 1000 Pa if applied directly to the middle ear. Since we wish to perform measurements at smaller pressure intervals than that, we connect a buffer volume to the middle-ear cavity. The buffer volume helps control the rate at which air is entering and exiting the middle-ear cavity. One of two buffer volumes was used in each experiment in this study: a 35-mm film canister with a volume of approximately 35 ml, and a glass bottle with a volume of 150 ml. Both buffer volumes are shown in Figure 4.28. One complete rotation of the motor shaft corresponds to a pressure change of only 40 Pa in the larger glass bottle compared with 150 Pa in the film canister. For this reason, the film canister is more suitable for studies involving a large number of measurements: pressures are more quickly established so drying of the eardrum is reduced. On the other hand, the glass bottle is more suitable for studies that demand accurate establishment of a series of consecutive pressures without overshoot, although it is more time consuming.

The film canister is closed with a lid and the beaker is closed with a rubber stopper. Holes (1 cm diameter) are drilled into the lid and stopper with a hand drill and the tubes are connected with carpenter's glue (Lepage, Brampton, ON). The buffer volumes are additionally sealed with the same glue followed by a putty-like adhesive (Blu-Tack, Bostik,
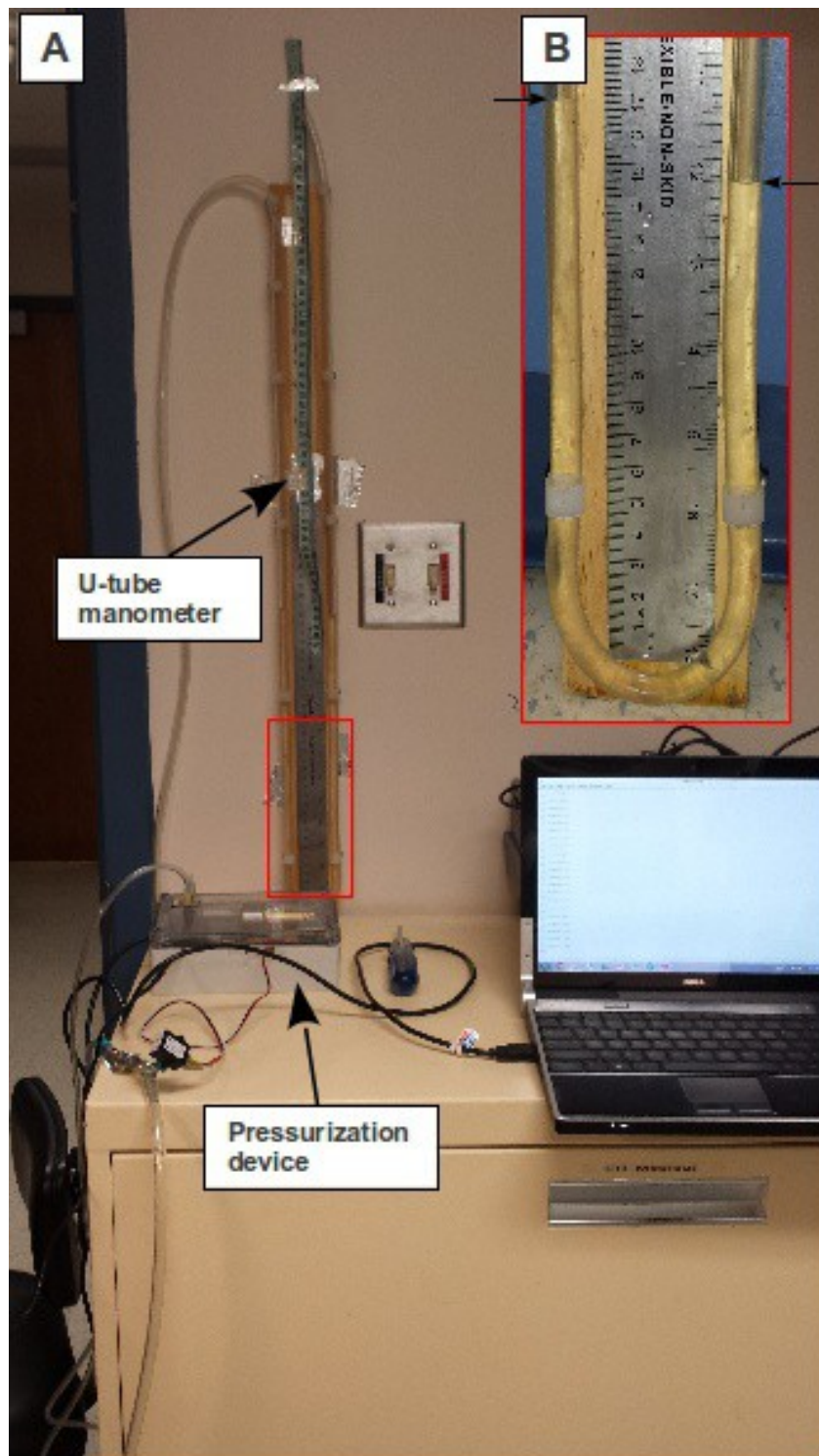
Figure 4.26: **A**. *Pressurization device calibration setup.* **B**. *Close-up of the U-tube manometer. The arrows correspond to the water levels used to calculate the pressure in the system.*
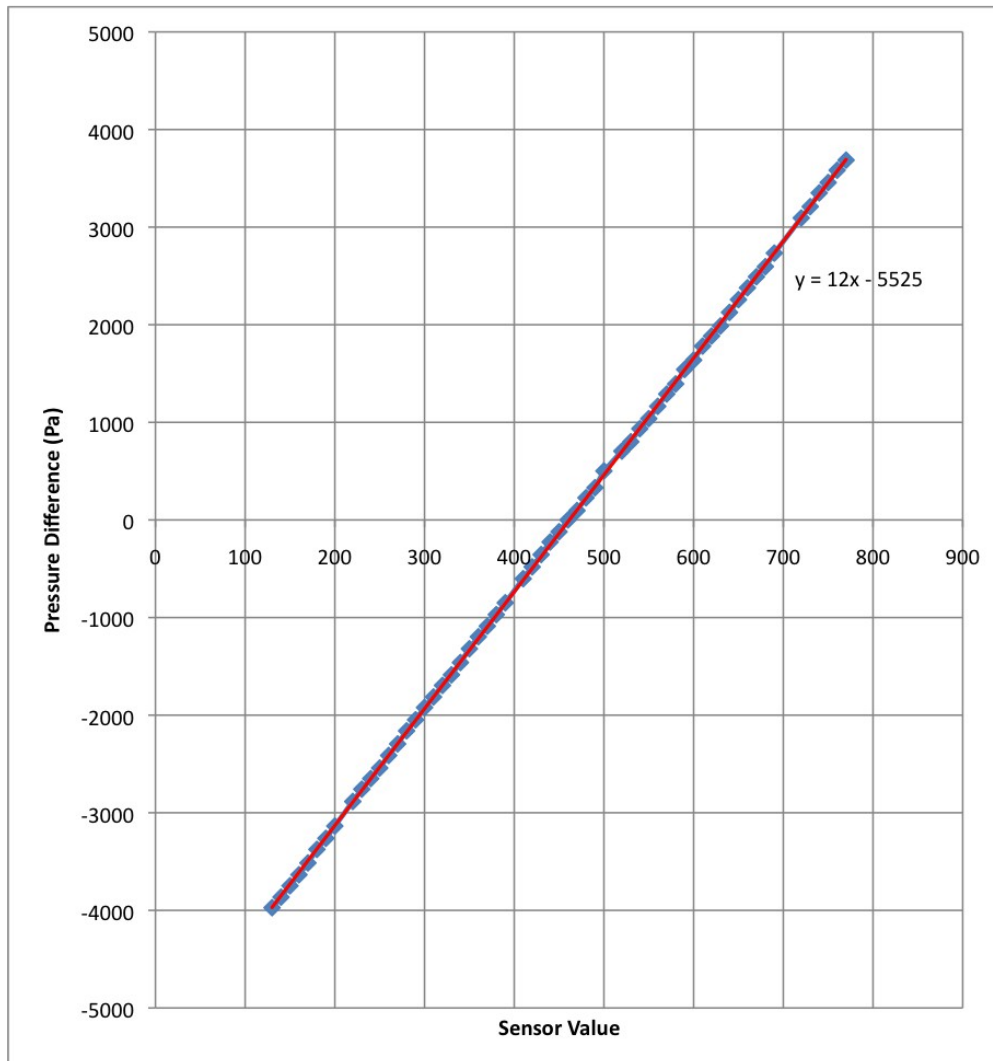
Figure 4.27: Pressurization device calibration data and fitted straight-line.

Paris, France) to eliminate any possible air leaks. Consequently, the volumes are capable of maintaining a pressure for an extended period of time.

*Figure 4.28: Glass bottle (left) and film canister (right)
used as buffer volumes in this study. Only one buffer volume
is connected to the middle-ear cavity in each experiment.*

4.9 Experimental protocols

4.9.1 Introduction

Two experimental protocols were used in this study to perform vibration measurements on the gerbil eardrum under static pressure. The first protocol was used in gerbils A, B, C and D, and was designed to study the effects of static pressure on the amplitude response of the eardrum over multiple cycles. Protocol 1 is described in Section 4.9.2. We then decided to use a different protocol for gerbils E, F, G and H. Protocol 2, described in Section 4.9.3, is the same as the one used by Decraemer's group in their studies related to static pressurization (e.g., Dirckx & Decraemer 1991; Dirckx & Decramer 2001).

4.9.2 Protocol 1

Each cycle of protocol 1 consisted of 9 measurements as shown in Table 4.2. The measurement cycles were repeated for pressures of 0.25, 0.5, 1.0, 1.5, 2.0 and 2.5 kPa. We

started with the 0.25-kPa pressure cycle, performed at the manubrium, then repeated for the next highest level of pressure, and so on. The 6 cycles on the manubrium were then repeated on the pars tensa. Thus, 12 cycles in total were performed in each gerbil ear. The time interval between measurements was approximately 45 s: we set the pressure, waited for 25 s, recorded the vibration measurement and then waited until the end of the 45-s period before setting the next pressure. Each cycle of 9 measurements was therefore performed over a timespan of 10–12 min. The film canister was used as a buffer volume because protocol 1 involves a large number of measurements. Pressure settings were performed with an accuracy of ±10 Pa.

Table 4.2: Sequence of measurements at a specific pressure in each cycle of protocol 1. Positive and negative refer to the pressure in the middle-ear cavity.

Measurement #	Pressure specification
1	Unpressurized
2	Positive pressure
3	Unpressurized
4	Negative pressure
5	Unpressurized
6	Positive pressure
7	Unpressurized
8	Negative pressure
9	Unpressurized

4.9.3 Protocol 2

Measurements for protocol 2 were performed at pressures of $0, \pm 0.25, \pm 0.5, \pm 1, \pm 1.5, \pm 2$ and ± 2.5 kPa. Each cycle began with a positive-pressure sweep consisting of 6 steps from 0 to +2.5 kPa then unloading in 6 steps back to zero, followed by a negative-pressure sweep that consisted of loading to −2.5 kPa and finally unloading back to zero. Measurements were recorded at each listed pressure in each sweep. In gerbil E we performed three cycles on the manubrium and in gerbils F, G and H we performed three cycles on the pars tensa.

The time between measurements was 20 s. Each cycle was performed over a timespan of 20–24 min. The glass bottle was used as a buffer volume for protocol 2 in order to reduce the rate at which we pressurized the middle-ear cavity, so that pressures could be established precisely and without overshoot.

4.10 Laser Doppler vibrometry

4.10.1 Introduction

Over the last two decades, laser-based methods for measurement of mechanical vibrations have become increasingly popular, primarily due to the non-invasive nature of the techniques. Vibration measurements are important in a number of fields, from industrial applications such as process monitoring and quality control to biomedical applications such as eardrum measurements. Today, LDV is the most widely used laser-based technique (Righini 2009). It is an optical interferometric method that uses the Doppler effect to measure the instantaneous velocity or displacement of a target without mass loading. In Section 4.10.2 the basic theoretical principles of optical interferometry are discussed, followed by an overview of the Polytec laser Doppler vibrometer used in this study in Section 4.10.3; both sections are largely based on Hariharan (2007).

4.10.2 Optical interferometry

Optical interferometry is based on interference between two superimposed light waves. Two such waves will reinforce each other if they are in phase and will tend to cancel each other if they are out of phase; complete cancellation of two waves will only occur if they are precisely 180° out of phase and have the same amplitude. Optical interferometry is most effective with a light source emitting light at a single wavelength, in other words a single-colour (monochromatic) light source. The use of the laser as a monochromatic light source eliminates many limitations of conventional light sources. In addition to being monochromatic, laser light is also highly collimated, meaning that it will spread little as it

propagates and can therefore be focused at a precise spot over a long distance (Allmen 1987). There exist several types of lasers, differing in the lasing material used to emit the light and in the specific wavelength of light emitted. Many interferometric devices (including the Polytec vibrometer used in this study) use a low cost helium-neon (He-Ne) laser with a wavelength of 633 nm that supplies continuous red light. The vibrometer used in this study uses a Class II laser and is therefore eye-safe.

There are several types of optical interferometric devices that are used for making vibration measurements. The fundamental principle of LDV is the Doppler effect, defined as the change in frequency of a wave perceived by an observer moving relative to the wave source. We notice this as a sound shift when an ambulance drives by, for instance. In a vibrometer, a coherent laser beam is projected onto the vibrating surface and the light reflected back is subject to a change in frequency (Doppler frequency shift) proportional to the velocity of the vibrating surface. This frequency shift f_D is given by

$$f_D = \frac{2v}{\lambda}$$ (Equation 4.4)

where λ is the wavelength of the laser beam and v is the velocity of the vibrating surface.

4.10.3 Polytec laser Doppler vibrometer

4.10.3.1 Principle of operation

The vibrometer used in this study is a single-point heterodyne interferometric device. As shown schematically in Figure 4.29, a He-Ne laser beam with frequency f_0 is projected from the laser head and split into measurement and reference beams by means of a beam splitter (BS1). The measurement beam is directed through a second beam splitter (BS2) and is then projected onto the vibrating surface. The reflected beam is subject to a Doppler frequency shift f_D. The reference beam is directed through a Bragg cell which shifts the frequency of the reference signal and generates a carrier signal with frequency $f_0 + f_B$. The

purpose of the Bragg cell is to disambiguate the direction of movement of the investigated object. Generally, the vibrating object produces the same interference pattern and therefore the same frequency shift whether it moves in a direction towards or away from the interferometer. The Bragg cell is placed in the path of the reference beam, modulating the frequency at the detector to 40 MHz if the investigated object is at rest. When the object moves away from the vibrometer, the frequency at the detector will be greater than 40 MHz, while a frequency below 40 MHz indicates that the object is moving in a direction towards the vibrometer head.

The output of the Bragg cell then passes through a third beam splitter (BS3) where it is made to interfere with the reflected measurement beam. The result is sent to the photodetector and the intensity is given by

$$I(t) = \left(E_M(t) + E_R(t) \right)^2 \qquad \text{(Equation 4.5)}$$

where E_M and E_R are the electric fields of the measurement and reflected beam respectively. These electric fields are given by

$$E_M(t) = E_m \cos\left(2\pi \left(f_0 + f_D \right) t + \phi_m \right) \qquad \text{(Equation 4.6)}$$

and

$$E_R(t) = E_r \cos\left(2\pi \left(f_0 + f_B \right) t + \phi_r \right) \ . \qquad \text{(Equation 4.7)}$$

Substituting Equations 4.6 and 4.7 into Equation 4.5 gives

$$I(t) = \left(\left(E_m \cos\left(2\pi \left(f_0 + f_D \right) t + \phi_m \right) \right) + \left(E_r \cos\left(2\pi \left(f_0 + f_B \right) t + \phi_r \right) \right) \right)^2 \ . \qquad \text{(Equation 4.8)}$$

Algebraically expanding Equation 4.8 and applying a trigonometric identity gives Equation 4.9:

$$I(t) = (E_m^2/2) + (E_r^2/2)$$
$$+ (1/2)\left(E_m^2 \cos\left(4\pi\left(f_0+f_D\right)t+\phi_m\right) + E_r^2 \cos\left(4\pi\left(f_0+f_B\right)t+\phi_2\right)\right)$$
$$+ E_m E_r \cos\left(2\pi(2f_0+f_B+f_D)t+\left(\phi_m+\phi_r\right)\right)$$
$$+ E_m E_r \cos\left(2\pi\left(f_D-f_B\right)t+\left(\phi_m-\phi_r\right)\right)$$

(Equation 4.9)

Given that the photodetector acts as a low-pass filter, high-frequency components are filtered out. In Equation 4.9, all terms with a frequency higher than (f_D-f_B) are well beyond the low-pass-filter cutoff frequency. Equation 4.9 is thus simplified to

$$I(t) = \left(E_m^2/2\right) + \left(E_r^2/2\right) + E_m E_r \cos\left(2\pi\left(f_D-f_B\right)t+\phi_m-\phi_r\right)$$

(Equation 4.10)

Defining $I_m = E_m^2/2$ and $I_r = E_r^2/2$, Equation 4.10 can be written as

$$I(t) = I_m + I_r + 2\sqrt{I_m I_r} \cos\left(2\pi\left(f_D-f_B\right)t+\left(\phi_m-\phi_r\right)\right)$$

(Equation 4.11)

Therefore, the output depends only on the difference between the Doppler frequency shift and the frequency offset created by the Bragg cell.
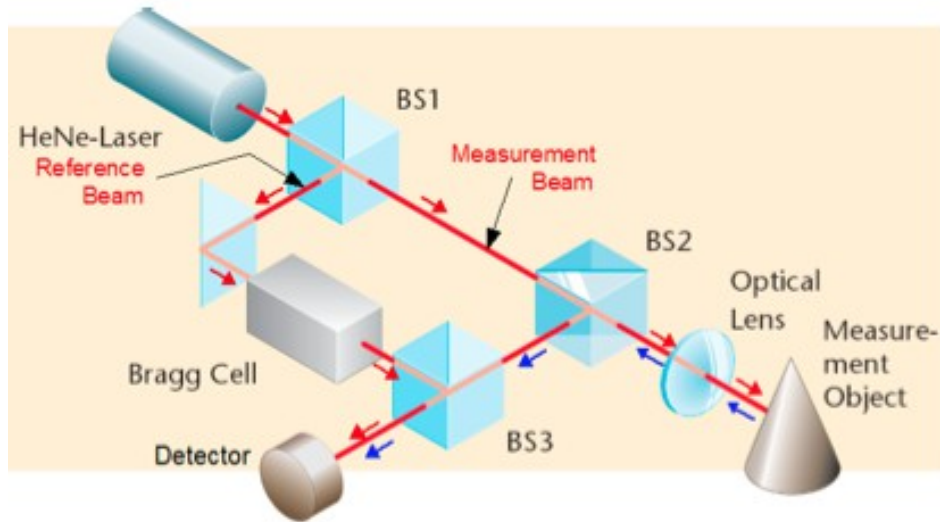

Figure 4.29: Schematic diagram of the operation of the laser Doppler vibrometer. Beam splitters BS1, BS2, BS3 split and recombine the HeNe-laser beam travelling towards the detector. (After polytec.com)

In our study the laser Doppler vibrometer measures velocity and integrates it to calculate displacement.

4.10.3.2 Vibrometer components

The vibrometer used in our study (HLV-1000, Polytec, Irvine, CA) is a 'hearing laser vibrometer' specifically developed to investigate the mechanics of the middle ear. Two main components of the vibrometer are a laser sensor head and a vibrometer controller unit. These two components are connected to each other with a fibre-optic cable that is not affected by mechanical vibrations. The laser head is mounted onto the operating microscope and a beam-positioning system on the laser head is equipped with a joystick that allows the user to manually deflect the laser beam to a precise location on the measurement object. The vibrometer controller unit is connected to the acoustical system and the data management system (DMS) by means of a junction box. The DMS is responsible for the generation of signals that drive the sound-delivery system and also for the acquisition and analysis of the audio and laser signals picked up by the microphone and sensor head respectively. The DMS hardware includes a 1.9-GHz AMD processor, 512 MB of RAM and an 80-GB hard disk. VibSoft 4.3 (Polytec) is the software used for the acquisition, visualization and manipulation of the measured signal in both the time and frequency domains. The software settings also allow for the specification of the frequency resolution and of the signal type (eg. burst random noise, white noise, pure tone, sinusoidal sweep, etc.) used as the input stimulus.

5.1 Introduction

In this chapter we present the effects of static pressurization on the vibration displacement response of the gerbil eardrum. For each gerbil in this study, the vibrations of two structures are investigated: the manubrium and the pars tensa, both at the level of the middle of the manubrium. In Section 5.2 we present the first unpressurized measurement on each structure in each gerbil, as well as the first pressurized measurement (either manubrium or pars tensa) in each gerbil. We address the variability between animals and provide a comparison with previously reported results. Measurements from protocol 1 and protocol 2 are then presented in Sections 5.3 and 5.4, respectively. For each protocol, we investigate the effects of multiple cycles of pressurization on the frequency response of the vibration displacement. Unless otherwise indicated, all responses are plotted on logarithmic frequency scales from 0.2 to 10 or 11 kHz, normalized with respect to sound pressure level. A discussion of the results is presented in Section 5.5.

5.2 First measurements

5.2.1 Unpressurized manubrium responses

The first measurement in each gerbil ear was performed on the manubrium prior to pressurization of the middle-ear cavity. The corresponding normalized frequency responses, including both magnitude and phase plots, are shown in Figure 5.1. In each plot, the solid line colour sequence of black, red, green, blue, cyan, magenta, yellow and grey corresponds to responses recorded in gerbils A to H, respectively. The magnitude and phase responses of gerbils A, F and G (black, magenta and yellow) exhibit irregularities at very low frequencies due to noise. At low frequencies, the other responses exhibit a response that is flat to within approximately ±1 dB, and the phase curves are close to zero (within 20°),

indicating that the middle ear is behaving as a stiffness-dominated system. As the frequency increases, a magnitude dip is observed in the range of 490 to 675 Hz, followed by a sharp rise to a peak in the range of 630 to 850 Hz. The phase curves show a maximum at a frequency corresponding to the sharp rise in magnitude. Our findings here are consistent with previous studies in which it was found that resonance of the normally flat pars flaccida results in these features in the response of the manubrium (and pars tensa) at low frequencies (e.g., Maftoon et al. 2013). The black dashed line in Figure 5.1 corresponds to the dark green measurement reported by Maftoon et al. (2013) in their Figure 4, recorded at the umbo with a partially retracted pars flaccida. Each umbo response from their study was very similar, so we present only one as a comparison. As mentioned in Chapter 3, unpressurized responses of the manubrium and the pars tensa are affected differently by two different pars-flaccida conditions at low frequencies: naturally flat, and retracted into the middle-ear cavity (e.g., Maftoon et al. 2013). Since their only flat-pars-flaccida manubrial measurements were made at the umbo, and not at the mid-manubrium level, we use an umbo response and multiply it by the ratio of the umbo and mid-manubrium responses in their Figure 5. Specifically, we obtain a ratio of 44.4/57.7 corresponding to the magnitude ratio of their light green curve to their grey curve, respectively. The resulting response is plotted in Figure 5.1. In our study, a flat pars flaccida was always observed under the microscope during the first unpressurized measurements. As shown in Figure 5.1, our responses exhibit a sharper rise of the flat-pars-flaccida feature, suggesting that their pars flaccida was not quite flat. (Maftoon et al. (2013) reported that the "magnitude-minimum/phase-maximum feature in the umbo response became gradually less distinct with a greater degree of retraction".)

The magnitude peak due to the pars flaccida is followed by a broad minimum in the response before the main middle-ear resonance. Table 5.1 lists the middle-ear resonance frequencies for each gerbil, ranging from 1.75 to 2.00 kHz. Maftoon et al. (2013) reported a similar range of 1.6 to 2.0 kHz. The maximum magnitude at resonance in each gerbil

ranges from 70 to 105 nm/Pa. Beyond resonance the frequency response starts to roll off, and above 4 kHz small irregularities are observed. Phase responses roll off slowly beyond the maximum, showing small irregularities at higher frequencies.
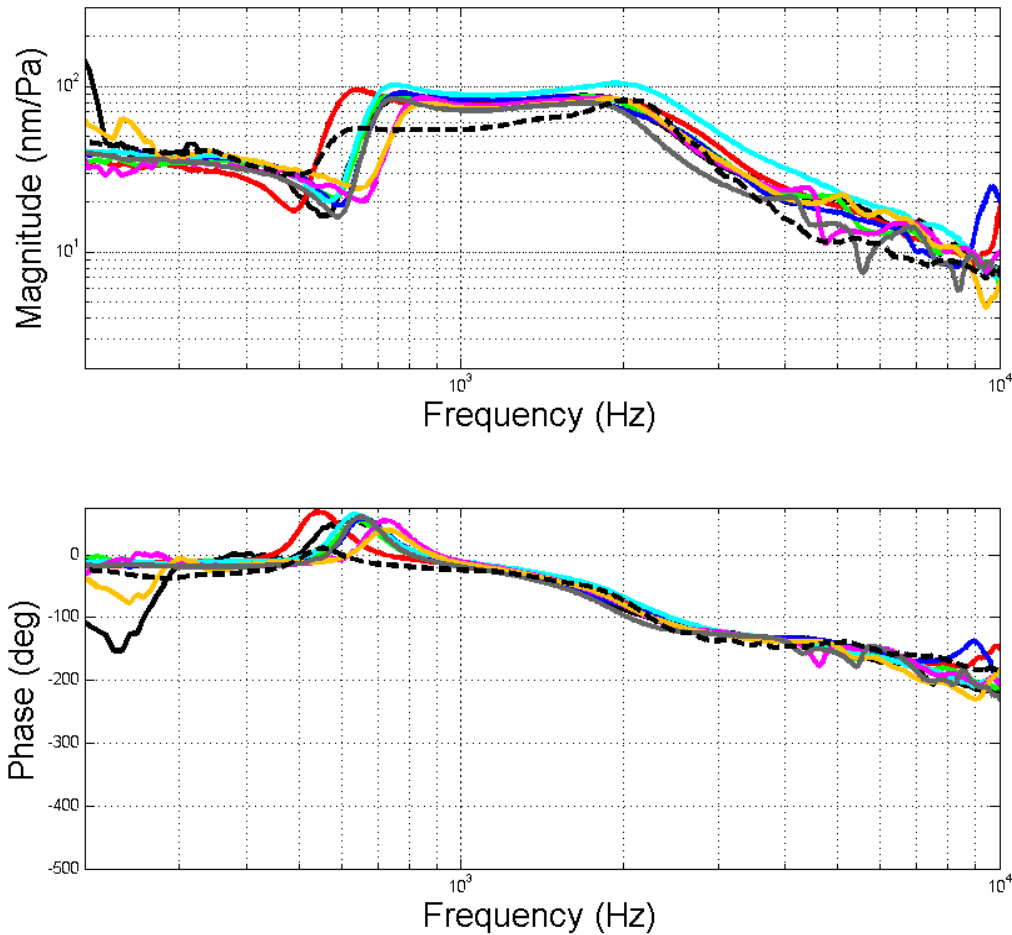
Figure 5.1: Normalized amplitude and phase frequency responses of the first measurement on the manubrium in each gerbil. The colour sequence of black, red, green, blue, cyan, magenta, yellow and grey corresponds to measurements recorded in gerbils A to H, respectively. The black dashed line corresponds to a measurement from Maftoon et al. (2013).

Table 5.1: Middle-ear resonance frequencies and estimated break-up frequencies in 8 gerbil ears.

Gerbil	Middle-ear resonance frequency (kHz)	Break-up frequency (kHz)
A	1.75	3.30
B	1.90	2.00
C	1.80	2.80
D	1.70	3.55
E	2.00	3.60
F	1.90	3.75
G	1.95	1.90
H	1.80	2.90

5.2.2 Unpressurized pars-tensa responses

Immediately following the first measurement on the manubrium, we performed a single unpressurized measurement on the pars tensa in each gerbil. The corresponding magnitude and phase frequency responses are shown in Figure 5.2, in the same format as for Figure 5.1. The pars-tensa responses are similar to the manubrium responses at lower frequencies, and again are influenced by the condition of the pars flaccida. Vibration magnitudes are higher on the pars tensa than on the manubrium. The average ratio of the first pars tensa and first manubrium response in each gerbil at a very low frequency (0.25 kHz) is approximately 1.35, comparable to the ratio of 1.4 obtained by Maftoon et al. (2013). The simple low-frequency response of the pars tensa becomes very complex at higher frequencies. A multitude of studies in the past (including Decraemer et al. (1989) in the cat, and Maftoon et al. (2013) in the gerbil) have reported the general observation that all points on the pars tensa move almost in phase with each other and with the manubrium up to a certain frequency. Beyond this frequency, phase differences increase and frequency-dependent magnitude differences are observed, demonstrating that the simple response has broken up and that a complex spatial pattern is present. The point where this occurs is termed the break-up frequency, arbitrarily defined by Maftoon et al. (2013) as the frequency

at which phase curves for different points on the pars tensa diverge by more than 15° (five times their calculated short-term variability of phase). Since we only study a single point on the pars tensa, we cannot provide direct evidence for the break-up frequency. However, we use a similar criterion and arbitrarily estimate the breakup point as the frequency at which the phase curve of the first pars-tensa measurement diverges from that of the first manubrium measurement by more than 15°. Breakup frequencies estimated for each ear are shown in Table 5.1, ranging from 1.90 to 3.75 kHz. Our breakup frequencies are somewhat higher than those reported by Maftoon et al. (2013), which ranged from 1.8 to 2.8 kHz. This difference may be due to the different estimation methods used in our study and theirs.
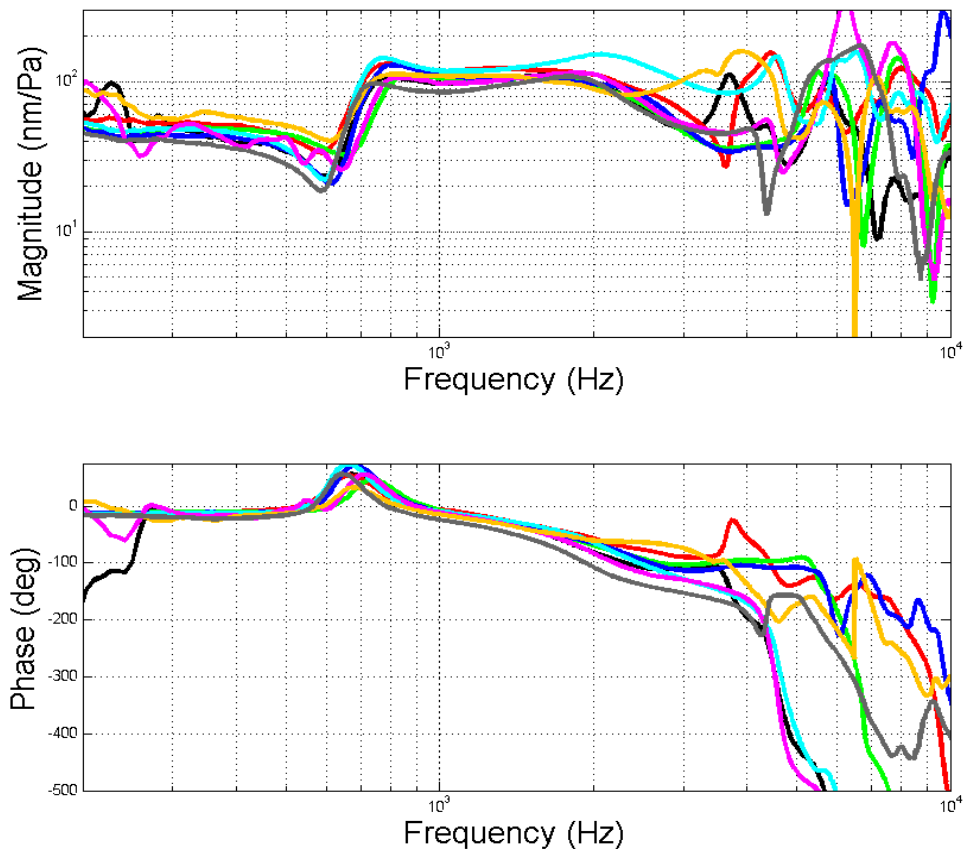
Figure 5.2: Normalized magnitude and phase frequency responses of the first measurement on the pars tensa in gerbils A to H. The line colours are the same as for Figure 5.1.

5.2.3 First pressurized response

Here we compare the first pressurized measurement, recorded at +250 Pa, in each gerbil ear. Subsequent measurements vary according to the protocol and are not compared. The frequency responses are shown in Figure 5.3, in the same format as for Figures 5.1 and 5.2. The responses in gerbils A to E correspond to measurements on the manubrium, and the responses in gerbils F to H correspond to measurements on the pars tensa. With the exception of the irregular low-frequency responses in gerbils A and F, pressurized magnitude responses on the manubrium and pars tensa are characterized by flat curves at low frequencies followed by gently increasing curves over the mid-frequency range. Magnitudes are lower than those of the corresponding unpressurized curves (cf. Figure 5.1). At higher frequencies, pressurized magnitude responses rise above the unpressurized responses and we see an magnitude peak. The pressurized pars-tensa responses increase to much higher magnitudes than the pressurized manubrium responses do. The abnormally high magnitudes in gerbils F and G are further discussed in Section 5.4.4. Compared with the unpressurized responses, pressurized phase responses on both the manubrium and pars tensa remain higher over the low-to-mid frequency range and then drop more rapidly at higher frequencies. At these high frequencies, the phase curves of the pars-tensa responses decrease more rapidly than the manubrium responses.

Phase responses are not presented in the remainder of this thesis because of the large amount data to be presented and because the phase does not add a great deal to the interpretation of the data.
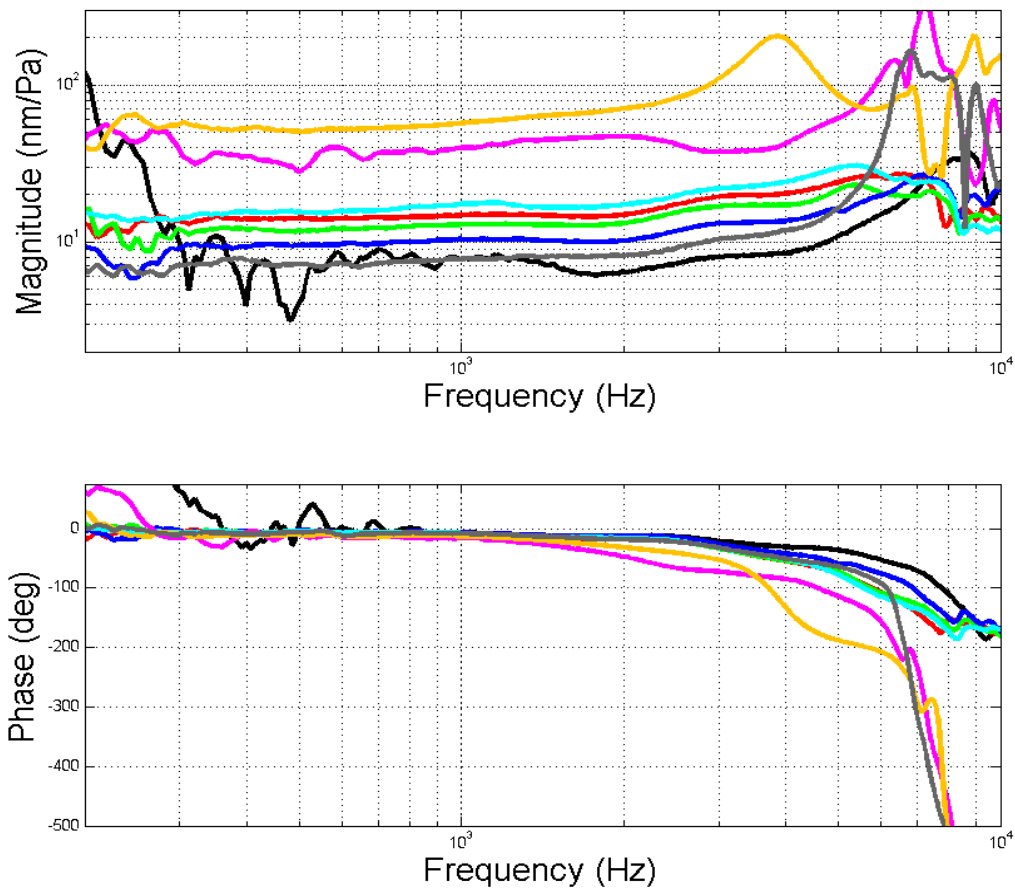
Figure 5.3: Normalized frequency responses of the first pressurized measurement in each of gerbils A to H. The measurements were on the manubrium in gerbils A to E (black, red, green, blue and cyan) and on the pars tensa in gerbils F to H (magenta, yellow and grey).

5.3 Pressurization protocol 1

5.3.1 Manubrium responses

In this section we present the effects of static pressurization on the vibration displacement response of the gerbil manubrium for protocol 1. Similar trends are observed in gerbils A to D so detailed results are presented only for gerbil D, in Figures 5.4 to 5.9. At 1.5 kHz for example, the average magnitudes of all of the unpressurized responses in gerbils A, B, C and D are 79, 78, 83 and 86 nm/Pa, respectively, calculated only from responses exhibiting the normal flat-pars-flaccida condition. This corresponds to a difference of less than 0.7 dB across all four gerbil manubria. Each figure includes five unpressurized responses as well as two positive-pressure responses and two negative-pressure responses. The first unpressurized response is represented by a black curve, and unpressurized responses immediately following positive and negative pressures are given by cyan and magenta curves, respectively. Positive-pressure and negative-pressure responses are represented by green and red curves, respectively. Responses belonging to the first part of the cycle have a solid line style, while responses belonging to the second part have a dashed line style. The line properties are summarized in Table 5.2.

Table 5.2: Sequence of measurements for each static pressure investigated. One complete cycle is shown, consisting of nine measurements. The colours and line styles applied to the frequency responses are also shown.

Measurement #	Pressure (Pa)	Colour	Style	Cycle part
1	0	black	solid	1
2	$+P$	green	solid	
3	0	cyan	solid	
4	$-P$	red	solid	
5	0	magenta	solid	
6	$+P$	green	dashed	2
7	0	cyan	dashed	
8	$-P$	red	dashed	
9	0	magenta	dashed	

Generally, the magnitude differences between the unpressurized responses within any given pressure cycle in gerbil D are within 1 dB over the frequency range from 1.8 to 5 kHz. Below 0.35 kHz, magnitude differences are larger because the responses are affected by low-frequency noise. From 0.45 to 1.8 kHz, we observe that features due to the pars flaccida shift by as much as ±50 Hz within each pressure cycle. Above 5 kHz, magnitude differences are usually within 2 dB.

We observe under the microscope that static pressures result in a dome-like geometry of the pars flaccida, convex outward or inward for middle-ear positive and negative pressures, respectively. In previous studies involving measurements with an experimentally stiffened pars flaccida (Teoh et al. 1997; Rosowski & Lee 2002) it was concluded that the pars flaccida cannot play its normal role of shunting low-frequency sound around the rest of the eardrum. Consequently, the pressurized responses in our study look like those of a stiffness-dominated system. Moreover, the pars-flaccida features observed in the unpressurized response do not appear in the pressurized responses.

The positive-pressure responses are characterized by gently increasing magnitudes over the low and mid-frequency ranges. We observe over this frequency range that the magnitudes of vibration decrease as pressures are increased. At frequencies greater than 4 kHz, responses at +250 Pa increase gradually to a peak and responses at higher pressures rise sharply to a peak. Each pressurized response becomes higher than the unpressurized responses during this rise. As pressures increase, we observe an increase in both the magnitude and the frequency of the peak. At +250 Pa and +500 Pa, the peak of each response is followed by a drop with a number of irregularities. At higher pressures, the irregularities occur prior to the peak.

Figure 5.4: Effect of static pressurization on manubrium vibrations in Gerbil D with pressures of ±250 Pa.

Figure 5.5: Effect of static pressurization on manubrium vibrations in Gerbil D with pressures of ±500 Pa.

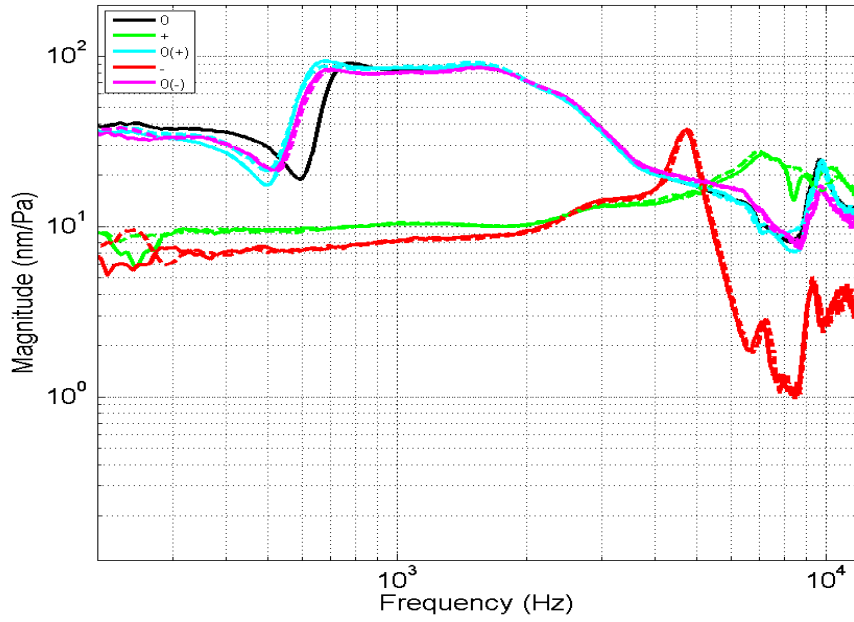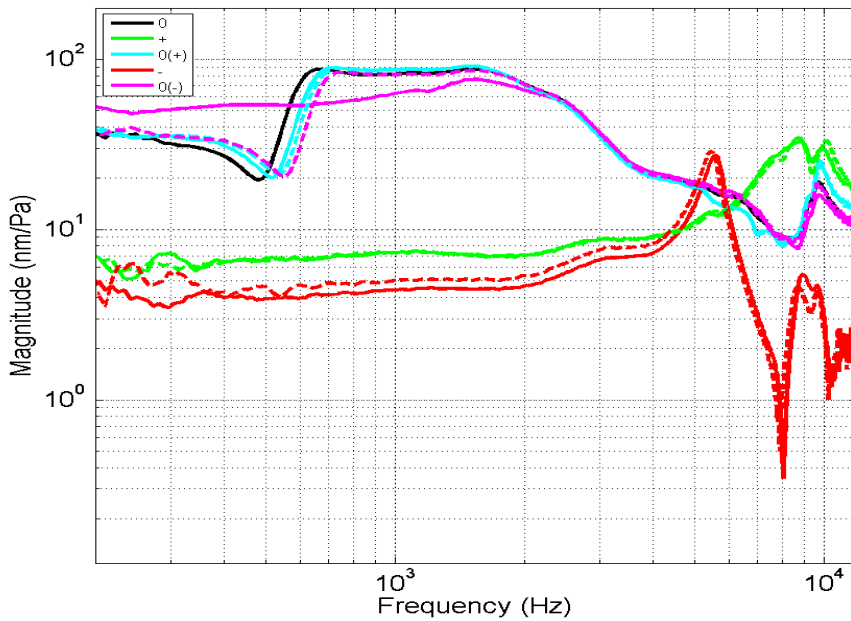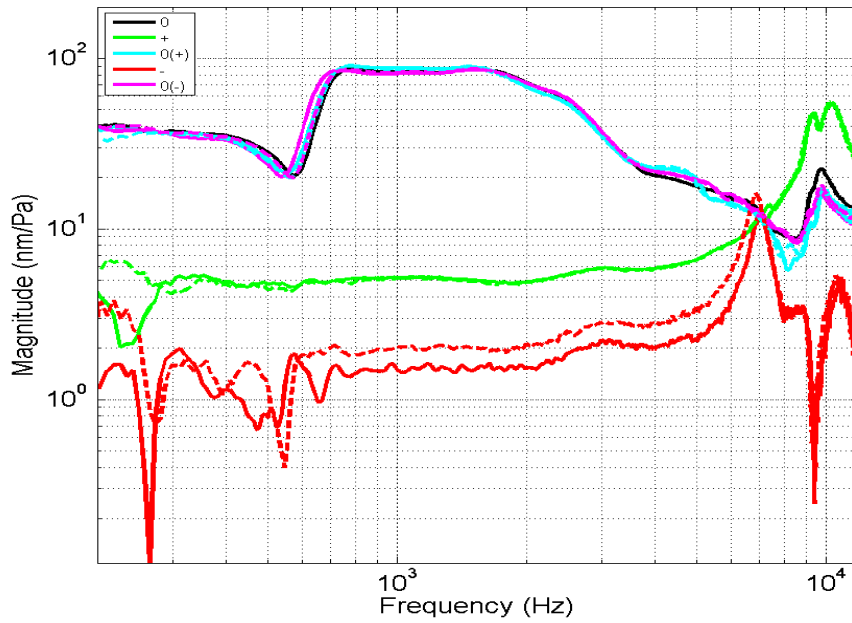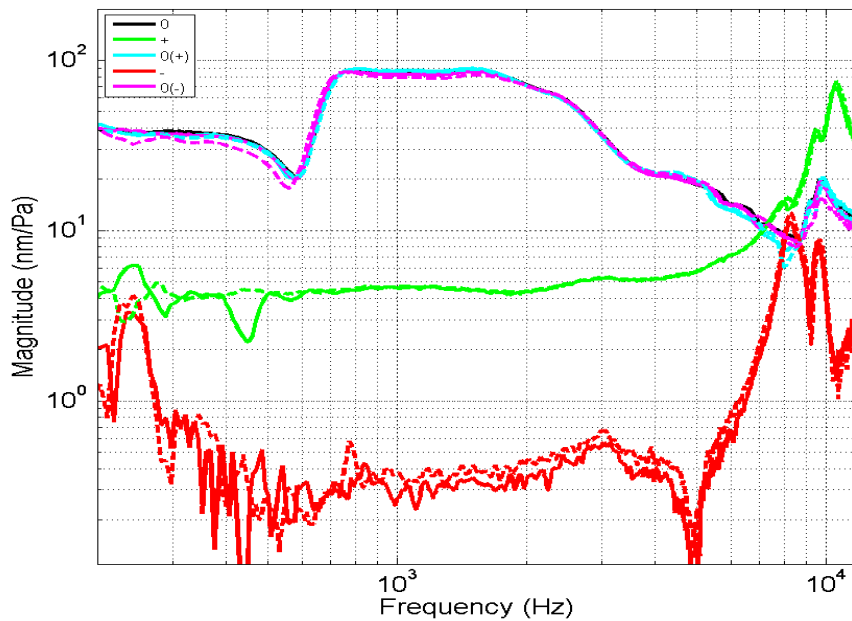*Figure 5.6: Effect of static pressurization on manubrium vibrations in Gerbil D with pressures of ±1000 Pa.*

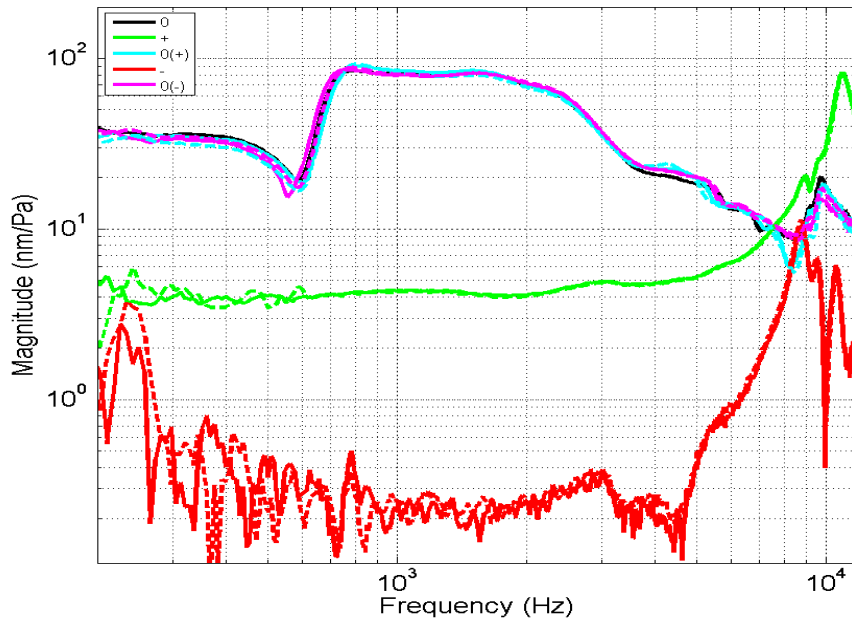*Figure 5.7: Effect of static pressurization on manubrium vibrations in Gerbil D with pressures of ±1500 Pa.*

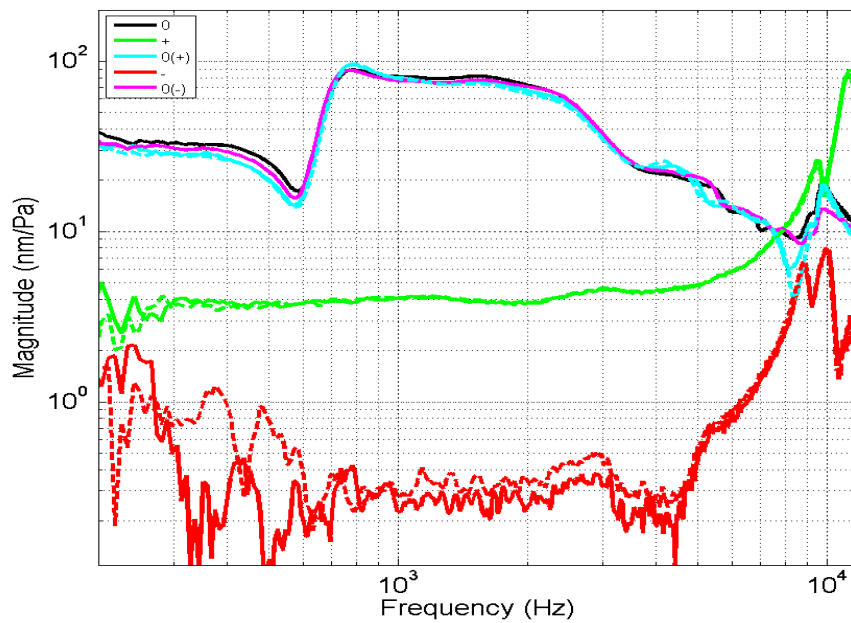*Figure 5.8: Effect of static pressurization on manubrium vibrations in Gerbil D with pressures of ±2000 Pa.*

Figure 5.9: Effect of static pressurization on manubrium vibrations in Gerbil D with pressures of ±2500 Pa.

As with the positive-pressure responses, the magnitudes of vibration of the negative-pressure responses over the low and mid frequency ranges are lower than those of the unpressurized responses. Ignoring low-frequency noise, responses in this frequency range follow the general trend of gently increasing magnitudes, except at pressures beyond −1000 Pa where a magnitude decrease is observed near 3.5 kHz. As with positive-pressure responses, the magnitudes of the negative-pressure responses decrease as pressures are increased. At frequencies greater than 3 kHz each response rises sharply to a peak. Only below −1000 Pa do the pressurized magnitudes surpass the unpressurized magnitudes. The frequency of the peak is lower than for the corresponding positive-pressure peak. As pressures are increased, the frequency of the peak increases while its magnitude decreases. The peak of each response is followed by a drop with a number of irregularities. Some irregularities are also observed prior to the peak. For example, responses at −1500 Pa, −2000 Pa and −2500 Pa show a sharp minimum around 5 kHz, and the response at −2500 Pa shows a peak and trough at 8.8 and 9.2 kHz, respectively, prior to the peak at 10 kHz.

Negative pressures decrease the response magnitudes more than positive pressures do, except for certain frequencies at lower pressures where a peak in the negative-pressure response rises above the positive-pressure response (2.7 to 5.2 kHz at 250 Pa, 4.5 to 6 kHz at 500 Pa, and 6.5 to 7.2 kHz at 1000 Pa). Generally, the magnitude differences between positive-pressure responses are within 1 dB for a given pressure (except at +250 Pa), and for negative-pressure responses they are within 2.5 dB for a given pressure. The exceptions are at the lowest frequencies, where differences are higher due to the effects of low-frequency noise.

After a positive pressure, the pars flaccida consistently returns to its normal flat state during the subsequent unpressurized measurement. Following a negative pressure, however, we observe under the microscope that the pars flaccida sometimes remains in the retracted state during the subsequent unpressurized measurement. This phenomenon is observed during

the −500 Pa cycle in gerbil D, as shown in Figure 5.5. Compared with a flat-pars-flaccida response, the unpressurized frequency response with a retracted pars flaccida is characterized by a gently increasing curve at low frequencies. We also observe in Figure 5.5 that the middle-ear resonance occurs at the same frequency for both pars-flaccida conditions and that the magnitude at resonance of the flat-pars-flaccida response is nearly 15% higher than for the retracted-pars-flaccida response. These findings are consistent with those of Maftoon et al. (2013).

As mentioned previously, the pressurized responses rise to a maximum magnitude at higher frequencies, and we observe a number of peaks and troughs. The magnitude of the highest peak, and therefore the maximum magnitude observed on the manubrium, is plotted for each pressure in Figure 5.10, along with its frequency in Figure 5.11. Linear magnitude scales are used in Figure 5.10. Since such a peak is not observed in the unpressurized responses, there is no data point at 0 Pa. The effects described previously are more clearly seen in Figures 5.10 and 5.11: as pressure increases, the maximum magnitude increases for the positive-pressure responses and decreases for the negative-pressure responses. Except at ±250 Pa, larger peak magnitudes are observed in the positive-pressure responses than in the corresponding negative-pressure responses. For both negative and positive static pressures, the frequency at which the maximum magnitude occurs increases as the absolute value of the pressure increases, increasing more slowly as the pressure increases. The frequencies of the maxima are consistently higher in the positive-pressure responses than in the corresponding negative-pressure ones. For both positive and negative pressure responses, the irregularities observed at higher frequencies are systematically compared with corresponding features on the pars tensa in Section 5.3.2.
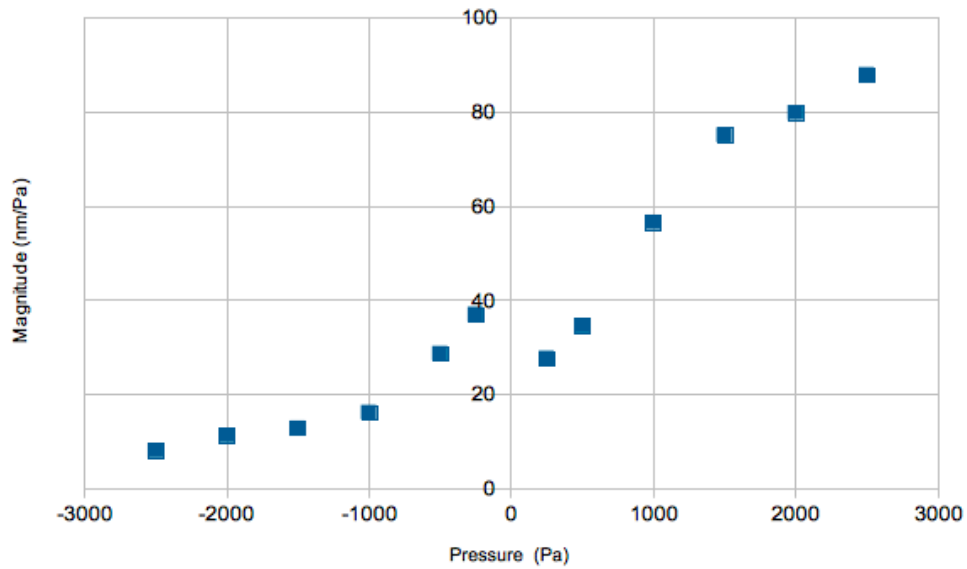
Figure 5.10: Magnitude maximum on the manubrium for each non-zero static pressure in Gerbil D. Magnitudes are shown on a linear scale.
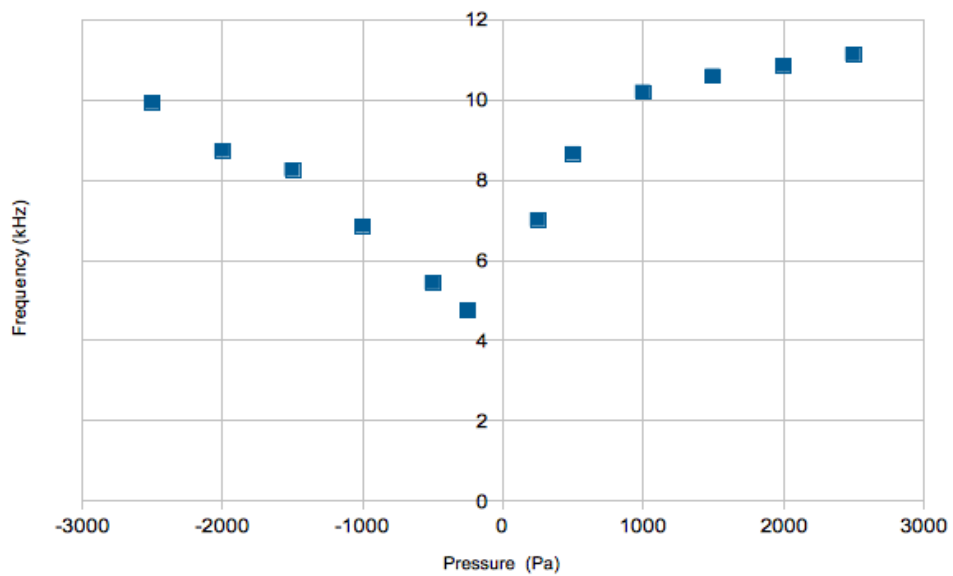

Figure 5.11: Frequency of the magnitude maximum for each pressure in Gerbil D. Frequencies are shown on a linear scale.

Figure 5.12 summarizes the low-frequency (1.5 kHz) results from all four gerbil manubria. This frequency is most suitable for analysis because the curves are relatively flat and relatively unaffected by noise. Lower frequencies are not suitable due to larger magnitude differences between measurements as a result of low-frequency noise. Unpressurized responses are omitted from this figure in order to permit an expanded magnitude scale. (At this frequency, unpressurized magnitudes are much larger than pressurized magnitudes.) Each magnitude value plotted in the figure is calculated as an average of the positive or negative pressurized values for a given pressure at 1.5 kHz. The general low-frequency trends described above for gerbil D are seen more clearly in Figure 5.12 and can be compared with the other gerbils. We observe that magnitudes decrease as the pressure applied to the middle ear increases. The magnitudes drop rapidly up to ±1000 Pa and then more slowly as the applied pressure increases. For the most negative pressures, magnitude reductions are much greater than for the positive pressures. Especially for positive pressures, the inter-animal variability is relatively small. For negative pressures we observe that the magnitudes for gerbil D are considerably lower than those for the other gerbils. As discussed later, unusually large magnitudes are observed at +2000 Pa and +2500 Pa in gerbil B.
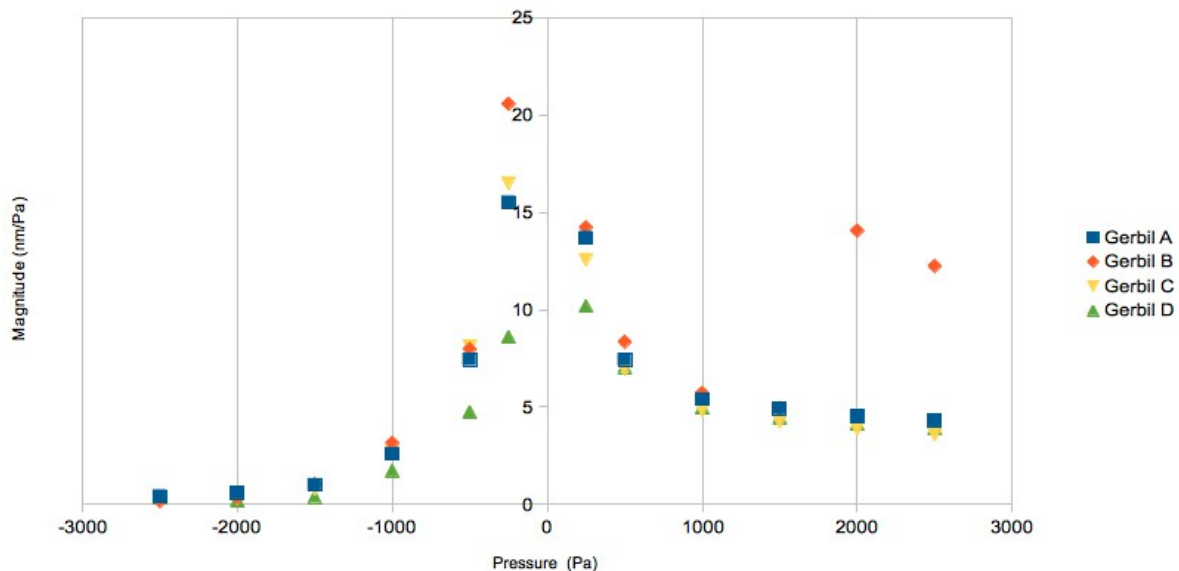
Figure 5.12: Vibration magnitudes of pressurized responses from all four gerbil ears measured on the manubrium at a frequency of 1.5 kHz.

Figure 5.13 displays how the unpressurized responses on the manubrium in gerbils A to D evolve over the duration of the experiment. In each panel the figure shows unpressurized frequency responses from the beginnings of pressure cycles, at approximately 20–25 min intervals. The black curve in each panel corresponds to the first recorded measurement. It is followed by red, green, blue, cyan and magenta curves that represent subsequent recordings in chronological order. The observed differences among the frequency responses within each gerbil are generally within 3 dB, except where an abrupt feature is shifting. The frequency shifts are particularly obvious at the pars-flaccida-induced peak, which shifts at an average rate of 1.7 to 3.7 Hz/min between the black and magenta curves in each gerbil. Maftoon et al. (2013) reported a maximum shift of about 2 Hz/min in their *in vivo* gerbil experiments.
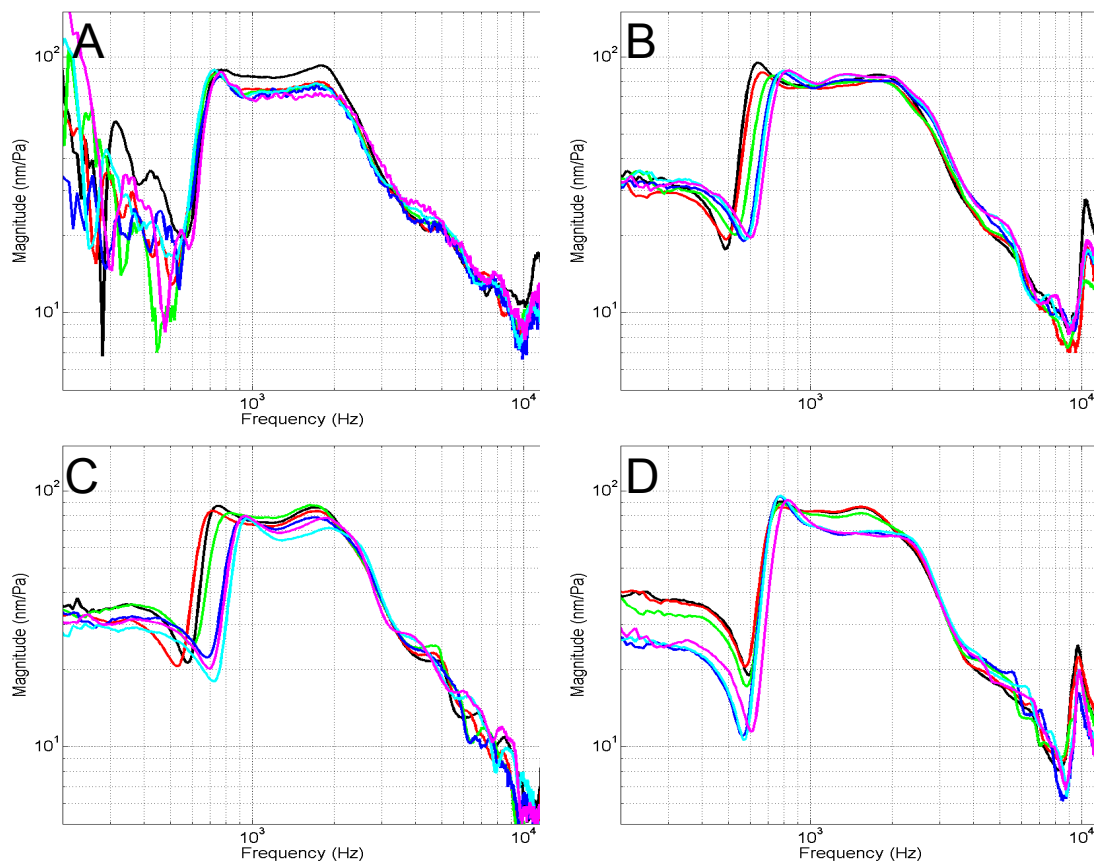
Figure 5.13: Unpressurized measurements on the manubrium of gerbils A to D recorded over the course of the experiment. The colour sequence of black, red, green, blue, cyan and magenta correspond to responses recorded in increasing chronological order.

5.3.2 Pars-tensa responses

We present in this section the effects of static pressurization on the vibration displacement response of the pars tensa for protocol 1. As on the manubrium, similar trends are observed on the pars tensa for all four gerbils, so detailed results are presented here only for gerbil D, in Figures 5.14 to 5.19, in the same format as for Figures 5.4 to 5.9.

In each figure, the magnitude differences between unpressurized responses with the same pars-flaccida condition are generally within 1.5 dB. The exceptions are at the pars-flaccida features and the sharp high-frequency features, where differences are within 4 dB and 8 dB, respectively. Features due to the pars flaccida shift by as much as ±40 Hz within each pressure cycle. As on the manubrium, a flat pars flaccida is consistently observed during each unpressurized response that immediately follows a positive pressure. On the other hand, a retracted pars flaccida is observed in each pressure cycle for one or both of the unpressurized measurements immediately following a negative pressure. This phenomenon may be related to the time course of protocol 1, given that pars-tensa responses were recorded after all the pressure cycles were completed on the manubrium.

As on the manubrium, pressurized pars-tensa responses over the low and mid frequency ranges are characterized by gently increasing curves, reduced magnitudes of vibration, and absence of the effects due to the pars flaccida. Unlike the situation on the manubrium, positive pressures reduce magnitudes more than the corresponding negative pressures do over this frequency range. As pressure increases, magnitudes decrease more slowly, and the negative and positive pressure responses become more similar. At higher frequencies, the responses rise sharply to a series of peaks and troughs. The frequencies of these features increase with pressure. This is shown more clearly in Figure 5.20, which illustrates the pressurized responses over the reduced frequency range of 2 to 11 kHz. Compared with those on the manubrium, the sharp features on the pars tensa are characterized by much larger magnitudes. Generally, the observed magnitude differences between pressurized responses

Figure 5.14: Effect of static pressurization on pars-tensa vibrations in Gerbil D with pressures of ±250 Pa.

Figure 5.15: Effect of static pressurization on pars-tensa vibrations in Gerbil D with pressures of ±500 Pa.

Figure 5.16: Effect of static pressurization on pars-tensa vibrations in Gerbil D with pressures of ±1000 Pa.

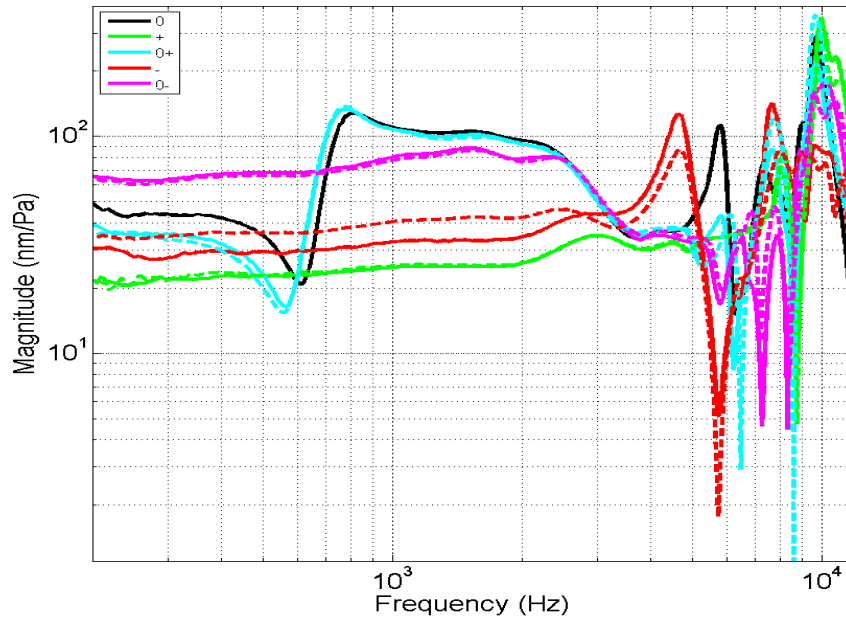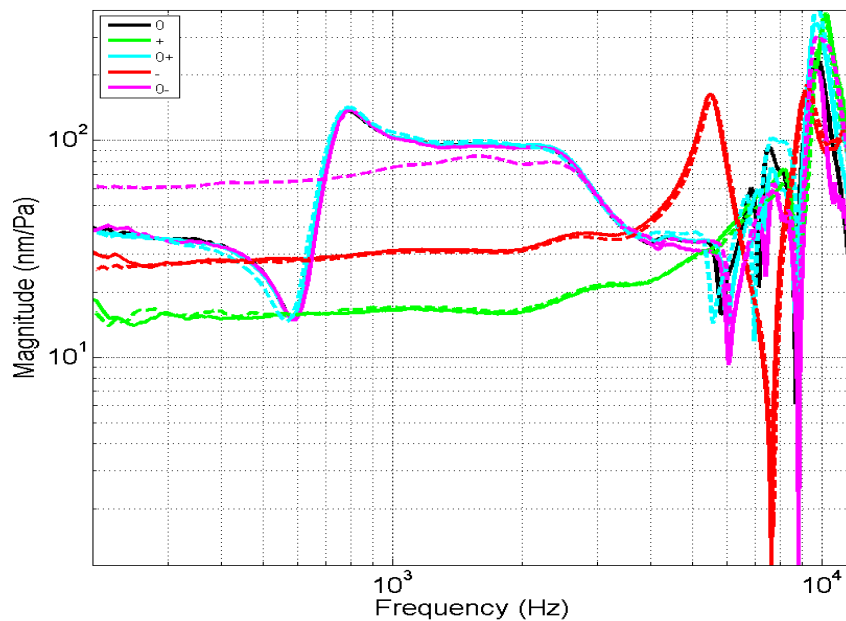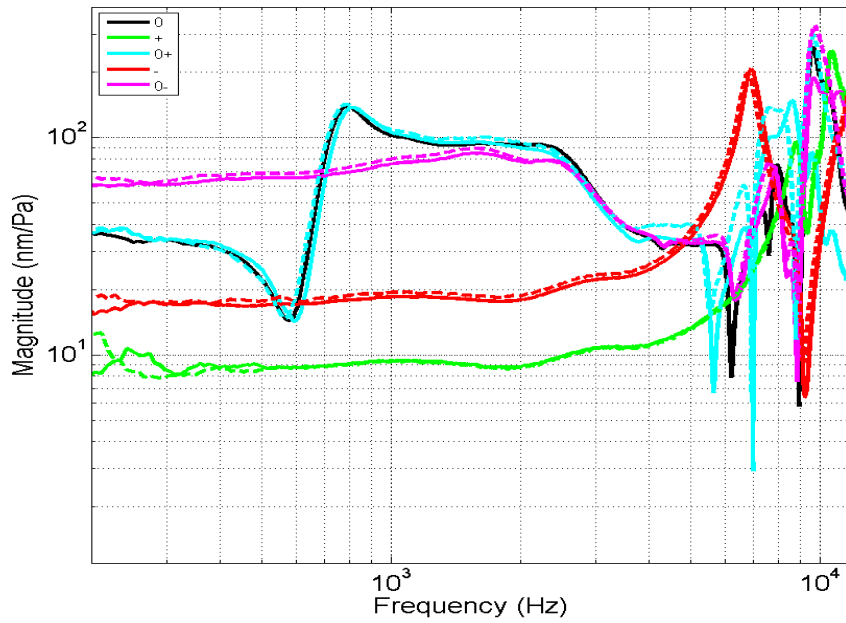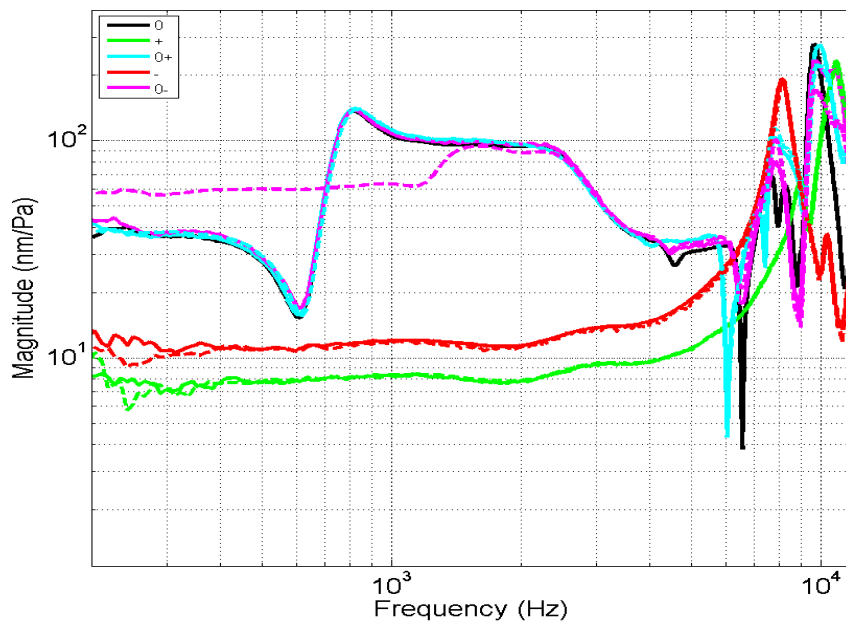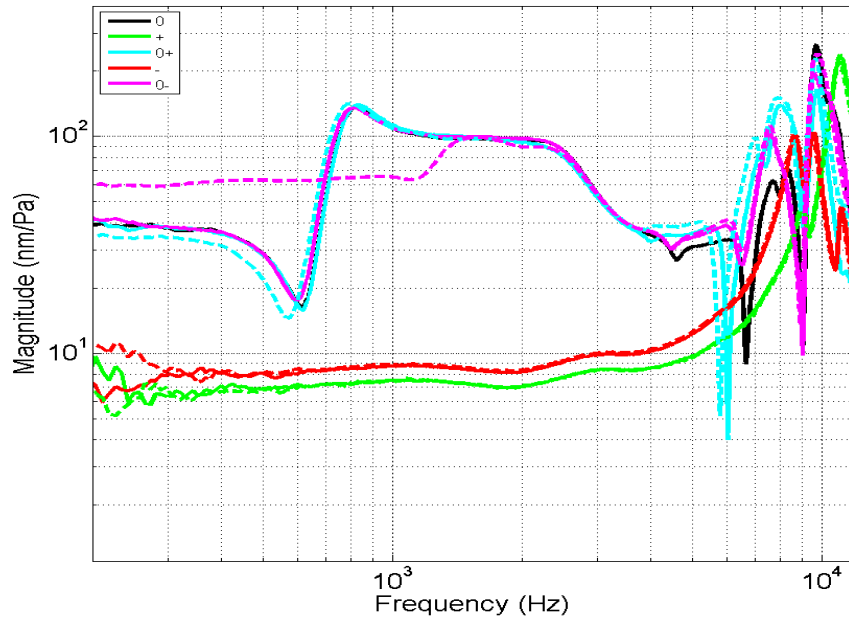*Figure 5.17: Effect of static pressurization on pars-tensa vibrations in Gerbil D with pressures of ±1500 Pa.*

*Figure 5.18: Effect of static pressurization on pars-tensa vibrations in
Gerbil D with pressures of ±2000 Pa.*
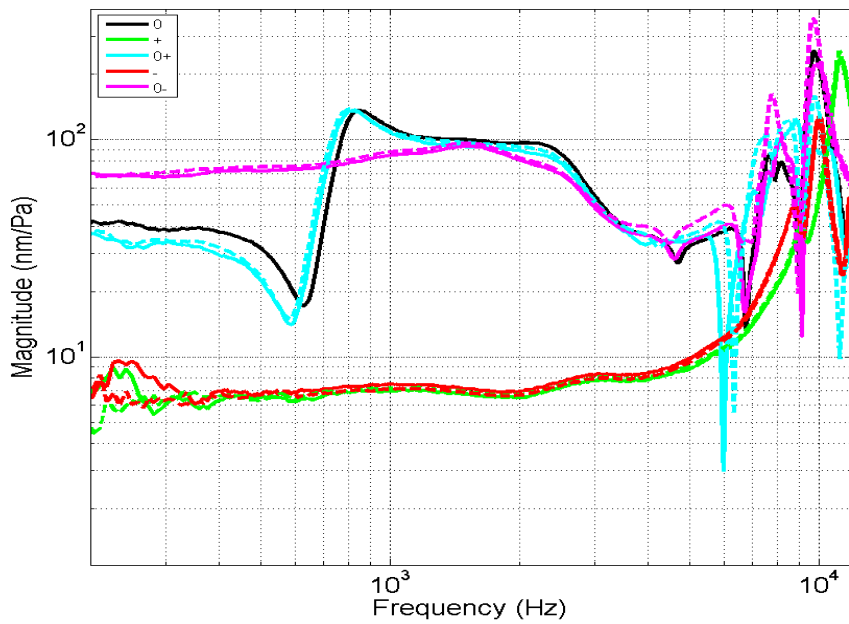
*Figure 5.19: Effect of static pressurization on pars-tensa vibrations in
Gerbil D with pressures of ±2500 Pa.*

on the pars tensa are within 1 dB for a given pressure, increasing to 2 dB at the sharpest features. The exception is at −250 Pa, where larger differences are observed.

To facilitate comparison between manubrium and pars-tensa responses, the arrows in Figure 5.20 correspond to the frequencies at which sharp features are observed in the pressurized responses of the manubrium. Arrows directed upwards correspond to peaks and arrows directed downwards correspond to troughs. Green arrows correspond to features in the positive-pressure responses of the manubrium and red arrows correspond to features in the negative-pressure responses. Except at ±250 Pa, we observe that the features in the positive and negative pressure pars-tensa responses also appear in the corresponding manubrium responses with a maximum difference of less than 0.5 kHz. As mentioned earlier, the features are pushed to higher frequencies as the pressure increases. For the negative-pressure responses, the first peak is shifted from 4.7 kHz at −250 Pa to 8.9 kHz at −2500 Pa. For the positive-pressure responses, the first peak is shifted from 8 kHz at 250 Pa to 9.1 kHz at 2500 Pa.

In the negative-pressure responses, we observe a splitting of a single peak (6.8 kHz at −1000 Pa) into two peaks (8 kHz and 10.1 kHz at −1500 Pa). Although the second peak only becomes well-defined in the −1500 Pa responses, we observe a small shoulder at approximately 8 kHz at −500 Pa, and a more obvious shoulder at approximately 8.8 kHz at −1000 Pa. These shoulders are presumably forerunners of the second peak. As the pressure increases further, the magnitude of the first peak decreases while the magnitude of the second peak increases: at −1500 Pa the magnitude of the first peak is 10 times larger than that of the second, while at −2500 Pa it is 5 times smaller. We also observe that, in the positive-pressure responses, the magnitude of the first peak decreases for pressures beyond +1000 Pa. A suggested hypothesis for this phenomenon is discussed in Section 5.5. Similar phenomena are also observed in gerbils A and C: except at very low pressures, features in the pressurized responses on the manubrium also appear in the pars-tensa responses with a maximum difference of less than 1 kHz. As discussed later, some pars-tensa responses in
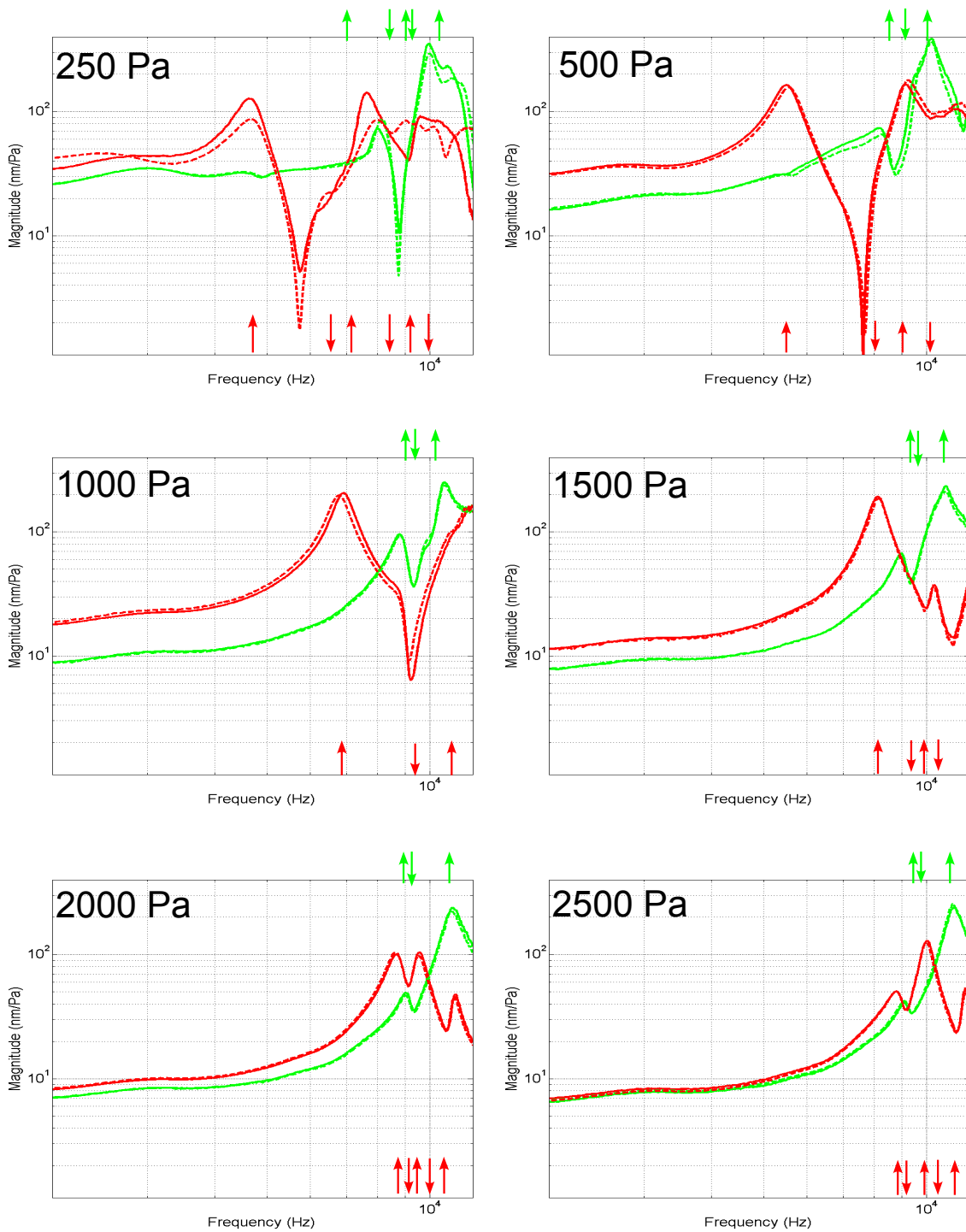
Figure 5.20: Pressurized responses on the pars tensa of gerbil D, with an expanded frequency scale. Arrows directed upward and downward correspond to frequencies of peaks and troughs, respectively, in the pressurized manubrium responses.

gerbil B are anomalous, resulting in features in the manubrium responses that do not appear in the pars-tensa responses, and vice versa.

Figure 5.21 summarizes the results from the pars tensa for all four gerbils in the same format as Figure 5.12. As with the manubrium, the magnitudes drop rapidly up to ±1000 Pa and then more slowly as the applied pressure increases. Generally, the trend of positive pressures reducing magnitudes more than negative pressures is observed at lower pressures, and essentially disappears at higher pressures. This trend does not apply to gerbil B. Abnormally large magnitude values are observed in the positive-pressure responses of gerbil B: magnitudes at +250 Pa and +500 Pa are beyond the upper magnitude limit of the figure and are marked with arrows. As mentioned in Section 5.3.1, a similar anomaly is observed on the manubrium of gerbil B, and we suggest a hypothesis in Section 5.5.
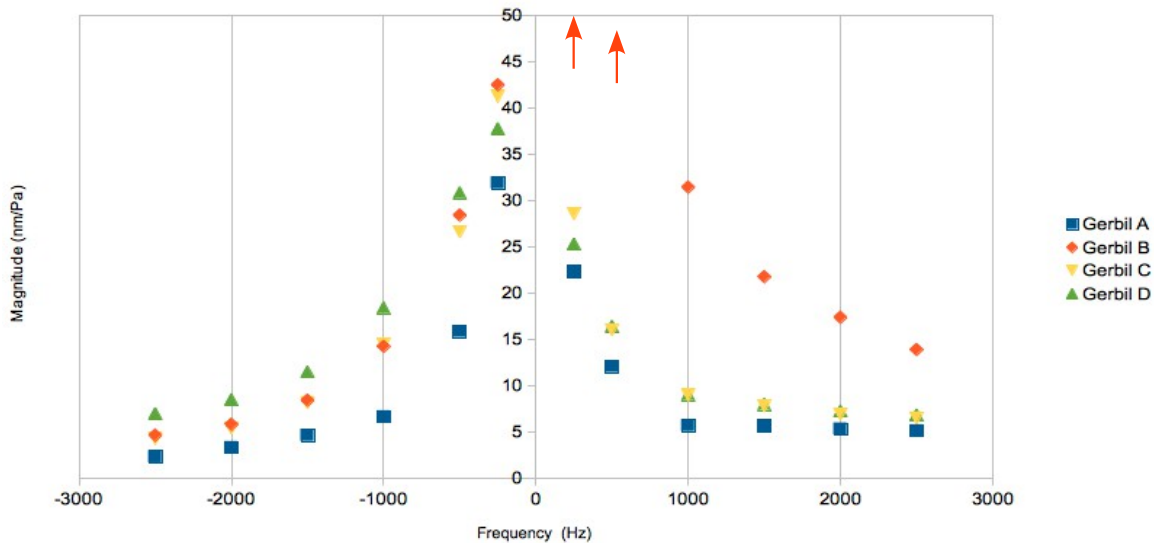
Figure 5.21: Vibration amplitudes of pressurized responses from all four gerbil ears measured on the pars tensa at a frequency of 1.5 kHz. Amplitudes of gerbil B at 250 Pa and 500 Pa (arrows) are 401 nm/Pa and 323 nm/Pa respectively.

As we did for the manubrium (cf. Figure 5.13), in Figure 5.22 we display how the unpressurized responses for the pars tensa of gerbils A to D evolve over the duration of the experiment. In order to improve the visibility of the features at higher frequencies, only three responses are plotted in each panel. The black curve corresponds to the first recorded

measurement, while the green and red curves correspond to measurements recorded near the middle and end of the experiment, respectively, each at the beginning of a pressure cycle. Typical responses are observed in gerbils A, C and D. At the pars-flaccida peak, we observe frequency shifts ranging from 1.9 to 3.1 Hz/min between the black and green curves in gerbils A, C and D. Compared with Figure 5.13 for the manubrium, the differences observed among the frequency responses within each gerbil are much greater, particularly above breakup due to sharp features with relatively large magnitude differences and sometimes substantial frequency shifts. Generally, however, we observe in each gerbil that the high-frequency irregularities of each response are within 1 kHz of each other. The responses recorded in gerbil B are characterized by abnormally large amplitudes. In addition, anomalous features are observed in the second and third recorded responses in gerbil B at approximately 4 kHz, marked by high-magnitude peaks.
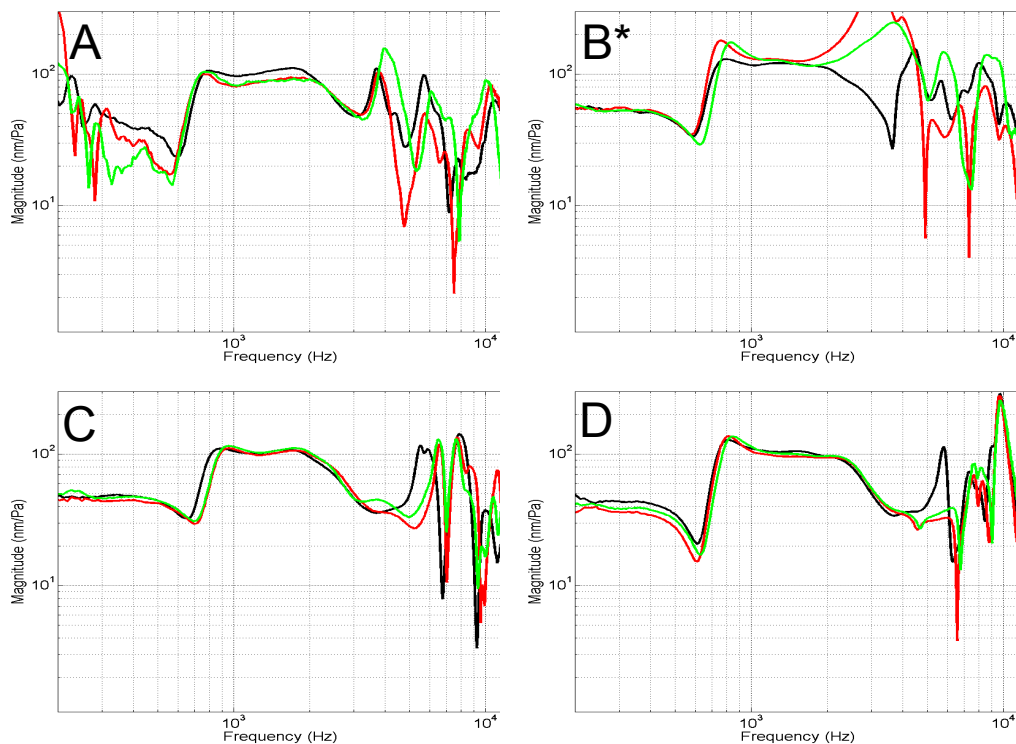
Figure 5.22: Unpressurized measurements on the pars tensa of gerbils A to D recorded over the course of the experiment. Black, red and green correspond to measurements recorded at the beginning, middle and end of the experiment, respectively, each at the beginning of a pressure cycle. Some anomalous responses are observed in gerbil B and so it is marked with an asterisk.

Figure 5.23 provides an overview of the results for gerbil D by showing the magnitudes at 1.5 kHz as a function of time over the course of experiment. The magnitudes are plotted on a logarithmic scale, with manubrium and pars tensa magnitudes shown in panels A and B, respectively. Black, green and red markers correspond to unpressurized magnitudes, positive-pressure magnitudes and negative-pressure magnitudes, respectively. The nine measurements of each pressure cycle are demarcated by a horizontal brace at the top of each panel. In panel A we observe a slight drift downward of the unpressurized measurements on the manubrium with time, while for the pars tensa in panel B the unpressurized measurements remain at approximately the same magnitude throughout the experiment. We suggest that this may be due to dehydration that occurred during the measurements on the manubrium but had stabilized by the time of the pars-tensa measurements.

As mentioned previously, for both the manubrium and pars tensa the pressurized magnitudes generally decrease with an increase in pressure, with nearly zero change at the highest pressures. On the manubrium, positive and negative pressure responses are similar at low pressures . The positive-pressure responses reach a constant level by about +1000 Pa while the negative-pressure responses drop more rapidly and only reach a constant level after −1500 Pa. In each cycle on the manubrium, the two positive-pressure magnitudes are nearly the same, while at 500 Pa, 1000 Pa and 1500 Pa the first negative-pressure magnitude is somewhat lower (4 dB) than the second.

On the pars tensa, the negative-pressure responses are about 7 dB higher than the positive-pressure ones until 1000 Pa; the differences decrease to nearly zero at the highest pressures. In each cycle on the pars tensa the two positive-pressure magnitudes are nearly the same, and only at 250 Pa are the negative-pressure magnitudes different, with the difference being in the same direction as observed on the manubrium at a few pressures.
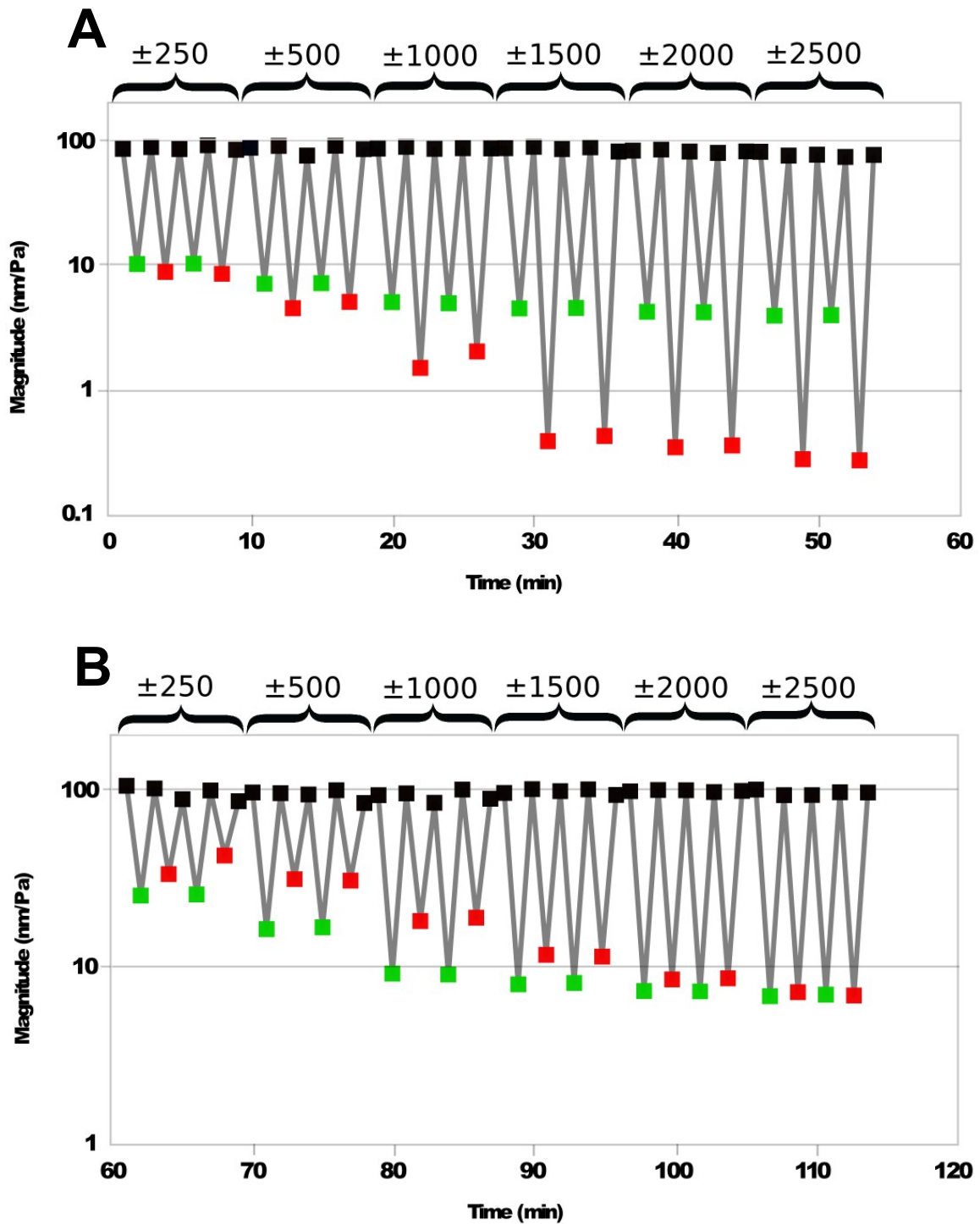
Figure 5.23: Magnitudes at 1.5 kHz in gerbil D as a function of time over the course of the experiment. Black, green and red markers correspond to unpressurized, positive-pressure and negative-pressure responses, respectively. Measurements in each cycle are demarcated by a horizontal brace. (A) Manubrium magnitudes. (B) Pars-tensa magnitudes.

5.4 Pressurization protocol 2

5.4.1 Introduction

We present in this section the effects of static pressurization on the vibration displacement magnitude response of the gerbil manubrium and pars tensa over multiple cycles of protocol 2. Recall that measurements were made only on the manubrium in gerbil E and only on the pars tensa in gerbils F, G and H. The frequency responses recorded in gerbils E (manubrium) and H (pars tensa) are presented in Sections 5.4.2 and 5.4.3, respectively. In those sections we also show the presence of hysteresis in the pressure-magnitude plots within pressure cycles. Responses recorded in gerbils F and G are presented in Section 5.4.4, with emphasis on the anomalous responses observed.

5.4.2 Manubrium responses

The frequency responses recorded during the positive-pressure sweep of cycle 1 in gerbil E are presented in Figure 5.24. The sequence of measurements performed during each pressure sweep is described in Section 4.9.3. The line colours red, green, blue, cyan, magenta and yellow correspond to frequency responses recorded at pressures of +250 Pa, +500 Pa, +1000 Pa, +1500 Pa, +2000 Pa and +2500 Pa, respectively. Unpressurized responses are given by black curves. Solid lines correspond to responses recorded during the loading part of the pressure sweep and dashed lines correspond to responses recorded during the unloading part. Over the low-to-mid frequency range (up to approximately 3 kHz), positive-pressure responses are characterized by gradually increasing magnitudes, and no pars-flaccida features are observed. Their magnitudes decrease as the pressure increases, and the responses recorded during the unloading part of the positive-pressure sweep for a given pressure are greater in magnitude than the responses recorded at the same pressure during the loading part. The maximum difference between responses (about 6 dB) occurs at +250 Pa and decreases to nearly zero at high pressures. We observe small humps

on the frequency response curves at approximately 1.3 kHz; the humps are more marked at higher pressures. Beyond 2 kHz, the +250 Pa loading and unloading responses as well as the +500 Pa unloading response increase gently to a peak, and the other responses rise sharply to a peak. The frequency of each peak is given in Table 5.3. As pressure increases, the peaks are shifted to higher frequencies. For pressures of +250 and +500 Pa, each peak occurs at a lower frequency during the unloading part than during the loading part. Beyond +500 Pa, the loading and unloading peaks for a given pressure occur at approximately the same frequency. The peak of each response is followed by a drop with a number of irregularities. Some irregularities are also observed prior to the peak at pressures of +1500 Pa, +2000 Pa and +2500 Pa.

Table 5.3: Frequency of the highest peak in the loading and unloading curves of each positive-pressure response.

Pressure (Pa)	Loading response (kHz)	Unloading response (kHz)
+250	5.4	2.7
+500	8.2	7.2
+1,000	9.3	
+1,500	10.1	
+2,000	10.3	
+2,500	10.4	

Frequency responses recorded during the negative-pressure sweep of cycle 1 in gerbil E are presented in Figure 5.25. Red, green, blue, cyan, magenta and yellow correspond to responses recorded at −250 Pa, −500 Pa, −1000 Pa, −1500 Pa, −2000 Pa, −2500 Pa, respectively. Line styles are in the same format as for Figure 5.24. As with the positive-pressure responses, the negative-pressure responses are characterized by gently increasing magnitudes over the low-to-mid frequency range, no pars-flaccida features are observed, and generally the magnitudes of vibration decrease as the pressure increases. Over this frequency range, responses recorded during the loading part of the sweep for a given
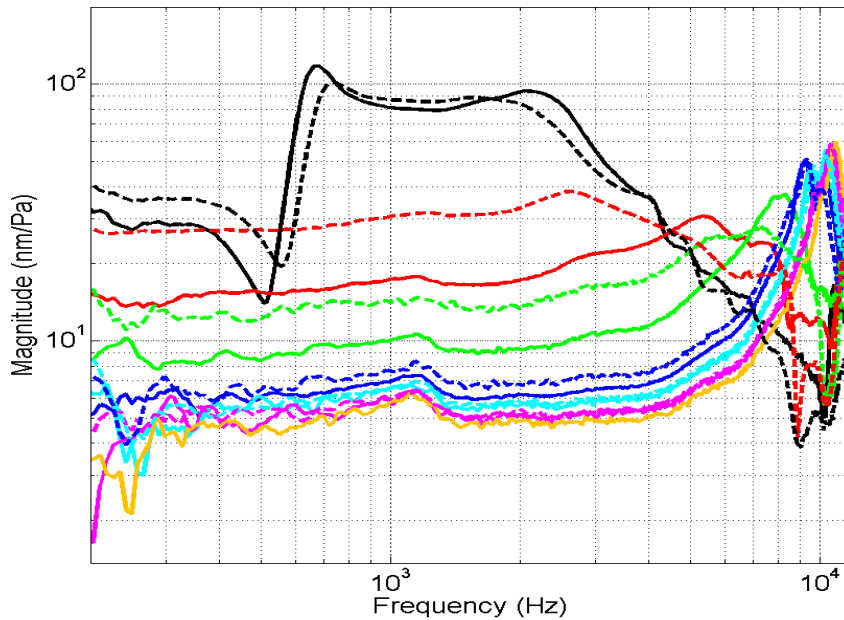
Figure 5.24: Effect of static pressurization during the positive-pressure sweep of cycle 1 on the manubrium in gerbil E. Red, green, blue, cyan, magenta and yellow correspond to frequency responses recorded at pressures of +250 Pa, +500 Pa, +1000 Pa, +1500 Pa, +2000 Pa and +2500 Pa, respectively. Unpressurized responses are given by black curves. Solid lines correspond to responses recorded during the loading part of the pressure sweep and dashed lines correspond to responses recorded during the unloading part.

pressure are greater in magnitude than responses recorded during the unloading part. The magnitude differences between the loading and unloading responses are between 2 dB and 6 dB: they are very small at −250 Pa, increase with pressure, and then become very small again at −2000 and −2500 Pa. We observe the presence of two humps, at 1400 Hz and at 2300 Hz, instead of the one hump in the positive-pressure responses of Figure 5.24. At higher frequencies, the −250 Pa loading and unloading responses increase gently to a peak, and higher-pressure responses rise sharply to a peak. The frequency of each peak is given in Table 5.4. The peaks are shifted to higher frequencies as the pressure increases. The magnitudes of the peaks decrease up to −1500 Pa, then increase. For −250 Pa, the peak occurs at a lower frequency during the unloading part than during the loading part. At higher pressures, the loading and unloading peaks occur at approximately the same

frequency. As with the positive-pressure responses, the peak of each response is followed by a drop with a number of irregularities. At the highest pressures (−2000 Pa and −2500 Pa), small irregularities are observed prior to the peak.

Table 5.4: Frequency of the highest peak in the loading and unloading curves of each negative-pressure response.

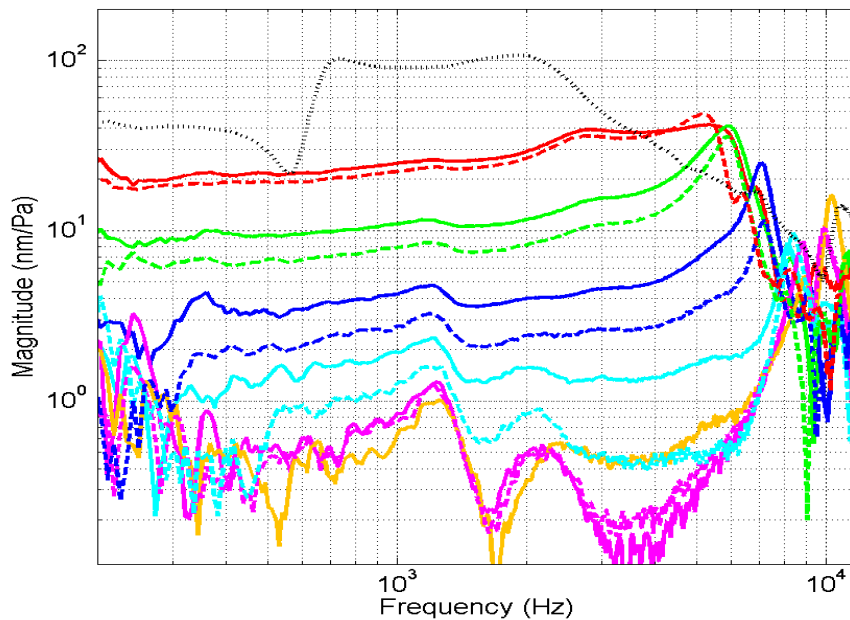| Pressure (Pa)	Loading response (kKz)	Unloading response (kHz)
−250	5.8	5.2
−500	5.9	
−1000	7.0	
−1500	8.2	
−2000	9.9	
−2500	10.2	

Figure 5.25: Effect of static pressurization during the negative-pressure sweep of cycle 1 on the manubrium in gerbil E. Red, green, blue, cyan, magenta and yellow correspond to frequency responses recorded at pressures of −250 Pa, −500 Pa, −1000 Pa, −1500 Pa, −2000 Pa and −2500 Pa, respectively. Line styles are the same as for Figure 5.24.

The mid-frequency magnitude differences between responses recorded during the loading and unloading parts of a pressure sweep are more clearly seen in Figure 5.26. This figure summarizes the results from all three pressure cycles in gerbil E at 2 kHz in a format similar to that of Figure 5.11. The arrows indicate the progression of each cycle. (We do not select 1.5 kHz as we did for Figure 5.11 because of the humps observed in the range of 1.3–2.3 kHz in the pressurized responses.) In each cycle, positive-pressure magnitudes are greater during the unloading part, and negative-pressure magnitudes are greater during the loading part for a given pressure. We also see that magnitudes are considerably larger on the positive-pressure side than on the negative-pressure side. The curves for all three cycles are superimposed in panel D, with red, green and blue corresponding to cycles 1,2 and 3, respectively. We observe that all three cycles are very similar, with the exception of a single magnitude point at −2500 Pa of the first cycle, and that the loading/unloading differences become somewhat smaller from cycle to cycle.

Figure 5.27 displays how the unpressurized frequency responses for the manubrium of gerbil E evolve during the experiment. The responses plotted were recorded at 20–30 min intervals, at the start of each pressure cycle and with a final measurement at the end of the experiment. The colour sequence of black, red, green, blue and cyan corresponds to responses recorded in increasing chronological order. . The responses follow the same trends that were discussed for protocol 1 (Figure 5.13). The differences among the frequency responses are generally within 3 dB, except where an abrupt feature is shifting. At the peak due to the pars flaccida, for example, we observe frequency shifts to higher frequencies at an average rate of approximately 2 Hz/min between the black and blue curves.
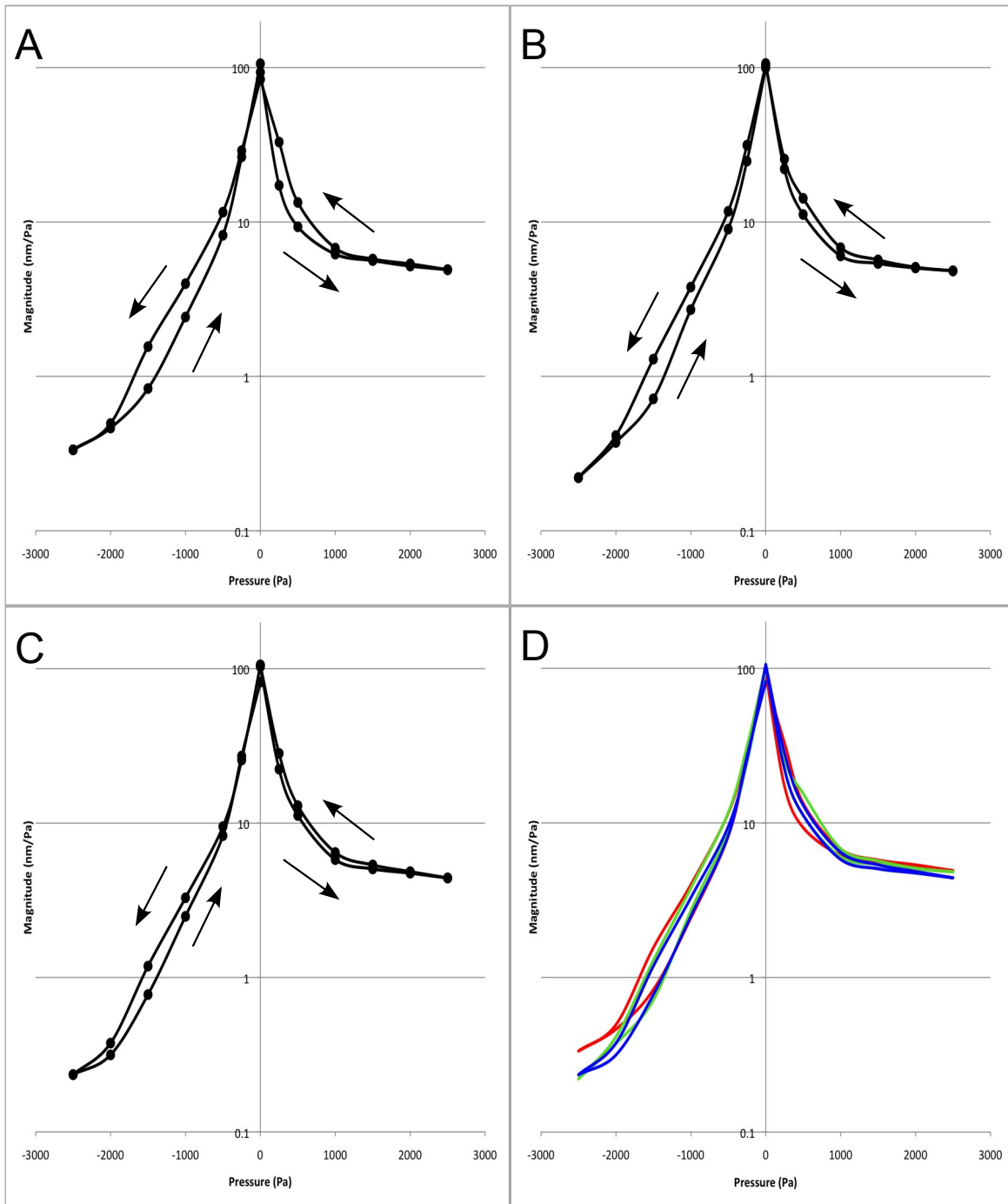
Figure 5.26: Magnitudes of vibration recorded on manubrium in gerbil E at a frequency of 2 kHz for cycles 1,2 and 3 are shown in panels A,B and C, respectively. The curves from each panel are superimposed in panel D with red, green and blue corresponding to the curves in panels A,B and C, respectively.
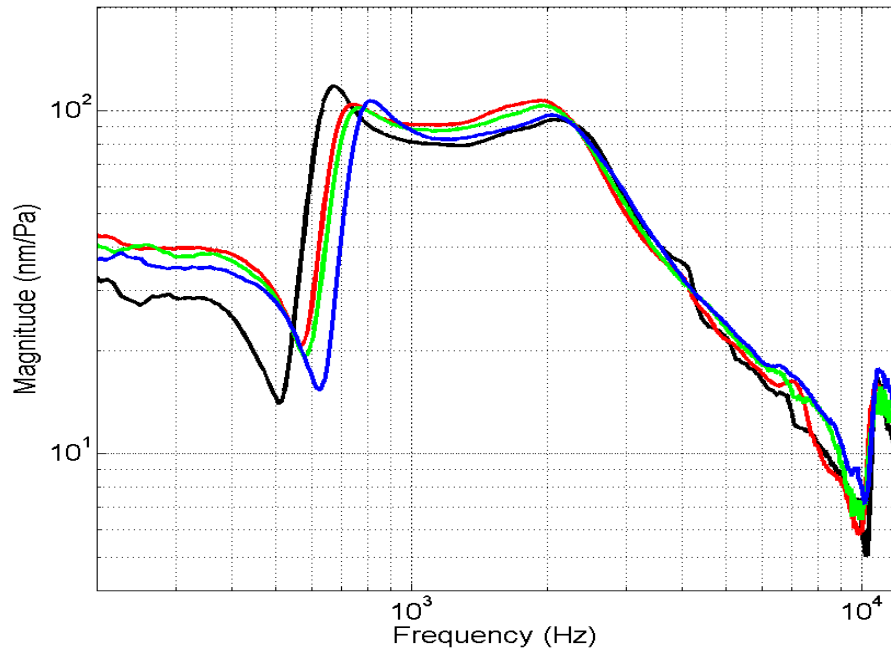
Figure 5.27: Unpressurized measurements on the manubrium of gerbil E recorded over the course of the experiment. The colour sequence of black, red, green and blue corresponds to measurements in increasing chronological order.

5.4.3 Pars-tensa responses

The frequency responses recorded on the pars tensa during the positive-pressure sweep of cycle 1 in gerbil H are presented in Figure 5.28, in the same format as for Figure 5.24. Like those for the manubrium of gerbil E, the positive-pressure responses on the pars tensa of gerbil H over the low-to-mid frequency range (up to approximately 3 kHz) are characterized by gradually increasing magnitudes and display no pars-flaccida features. The humps that were observed in the responses of gerbil E do not appear in gerbil H, nor do they appear in gerbils F and G; it is not clear why this is the case. Over the low-to-mid frequency range, the magnitudes of the responses of gerbil H decrease as pressure increases, and the responses recorded during the unloading part of the positive-pressure sweep for a given pressure are greater in magnitude than responses recorded during the loading part. Magnitude differences between loading and unloading responses for a given

pressure are largest at +250 Pa (about 13 dB), then decrease with an increase in pressure and become nearly zero for pressures of +1500 Pa or greater. Between 2.5 and 4 kHz, the response recorded at +250 Pa during the unloading part is characterized by a slight decrease before increasing sharply, and the responses at higher pressures begin to rise sharply. In order to improve visibility of the features at higher frequencies, the loading and unloading positive-pressure responses are shown with an expanded frequency scale (from 5 to 11 kHz) in Figure 5.30A and B, respectively. As on the manubrium, the responses show a number of peaks and troughs that are shifted to higher frequencies as pressure increases. The peak-to-trough magnitude swings are much larger than on the manubrium. In each figure, it is not clear which features correspond to which for responses at different pressures. For example, in Figure 5.30B, it is difficult to conclude which peak on the cyan curve (9.3 or 10.8 kHz) corresponds to the peak at 10.2 kHz on the blue curve.
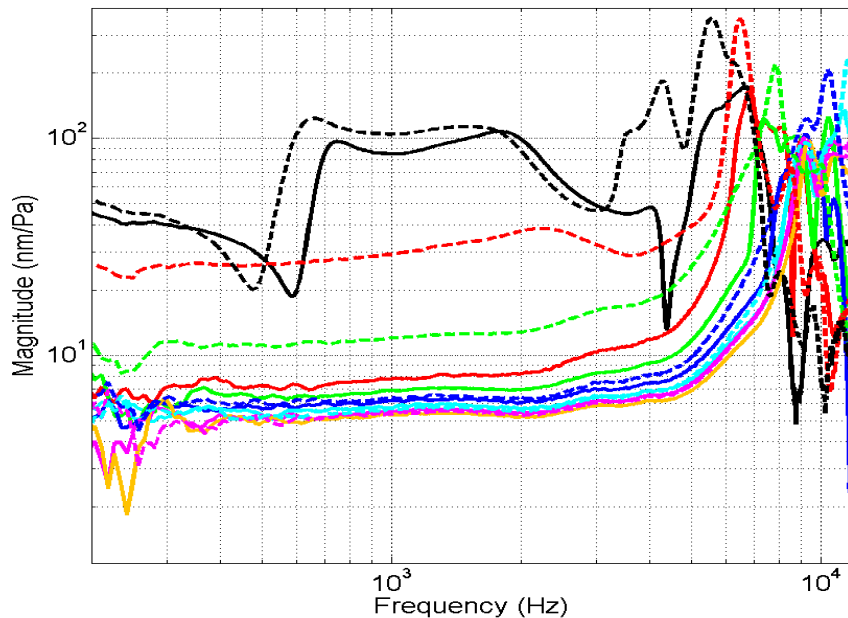
Figure 5.28: Effect of static pressurization during the positive-pressure sweep of cycle 1 on the pars tensa in gerbil H. Colours and line styles are the same as for Figure 5.24.

As shown in Figure 5.29, the low-to-mid-frequency negative-pressure responses, like the positive-pressure ones, are characterized by gently increasing magnitudes, show no pars-flaccida effect, and decrease in magnitude as the pressure increases. In this case the responses recorded during the loading part of the pressure sweep are generally greater in magnitude than responses recorded during the unloading part for a given pressure. These magnitude differences increase with pressure to about 2 dB at 1500 Pa before becoming smaller at higher pressures. At frequencies greater than 3 kHz, the response recorded at −250 Pa during the unloading part is characterized by a relatively flat response followed by an abrupt rise, and the other responses begin to rise sharply. Similar to the positive-pressure responses on the pars tensa, the negative-pressure responses show a number of peaks and troughs that are shifted to higher frequencies as the pressure increases, and the peak-to-trough magnitude swings are much larger than on the manubrium. As with the positive-pressure responses, even with the expanded frequency scale in Figure 5.30 it is not clear which features correspond to which at different pressures. For example, in Figure 5.30D, it
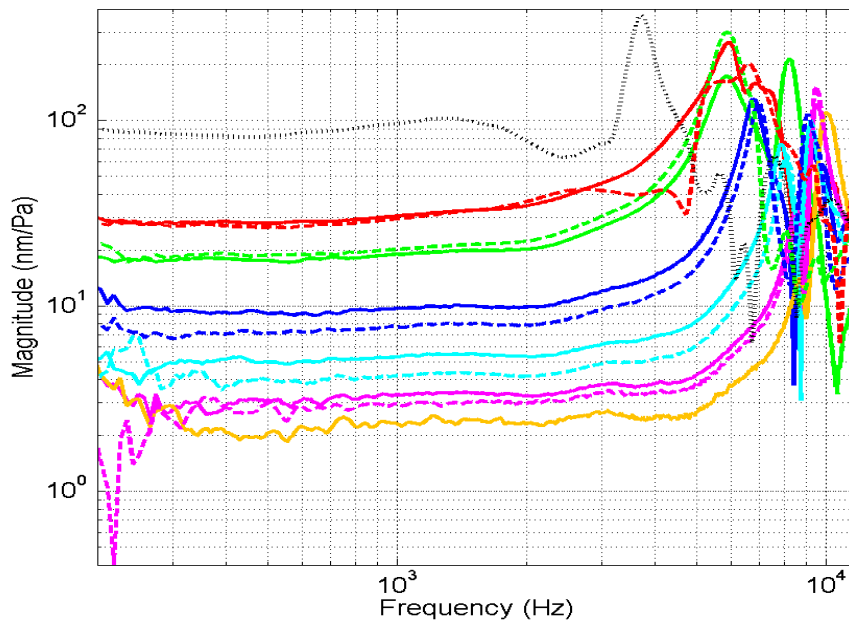
Figure 5.29: Effect of static pressurization during the negative-pressure sweep of cycle 1 on the pars tensa in gerbil H. Colours and line styles are the same as for Figure 5.25.
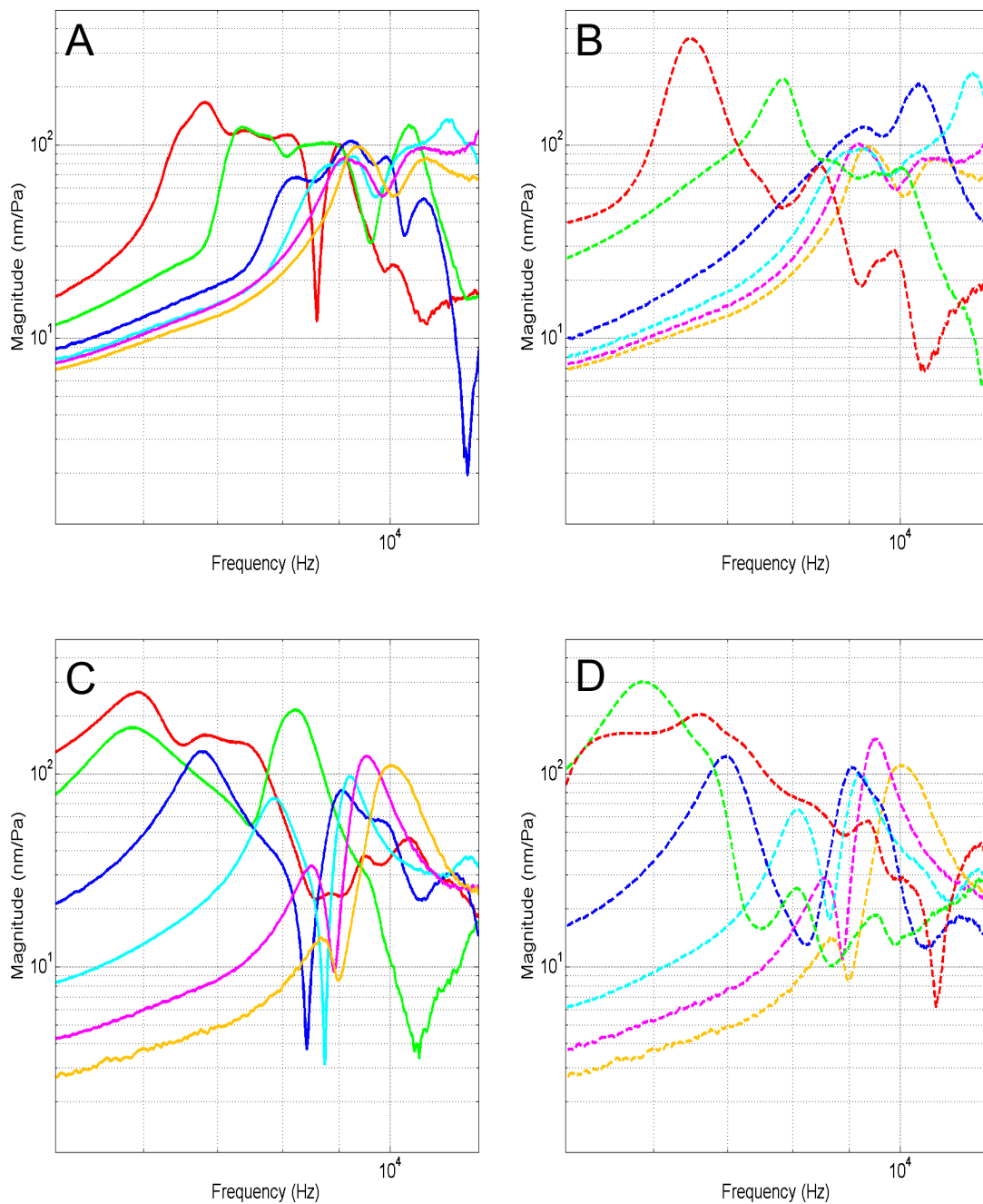
Figure 5.30: Pressurized responses recorded on the pars tensa of gerbil H on a frequency scale from 5 to 11 kHz. (A) Positive-pressure loading responses. (B) Positive-pressure unloading responses. (C) Negative-pressure loading responses. (D) Negative-pressure unloading responses.

is not clear whether the peak at 5.8 kHz on the green curve corresponds to the shoulder at 5.3 kHz on the red curve or to the peak at 6.3 kHz. Recall that for negative pressures in gerbil D we observed two distinct peaks, and the magnitude of the first peak decreased as pressures increased. A similar phenomenon is observed in gerbil H: for pressures of −1000 Pa or greater, we observe that the magnitude of the first peak (6.8 kHz at −1000 Pa) decreases with pressure while the magnitude of the second peak (9 kHz at −1000 Pa) remains relatively stable. A suggested hypothesis for this phenomenon is discussed in Section 5.5.

Figure 5.31 summarizes the results from all three pressure cycles in gerbil H. The figure is in the same format as Figure 5.26 but the data are for 1.5 kHz rather than 2 kHz. (Unlike the case for gerbil E, we do not observe any humps at 1.5 kHz in the pressurized responses in gerbil H so we go back to using this frequency for the analysis, as we did for protocol 1). We observe that the magnitude differences between the loading and unloading curves are the same in all three cycles. Compared with gerbil E on the manubrium (Figure 5.26), the degree of asymmetry between the curves for positive and negative pressures is reduced but still evident. Comparing all three cycles in panel D, we see that, on the positive-pressure side below +1000 Pa, the magnitudes of the loading parts are almost identical in cycles 2 and 3 but greater than in cycle 1, and that the unloading parts are almost identical in all three cycles. This suggests that something in the system changed during the first loading cycle. On the negative-pressure side, we see that the shapes of the first and second cycles are similar, and that the shape of the third cycle exhibits an upward bulge between −2000 and −1000 Pa. Beyond −250 Pa, the magnitudes tend to increase from cycle to cycle. The magnitude of the unpressurized measurement at the end of each cycle decreases as the experiment progresses, associated with values of 98.8, 83.4 and 43.6 nm/Pa for cycles 1, 2 and 3, respectively. This phenomenon is illustrated more clearly in the inset in panel D, with arrows corresponding to magnitudes at the end of the first and second cycles.
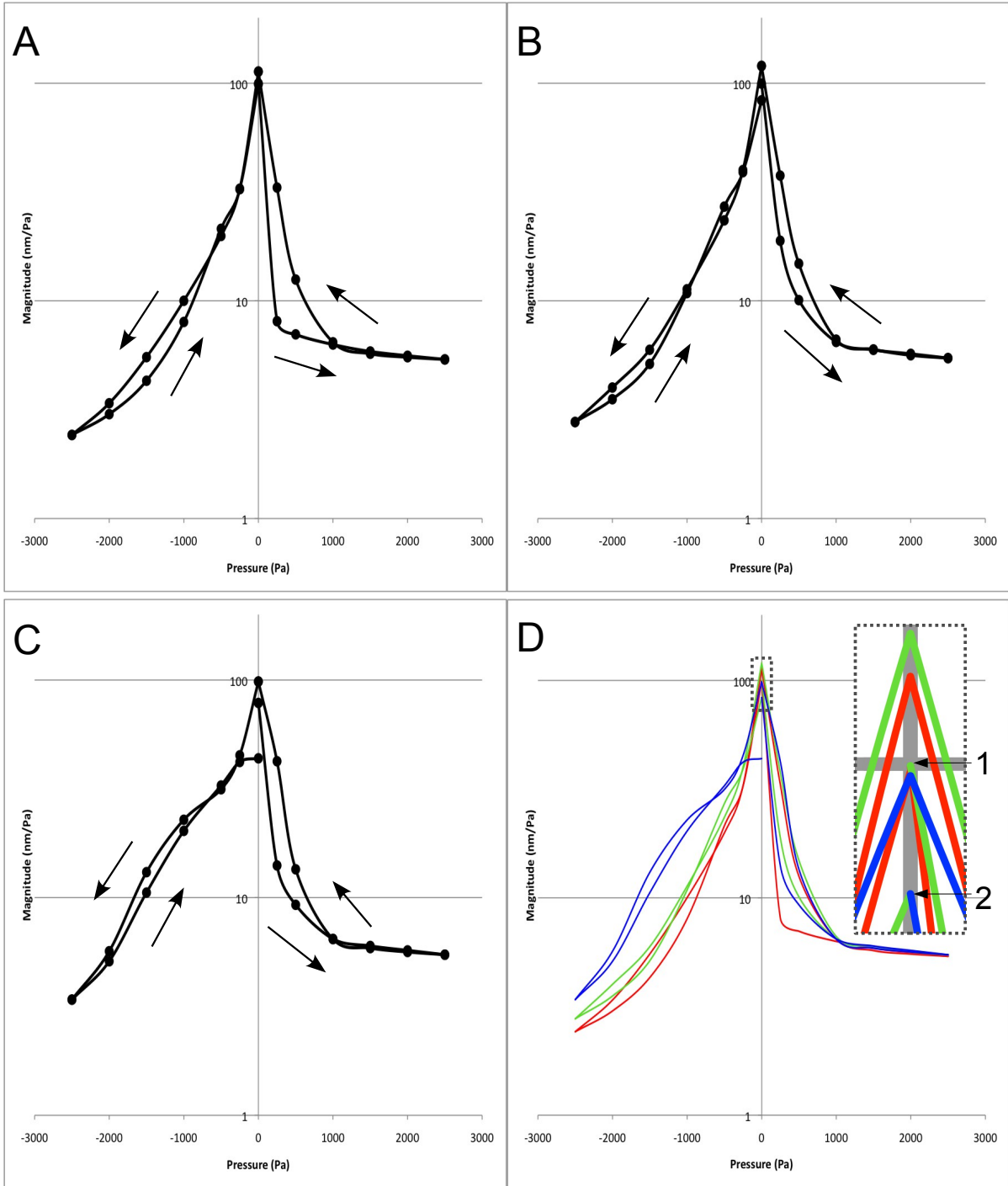
Figure 5.31: Magnitudes of vibration recorded on the pars tensa in gerbil H at a frequency of 1.5 kHz for cycles 1,2 and 3 are shown in panels A,B and C, respectively. The curves from each panel are superimposed in panel D with red, green and blue corresponding to the curves in panels A, B, and C, respectively. A magnified inset showing the curves near 0 Pa is shown in panel D, with arrows corresponding to magnitudes at the end of the first and second cycles.

Figure 5.32 displays how the unpressurized responses for the pars tensa of gerbil H evolve over the duration of the experiment. The colour sequence and the approximate times of the measurements are the same as in Figure 5.27 for the manubrium. The differences among the frequency responses are generally within 5 dB except at the sharp features, where the differences are much larger. At the peak due to the pars flaccida, we first observe a leftward frequency shift of 1.6 Hz/min between the black and red curves, followed by a rightward frequency shift of approximately 2 Hz/min between the red and blue curves. We observe a peak at 6.5 kHz and a trough at 8.5 kHz that shift by less than 0.5 kHz from response to response.
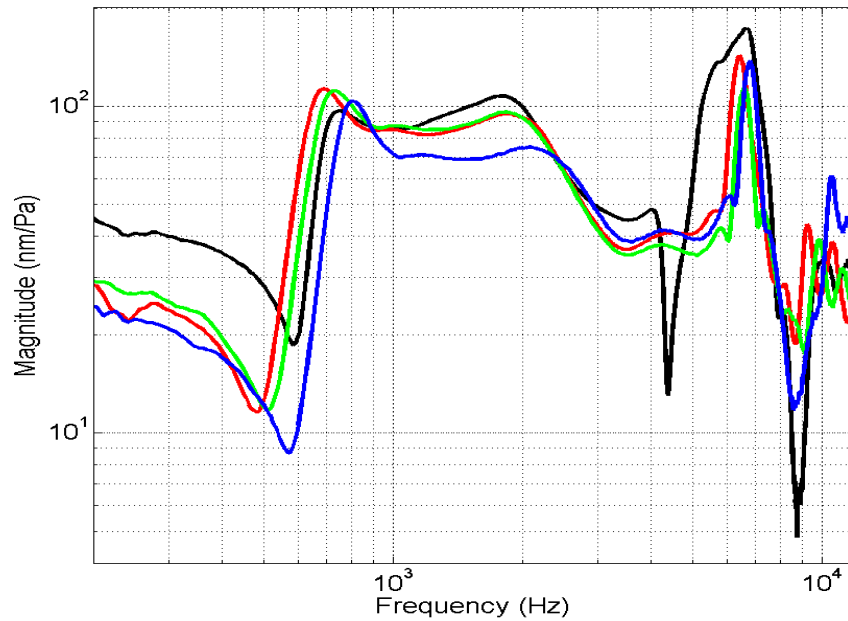
Figure 5.32: Unpressurized measurements on the pars tensa of gerbil H recorded over the course of the experiment. The colour sequence is the same as for Figure 5.27.

5.4.4 Responses in gerbils F and G

As mentioned in Chapter 4, complications during the experiments in gerbils F and G led to increased preparation times. The frequency responses of these gerbils are similar to those recorded in gerbil H (discussed in Section 5.4.3), with the exception of certain anomalous features that are especially evident after the first pressure cycle: we present the pressure sweeps of the second cycle for each gerbil and focus on the anomalies in the following paragraphs.

The frequency responses recorded during the positive-pressure sweep of the second cycle in each of gerbils F and G are presented in Figures 5.33 and 5.34, respectively. They are in the same format as for Figure 5.28 except that the upper limit of the magnitude range is increased to 800 nm/Pa. In both gerbils, high peaks are observed between 3 and 4 kHz during the unloading part of the sweep at pressures of +500 Pa and +250 Pa as well as during the subsequent unpressurized measurement. Similar peaks (although smaller and at higher frequencies) are visible in gerbil F at +1000 Pa during the unloading part (blue dashed curve) as well as in gerbil G at +250 Pa and +500 Pa during the loading part (red and green solid curves). Such peaks are not observed in the corresponding responses of gerbil H.

The frequency responses recorded during the negative-pressure sweep of the second cycle in each of gerbils F and G are presented in Figures 5.35 and 5.36, respectively, in the same format as for Figure 5.33. In both gerbils, peaks with high magnitudes are observed between 4 and 5 kHz during the loading part of the sweep at −250 Pa in the second cycle, and it was still there in the third cycle. A similar anomalous peak occurred at −500 Pa between 5 and 6 kHz during the third pressure cycle in gerbil G. Although the preparation times in both of these animals were unusually long, we cannot say for certain whether this is the primary cause of the anomalous behaviours.
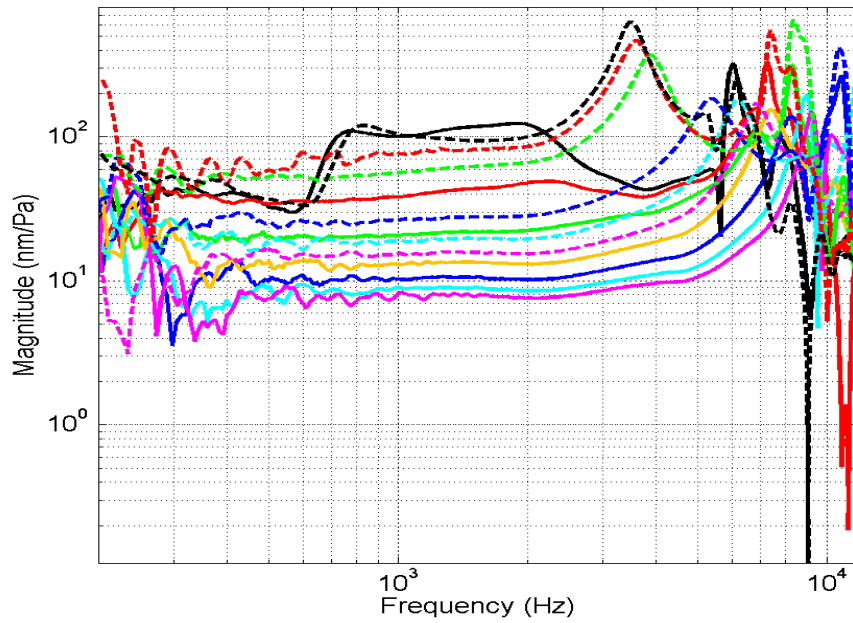
Figure 5.33: Effect of static pressurization during the positive-pressure sweep of the second cycle in gerbil F. Colours and line styles are the same as for Figure 5.28.
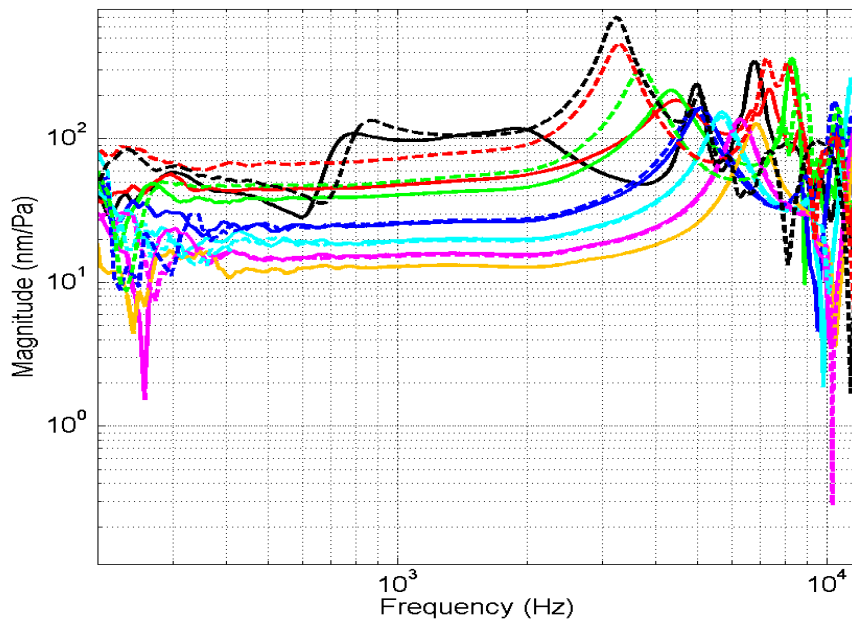
Figure 5.34: Effect of static pressurization during the positive-pressure sweep of the second cycle in gerbil G. Colours and line styles are the same as for Figure 5.28.
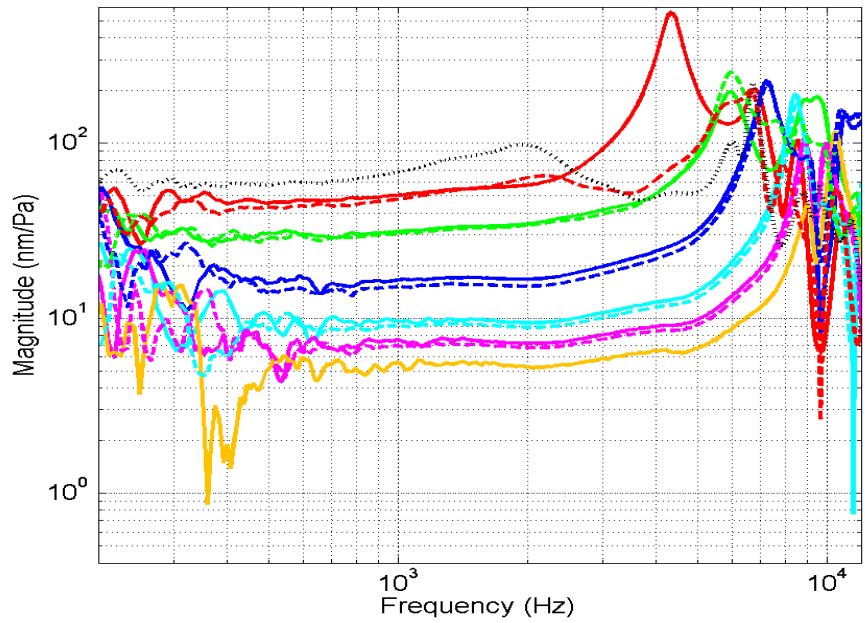
Figure 5.35: Effect of static pressurization during the negative-pressure sweep of the second cycle in gerbil F. Colours and line styles are the same as for Figure 5.29.
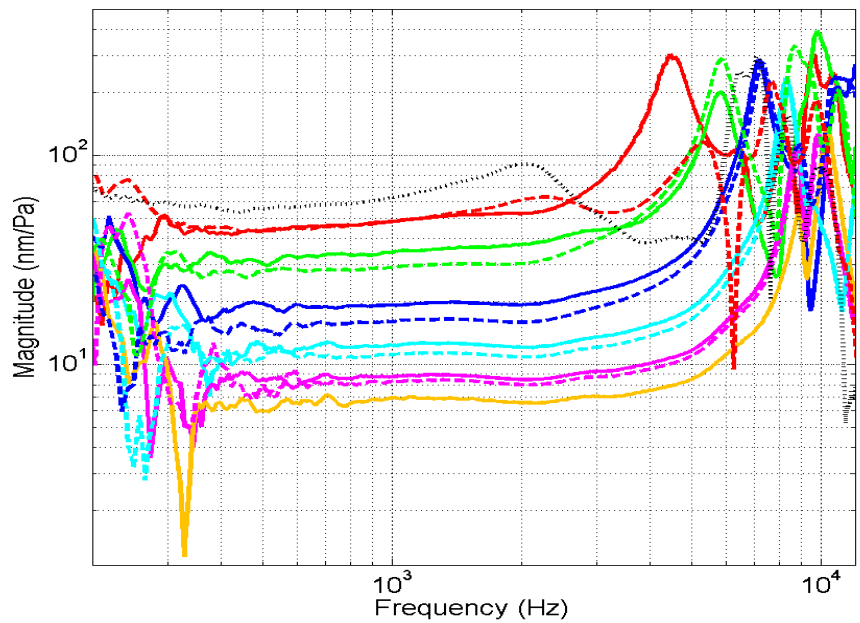
Figure 5.36: Effect of static pressurization during the negative-pressure sweep of the second cycle in gerbil G. Colours and line styles are the same as for Figure 5.29.

Figures 5.37 and 5.38 summarize the results at 1.5 kHz from all three pressure cycles on the pars tensa for gerbils F and G, respectively, in the same format as for Figure 5.31 (gerbil H). Compared with Figure 5.31, we generally see the same mostly small differences between loading and unloading cycles, the same degree of asymmetry, and the same trend of decreasing magnitudes of the final unpressurized response in each cycle (particularly evident between cycles 2 and 3 in gerbil G). We also see the same magnitude increase of the negative-pressure curves from cycle to cycle. During the positive-pressure sweep of gerbil F (Figure 5.37) there is a medium-size gap between the loading and unloading curves of the first cycle, then a very large gap in the second cycle and a very small gap in the final cycle. The sudden increase in magnitude that occurs between 2000 and 2500 Pa in the second cycle, together with the higher magnitudes in cycle 3, suggests that something changed in the system and stayed that way for the remainder of the experiment.

We also observe an abnormally low magnitude in gerbil F during the third cycle at +250 Pa of the loading part of the sweep. We see a similar feature in gerbil G (Figure 5.38) at the same pressure during the loading part of the first cycle. The feature is still visible during the second cycle although it is much less obvious; this suggests a transient change in the system.
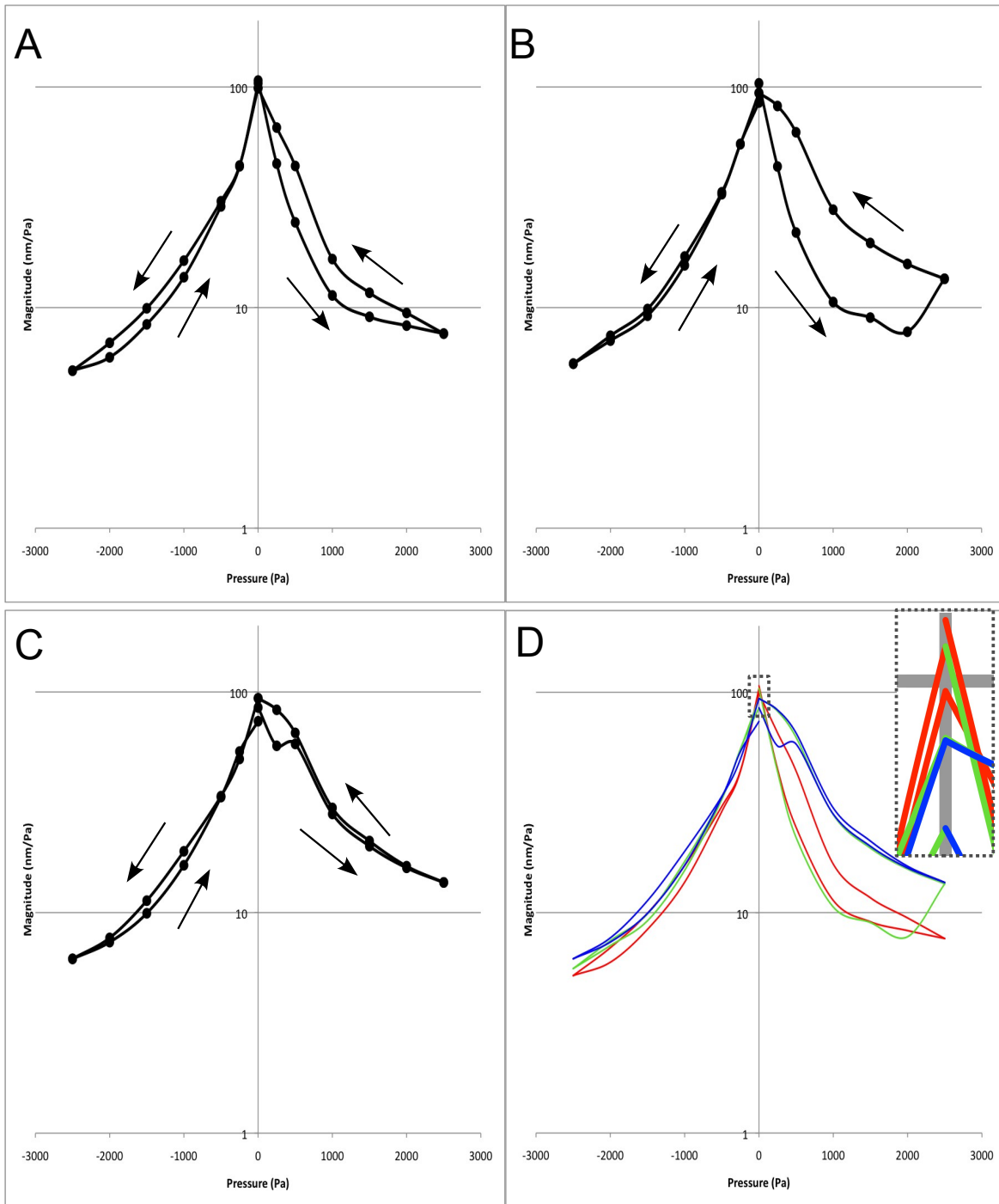
Figure 5.37: Magnitudes of vibration recorded in gerbil F at a frequency of 1.5 kHz for cycles 1,2 and 3 are shown in panels A, B and C, respectively. The colours in panel D are the same as for Figure 5.30. A magnified inset showing the curves near 0 Pa is shown in panel D.
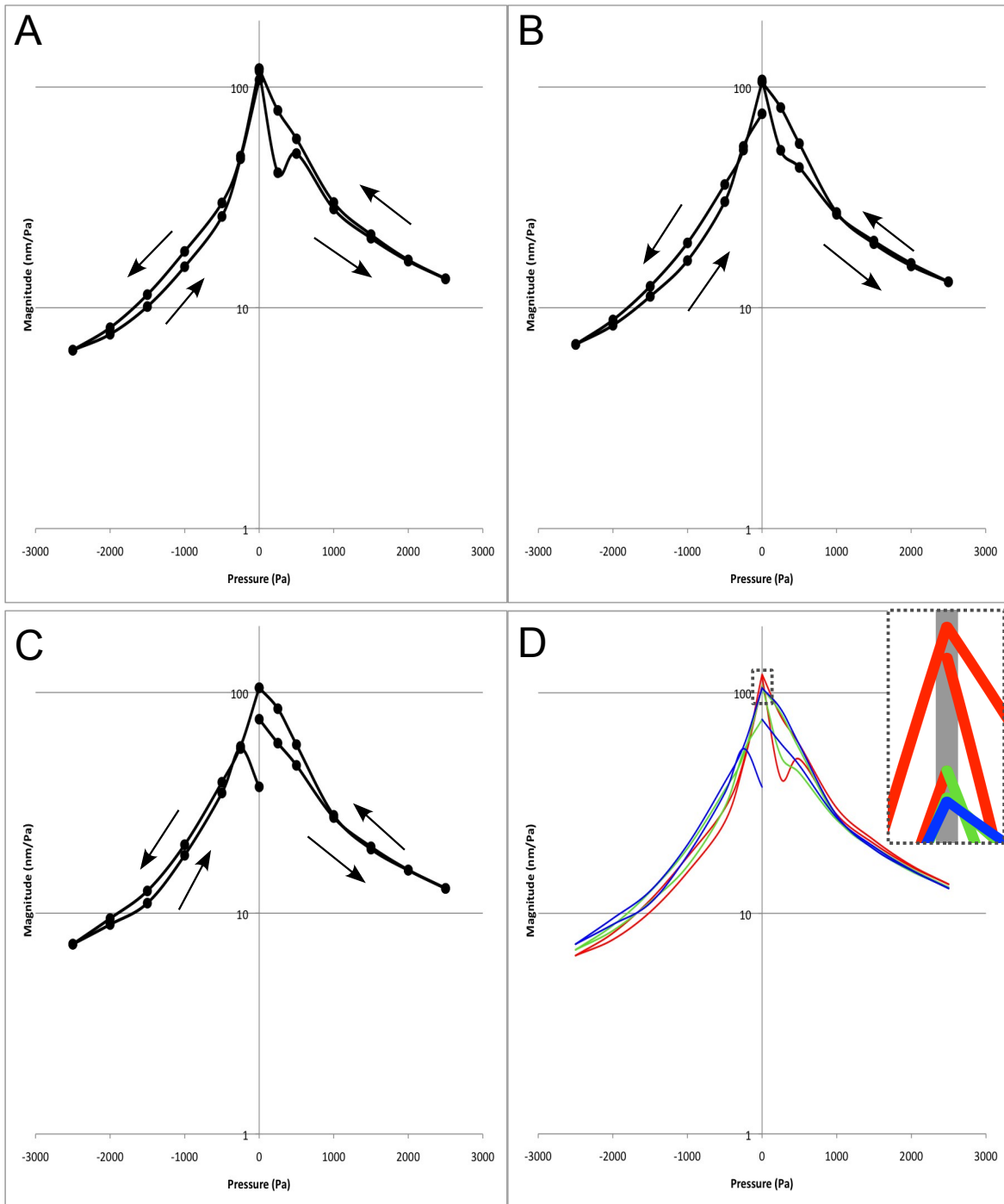
Figure 5.38: Vibration magnitudes recorded in gerbil G at a frequency of 1.5 kHz for cycles 1,2 and 3 are shown in panels A,B and C, respectively. The colours in panel D are the same as for Figure 5.30. A magnified inset showing the curves near 0 Pa is shown in panel D.

5.5 Discussion

In both protocols of this study, we investigate the effects on eardrum vibrations when static pressures are applied to the middle-ear cavity. Based on our results from protocol 1 (Figures 5.4–5.9), we conclude that we have good short-term repeatability over the 10–12 minute timespan of each pressure cycle. In particular, the repeatability of unpressurized responses suggests that the observed irregularities at high frequencies are not just due to high-frequency noise, a conclusion also reported in many previous studies (e.g., Maftoon et al. 2013). A positive-pressure sweep or a negative-pressure sweep in protocol 2 is performed over a timespan of just over 10 minutes. Based on our conclusions from protocol 1, we can therefore presume that the system is generally stable over that period of time, and that observed changes are not due to experimental artefacts like dehydration. For protocol 2 on the manubrium (gerbil E, Figures 5.24–5.25), we observe small but repeatable differences between the loading and unloading parts of each pressure sweep. We therefore suggest that in that experiment we also had good repeatability over the period of nearly 20 minutes required for the measurements in a pressure sweep. For protocol 2 on the pars tensa (gerbils F, G and H, Figures 5.28–5.29 and 5.33–5.36), however, we do not have long-term repeatability from cycle to cycle over the course of the experiment. However, the claims for short-term repeatability still seem to be valid: in gerbil F, nearly identical responses were obtained following an abrupt change of some kind after the first pressure cycle (Figure 5.37), thus suggesting good repeatability except for that change. In gerbil H, (Figure 5.31) the system changed in a systematic fashion, consistent with a long-term drift as opposed to a sudden change.

As shown in previous studies (e.g. Dirckx & Decraemer 2001), the displacement of the eardrum is a non-linear function of pressure. We report in our study that the vibration magnitude response is also a non-linear function of pressure. The slope of the magnitude-pressure curve is greatest near 0 Pa, decreasing strongly near the pressure extremes where the curves level off. The overall shape is similar to that of tympanograms (e.g.,

Figure 3.14), which is to be expected since tympanometry effectively measures a spatial integration of pressurized vibrations.

We observed that pressurized magnitudes on the manubrium were reduced at low frequencies, and that at higher frequencies the responses rise to a peak. Gan et al. (2006) and Homma et al. (2010), in their laser Doppler vibrometer measurements at the umbo in human temporal bones, also observed that vibration magnitudes were reduced at lower frequencies when the pressure was increased, with smaller reductions at higher frequencies. We observed that negative-pressure magnitudes on the manubrium were smaller than positive-pressure magnitudes. However, both Gan et al. (2006) and Homma et al. (2010) reported that magnitude reductions on the umbo for positive and negative pressure were similar. We observed that positive-pressure magnitudes on the pars tensa were generally smaller than negative-pressure magnitudes. This difference from the manubrium might be because the pars tensa is directly affected by the changes to its curvature that are caused by pressurization, while the manubrium is more directly affected by the ossicular chain.

We observed a shift of the peak in the magnitude response to higher frequencies with an increase in pressure. Similar shifts were observed by Gan et al. (2006) and Homma et al. (2010). We observe for protocol 1 that the peaks and troughs in the pressurized responses of the pars tensa also appear, within about 1 kHz, in the pressurized responses of the manubrium for a given pressure. This means that, over the frequency range of our results, in the presence of a static pressure, even one as small as ±250 Pa, the pars tensa appears to still be vibrating in its simple mode and the manubrium is following it. We conclude that by applying a static pressure and stiffening the membrane, we are pushing the vibration-pattern break-up to frequencies above the observable range in our study (11 kHz).

As discussed in Section 5.3.2 (Figure 5.20), there are multiple peaks in the pressurized responses in the frequency range from 6 to 11 kHz. We suggest that the first two peaks correspond to (1) the first resonance of the pars tensa (PTR), and (2) the first ossicular-

chain resonance (OCR). We cannot immediately say which peak is which. We hypothesize that at zero pressure the two resonances occur at approximately the same frequency and thus appear as a single resonance due to the broad nature of the peak. As pressure is applied, the first resonance of the eardrum and the first resonance of the ossicular chain presumably respond differently and therefore end up at different frequencies. In order to provide insight into the mechanisms that function in the ear upon exposure to intense sounds, Price & Kalb (1991) developed "time and frequency domain mathematical models of the ear including significant nonlinearities in the middle ear." They concluded that the nonlinearity in the middle ear was primarily due to the annular ligament of the stapes footplate. If that is true, then, although both the pars tensa and the ossicular chain will stiffen from pressurization, the ossicular chain will be affected more strongly due to the annular-ligament nonlinearity, resulting in a larger frequency shift. The results of Dirckx et al. (2006) appear to support the conclusion of Price & Kalb, but the results of Dirckx & Decraemer (2001) indicate that the stapedial nonlinearity does not influence the vibrations of the manubrium very much. In any case, different parts of the middle ear can be expected to respond to static pressures in different ways, thus causing their resonances to shift by different amounts.

As discussed in Chapter 3, von Unge et al. (1993) measured the shape of the eardrum in response to static pressure variations. They were the first group to discuss the viscoelasticity of the eardrum in terms of hysteresis and preconditioning. Later, other studies (e.g., Funnell & Decraemer 1996; Dirckx & Decraemer 2001, Ladak et al. 2004) demonstrated these two viscoelastic effects increasingly clearly. We discuss each effect in the following paragraphs, with emphasis on their presence in our study.

As discussed in Section 3.4, hysteresis in pressure-displacement plots involves unloading curves that have greater displacements than the loading curves. In protocol 2 of our study, we observe that the unloading curves are smaller for negative pressures but larger for positive pressures. We conclude that these differences in the magnitudes of vibration are

probably an indirect effect of the hysteresis affecting the underlying static displacements of the eardrum. It is difficult to predict the details of how the hysteresis should affect the vibration magnitudes because of the interplay between geometric non-linearities and material non-linearities (e.g., Ladak et al. 2006). For negative middle-ear pressures, the geometric effects are more complicated than for positive pressures because of a reversal of the direction of the curvature of the pars tensa and possible snap-through buckling (Ladak et al. 2004).

In protocol 1, we would expect the effects of hysteresis to appear in the unpressurized measurements immediately following positive or negative middle-ear pressures. Based on the moiré results presented in Section 3.4, the unpressurized deformations should be non-zero and therefore the magnitudes after both positive and negative middle-ear pressures would be expected to be different. Again, it is difficult to predict these magnitudes in detail. However, as shown in Figures 5.4 to 5.9 for the manubrium and in Figures 5.14 to 5.19 for the pars tensa, the unpressurized measurements are repeatable to within 1.5 dB in each pressure cycle for all animals, so there is no evidence of hysteresis, in contrast to protocol 2. This is presumably due to the particular sequence of measurements, although the reason is not clear.

In a viscoelastic material repeated loading and unloading curves will generally change from cycle to cycle but converge to a repeatable loop. As discussed in Section 3.4, this process is defined as preconditioning and has been reported in multiple studies. At the same time, however, we are also dealing with possible time-dependent changes of middle-ear components. Especially in *post mortem* studies, measurements can be affected by the dehydration or other degradation of middle-ear structures, and that can lead to changes in the material properties of the eardrum or middle-ear ligaments (e.g., Dirckx & Decraemer 2001; Ellaham 2007). As discussed in nearly all of the studies presented in Section 3.4, any differences that we observe between the responses from cycle to cycle may result from two possible sources: (1) the phenomenon of preconditioning, or (2) temporal effects such as

tissue dehydration and degradation over the course of the experiment. The lack of differences from cycle to cycle in gerbil E suggests that there is neither preconditioning nor *post mortem* change. The reason for this long-term repeatability could be that middle-ear tissues (at least *post mortem* ones) do not normally require preconditioning. In gerbils F, G and H, however, there are changes observed from cycle to cycle, but it is clear that these changes are not due to preconditioning, given that the changes are not gradual and the responses do not converge. It is possible that some of the odd behaviour on the pars tensa is either due to experimental artefacts, such as the accumulation of middle-ear liquid that may contact the eardrum (especially during pressurization), or due to instabilities of the eardrum that do not occur on the manubrium. Recall that, in their tympanometric measurements performed in cats, Osguthorpe & Lam (1981) observed notches in the ascending runs of the tympanogram curves. In our study, we observe notches in one ascending run each in gerbils F and G; we suggest that these phenomena may be related.

CHAPTER 6
CONCLUSION

6.1 Summary

In this study, vibration displacement responses on the manubrium and the pars tensa have been investigated with the aim of enhancing our understanding of the mechanics of the gerbil middle ear under static pressurization. First, we made a number of modifications to an existing pressurization device in order to accurately establish known static pressures in the gerbil middle ear. We also designed and manufactured a new coupler that improved upon the design of the previous coupler used in our lab. The new coupler featured an angled glass window to reduce residual laser-beam reflections; a conical shape to make the outer edges of the eardrum visible; and a threaded base to facilitate removal and replacement of the coupler. *Post mortem* frequency responses were then obtained using single-point LDV and were presented over the frequency range between 0.2 and 10 or 11 kHz. All responses were normalized with respect to sound pressure level in front of the eardrum.

For each gerbil we presented *post mortem* magnitude and phase frequency responses of the first unpressurized measurement on the manubrium and pars tensa as well as the first pressurized measurement. Our unpressurized results matched fairly well with the *in vivo* results reported by Maftoon et al. (2013). We found that the inter-specimen variability was small and that measurements were more or less repeatable from cycle to cycle.

Two protocols were used in this study: the first was used in gerbils A to D and consisted of cycles of alternating unpressurized and pressurized measurements at multiple pressure levels. Each pressure cycle was performed first on the manubrium and then on the pars tensa. The second protocol was used in gerbils E to H and consisted of three cycles that each included a positive and a negative pressure sweep. Only the manubrium was measured in gerbil E and only the pars tensa was measured in gerbils F to H. In each protocol we

studied the effects of static pressurization on the vibration response. In protocol 1, similar magnitude trends were observed in the frequency responses of each gerbil. Generally, the pressurized responses were characterized by gently increasing curves over the low-to-mid frequency range with no pars-flaccida features, rising to a peak and exhibiting sharp features at high frequencies. The measurements were quite repeatable over time. As the pressure increased, we observed that the magnitudes decreased over the low-to-mid frequency range and that the peak was shifted to higher frequencies. We also compared the higher-frequency features on the manubrium and pars tensa and concluded that the break-up frequency had been shifted to a frequency beyond the observable range of our measurements.

We also observed in protocol 1 that the pars-flaccida features were not apparent in the pressurized magnitude responses. The magnitude response was a non-linear function of pressure, with the largest slopes near 0 Pa, decreasing strongly near the pressure extremes where the curves levelled off. At pressures greater than ±500 Pa on the manubrium and greater than ±1000 Pa on the pars tensa, the responses were asymmetrical: the magnitudes of the responses recorded with positive middle-ear pressures were larger than those recorded with negative middle-ear pressures. The features of the pressurized responses shifted to higher frequencies with an increase in pressure. These observations also apply to the results of protocol 2.

For each pressure cycle of protocol 2, larger magnitudes were observed during the loading part of the positive-pressure sweep and during the unloading part of the negative-pressure sweep. In gerbil E (on the manubrium) we observed good repeatability between the pressure-magnitude responses of each cycle, indicating an absence of preconditioning and *post mortem* changes. In gerbils F, G and H (on the pars tensa), changes were observed from cycle to cycle. It is difficult to conclude whether these differences were a result of preconditioning, dehydration, or some other mechanism. A large change was observed during cycle 2 in gerbil F between 2000 and 2500 Pa of the positive pressure sweep

(Figure 5.37); it is not clear what caused the change but we concluded that it was not due to viscoelastic effects.

6.2 Future work

An important extension of our study would be to perform pressurized measurements at very low pressures, near 0 Pa. This would be useful for three main reasons:

1. We observed a number of oddities near zero pressure. For example, there is a notch in gerbil F during cycle 3 at 250 Pa (Figure 5.37), a notch in gerbil G during cycle 1 at 250 Pa (Figure 5.38), and a sharp drop in gerbil G at the end of cycle 3 (Figure 5.38). It would be useful to more closely investigate any possible further oddities that might occur near zero pressure.

2. We conclude in this study that, even for the lowest static pressures that we investigated, the break-up frequency of the pars tensa was shifted beyond the observed frequency range. It would be interesting to investigate the details of this shift, including how the particular response features change their relative amplitudes as they get pushed to higher frequencies.

3. It would be useful to determine the pressure at which the pars-flaccida effect disappears from the manubrium and pars-tensa frequency responses. Although this may not be important for clinical applications (the human eardrum has a relatively small pars flaccida), part of the rationale for studying the gerbil is to build confidence in our ability to explain and model the behaviour of the middle ear.

With our protocol 1 we were able to take measurements on both the manubrium and the pars tensa in the same animal. With protocol 2 this was not possible but the protocol had the advantage of matching the pressurization protocol used by Decraemer's group in their moiré measurements, so that we can use their results in the interpretation and modelling of

our results. For future work it will be important to also use a protocol that involves pressure sweeps similar to those used in clinical tympanometry. However, there would be an additional challenge because we would need to track the large movements of the eardrum as the pressure changes. In addition, we would need to redesign the pressurization system to avoid contamination of the measured signals by noise from the motor and pump. One possibility for reducing noise might be to operate the motor at lower speeds.

As discussed in Section 5.5, we provide a hypothesis for the frequency shifts and changes of relative magnitudes of the first two resonances in the pressurized pars-tensa responses. Our hypothesis could be investigated by, for example, immobilizing the ossicular chain during measurements (e.g., Ladak et al. 2004).

It would be useful to include more repetitions of pressurized measurements in the low-pressure cycles of protocol 1. An error of approximately ±10 Pa in the establishment of static pressures has a larger effect at low pressures than at higher pressures. The acquisition of more than two pressurized measurements in each cycle would allow us to more easily identify an anomalous response.

A very important extension of our study would be to perform the measurements *in vivo* in order to minimize the temporal effects associated with collecting measurements in a *post mortem* specimen. It would help us draw more definitive conclusions related to longer-term viscoelastic effects observed over the course of the experiment, given that we could perform more cycles of protocol 2. It would be necessary to use a larger number of animals in order to better determine the repeatability of various features that have been observed.

The possible hysteresis and preconditioning findings in protocol 2 of our study, as well as in previous studies, suggest that the mechanical properties of the eardrum at any given time are affected by the pressure loading and unloading history. Indeed, it is a well-known fact that the results of tympanometry measurements vary according to the pressure load history (e.g., Osguthorpe & Lam 1980). For future studies, we emphasize the importance of strictly

following the same protocol in each specimen, including the order and the time sequence of pressurized measurements, in order to make the data more reliable. In some previous reports there is no indication that the same time sequence was followed for each pressure cycle throughout the experiment. We also stress the importance of adhering to the same protocol in multiple studies, so that we can justifiably compare the results. More work is required to determine which protocols are appropriate for various experimental situations.

It would also be interesting to investigate the underlying phenomenon causing the anomalous responses observed in gerbils B, F, and G, where preparation times were longer. One hypothesis is related to buckling, either snap-through (a reversal of curvature, as discussed by Ladak at al. 2004) or wrinkling. We speculate that, during the negative-pressure sweep in these gerbils, the eardrum may start to buckle. After an extended period of time following the sacrifice of the gerbil, the condition of the eardrum has presumably deteriorated somewhat and it may be more vulnerable to this buckling effect. However, buckling may be inevitable as the pars-tensa curvature reverses. We could try to investigate these hypotheses by verifying whether the phenomenon is ever observed in *in vivo* measurements.

It would be useful to perform pressurized vibration measurements of the eardrum at more locations. To accomplish this, we suggest using multi-point LDV (e.g., Maftoon 2013), applying multiple beads or reflective coatings (such as ink or silver powder) to the surface of the eardrum. However, especially in *post mortem* studies but also in *in vivo* ones, the middle ear is susceptible to drying and other changes, and time constraints such as the need to refocus when pressurizing limits the total number of measurements that we can obtain over the course of an experiment. Possible solutions include refocusing automatically using stepper motors to drive an *x-y-z* positioning system (Decraemer et al. 2007), as well as other vibration measurement techniques such as scanning LDV and holography. A complementary approach is to measure acoustic input admittance as a method of characterizing eardrum behaviour. This could be done in the same ears as the LDV

measurements. It would provide information about the entire eardrum and would also be directly comparable to the tympanometry data in the literature.

In the future, modelling will be an important tool that will help us better understand the changes that occur because of viscoelastic effects, and finite-element models will be particularly useful. More work is required to combine various features of existing models. However, modelling eardrum vibrations in response to pressurization is challenging because both geometric and material changes are occurring simultaneously and a wide range of time constants is involved.

Ultimately, our study indicates that more work is needed to clarify the response of the eardrum to pressurization, as well as the roles of hysteresis, preconditioning and other temporal effects. This will lead to a better understanding of tympanometry, which is particularly important in infants where the response to tympanometry and therefore the assessment of middle-ear function are not well understood.

REFERENCES

Akache F, Funnell WRJ, & Daniel SJ (2007): An experimental study of tympanic membrane and manubrium vibrations in rats. *Audiology & Neuro-Otology* 12: 49–58.

Akinpelu OV, Peleva E, Funnell WRJ & Daniel SJ (2014): Otoacoustic emissions in newborn hearing screening: A systematic review of the effect of different protocols on test outcomes. *International Journal of Pediatric Otorhinolaryngology*, in press.

Allmen MV (1987): *Laser-bream interactions with materials*. Spring-Verlag, New York, NY.

Békésy G. von (1941): Über die Messung der Schwingungsamplitude der Gehörknöchelchen mittels einer kapazitiven Sonde. *Akustische Zeitschrift* 6: 1–16.

Békésy G. von (1949): The structure of the middle ear and the hearing of one's own voice by bone conduction. *The Journal of the Acoustical Society of America* 21: 217–232.

Békésy G. von (1960): *Experiments in hearing*. McGraw Hill, NY.

Beranek LL (1993): *Acoustics*. Acoustical Society of America, Woodbury, NY

Borg E & Counter SA (1989): The middle-ear muscles. *Scientific American* 261: 74–80.

Charlebois M, McKee MD & Buschmann MD (2004): Nonlinear tensile properties of bovine articular cartilage and their variation with age and depth. *Journal of Biomechanical Engineering* 126: 129–137.

Cheng JT, Aarnisalo AA, Harrington E, Hernandez-Montes MS, Furlong C, Merchant SN & Rosowski JJ (2010): Motion of the surface of the human tympanic membrane measured with stroboscopic holography. *Hearing Research* 263: 66–67.

Cheng JT, Dai C & Gan RZ (2007): Viscoelastic properties of human tympanic membrane. *Annals of Biomedical Engineering* 35: 305–314.

Cohen YE, Doan DE, Rubin DM & Saunders JC (1993): Middle-ear development. V: Development of umbo sensitivity in the gerbil. *American Journal of Otolaryngology* 14: 191–198.

Dahmann H (1930): Zur Physiologie des Hörens- experimentelle Untersuchungen über die

mechanik der Gehörknöchelchenkette, sowie über deren Verhalten auf Ton und Luftdruck. *Zeitschrift für Hals Nasen Ohrenheilkunde* 27: 329–367.

Decraemer WF, de La Rochefoucald O, Dong W, Khanna SM, Dirckx JJJ & Olson ES (2007): Scala vestibuli pressure and three-dimension stapes velocity measured in succession in gerbil. *The Journal of the Acoustical Society of America* 121: 2774–2791.

Decraemer WF & Khanna SM (1994): Modelling the malleus vibration as a rigid body motion with one rotational and one translational degree of freedom. *Hearing Research* 72: 1–18.

Decraemer WF & Khanna SM (1997): Vibrations on the malleus measured through the ear canal. *Proceedings of Middle Ear Mechanics in Research and Otosurgery.* Dresden, 32–39.

Decraemer WF, Khanna SM & Funnell WRJ (1989): Interferometric measurements of the amplitude and phase of tympanic membrane vibrations in cat. *Hearing Research* 38: 1–17

Decraemer WF, Khanna SM & Funnell WRJ (1991): Malleus vibration mode changes with frequency. *Hearing Research* 54: 305–318.

Decraemer WF, Khanna SM & Funnell WRJ (1994): A method for determining three-dimensional vibration in the ear. *Hearing Research* 77: 19–37.

Decraemer WF, Khanna SM & Funnell WRJ (1995): Bending of the manubrium in cat under normal sound stimulation. *Proceedings of Optical and Imaging Techniques in Biomedicine* 2329: 74–84.

Decraemer WF, Maes MA, Vanhuyse VJ, Vanpeperstraete (1980): A non-linear viscoelastic constitutive equation for soft biological tissues, based upon a structural model. *Journal of Biomechanics* 13: 559–564.

de La Rochefoucauld O & Olson ES (2010): A sum of simple and complex motions on the eardrum and manubrium in gerbil. *Hearing Research* 263: 9–15.

Dirckx JJJ, Buytaert JAN & Decraemer WF (2006): Quasi-static transfer function of the rabbit middle ear, measured with a heterodyne interferometer with high-resolution position

decoder. *Journal of the Association for Research in Otolaryngology* 7: 339–351.

Dirckx JJJ & Decraemer WF (1991): Human tympanic membrane deformation under static pressure. *Hearing Research* 51: 93–105.

Dirckx JJJ & Decraemer WF (1996): Reflective coatings in optical interferometry for *in vitro* studies of the eardrum. *Optical and Imaging Techniques for Biomonitoring II* 2927: 2–10.

Dirckx JJJ & Decraemer WF (2001): Effect of middle ear components on eardrum quasi-static deformation. *Hearing Research* 157: 124–137.

Dirckx JJJ, Decraemer WF, von Unge M & Larsson C (1998): Volume displacement of the gerbil eardrum pars flaccida as a function of middle ear pressure. *Hearing Research* 118: 35–46.

Dong W & Olson ES (2006). Middle ear forward and reserve transmission in gerbil. *Journal of Neurophysiology* 95: 2951-2961.

Elkhouri N, Liu H & Funnell WRJ (2006): Low-frequency finite-element modeling of the gerbil middle ear. *Journal of the Association for Research in Otolaryngology* 7: 399–411.

Ellaham N (2007): *An experimental study of middle-ear vibrations in gerbils*. Master's thesis, McGill University, Montréal.

Falk B (1982): Sniff-induced negative middle-ear pressure: study of a consecutive series of children with otitis media with effusion. *American Journal of Otolaryngology* 3: 155-62.

Finck A & Sofouglu M (1966): Auditory sensitivity of the mongolian gerbil (*Meriones unguiculatus*). *Journal of Auditory Research* 6: 313–319.

Fung YC (1996): *Biomechanics: mechanical properties of living tissues*. Springer-Verlag, NY.

Funnell WRJ (1996): Low-frequency coupling between eardrum and manubrium in a finite-element model. *The Journal of the Acoustical Society of America* 99: 3036–3043.

Funnell WRJ & Decraemer WF (1996): On the incorporation of moiré shape measurements in finite-element models of the cat eardrum. *The Journal of the Acoustical Society of America* 91: 2082-90.

Funnell WRJ, Khanna SM & Decraemer WF (1992): On the degree of rigidity of the manubrium in a finite-element model of the cat eardrum. *The Journal of the Acoustical Society of America* 91: 2082–2090.

Funnell WRJ & Laszlo CA (1982): A critical review of experimental observations on eardrum structure and function. *Journal for Oto-Rhino-Laryngology* 44: 181–205.

Gaihede M (1996): Tympanometric preconditioning of the tympanic membrane. *Hearing Research* 102: 28–34.

Gan RZ, Dai C & Wood MW (2006): Laser interferometry measurements of middle ear fluid and pressure effects on sound transmission. *The Journal of the Acoustical Society of America* 120: 3799–3810.

Gundersen T & Høgmoen K (1976): Holographic vibration analysis of the ossicular chain. *Acta Oto-Laryngologica* 82: 16–25.

Gyo K, Aritomo H & Goode RL (1987): Measurement of the ossicular vibration ratio in human temporal bones by use of a video measuring system. *Acta Oto-Laryngologica* 103: 87–95.

Hariharan P (2006): *Basics of interferometry, second edition* (2nd ed). Academic Press.

He Z (2012): *Vibration measurements on the widely exposed gerbil eardrum.* Master's thesis, McGill University, Montréal.

Helmholtz H (1869): *Die Mechanik der Gehörknöchelchen und des Trommelfells, Pflügers Archiv Physiol* (1st ed). Bonn. [English translations — (1) Bucks AH & Smith N (1873): The Mechanism of the Ossicles of the Ear and Membrana Tympani (Woods, New York), 69 pp. (2) Hilton J (1874): The Mechanism of the Ossicles and the Membrana Tympani (New Sydenham Society, London), 62: 97–155.]

Henry KR, McGinn, MD & Chole RA (1980): Age-related auditory loss in the Mongolian gerbil. *Archives of Oto-Rhino-Laryngology* 228: 233–238.

Homma K, Shimizu Y, Kim N, Du Y & Puria S (2009): Effects of ear-canal pressurization on middle-ear bone-and air-conduction responses. *Hearing Research* 263: 204–215.

Hunt RM & Korth WW (1980): The auditory region of dermoptera: Morphology and function relative to other living mammals. *Journal of Morphology* 164(2): 167–211.

Huttenbrink KB (1989): The mechanics of the middle eat at static air pressures. *Acta Oto-laryngologica* Supplement (Stockholm) 451: 1–35.

Joint Committee on Infant Hearing (2007): Principles and guidelines for early hearing detection and intervention programs. *Pediatrics* 120: 898–921.

Kessel J (1874): On the influence of the middle-ear muscles on the displacements and vibrations of the eardrum in the cadaver ear. *Archiv für Ohrenheilkunde* 8: 80–92 (in German).

Kobrak HG (1948) Construction material of the sound conduction system of the human ear. *The Journal of the Acoustical Society of America* 20: 125–130

Koike T, Wada H & Kobayashi T (2002): Modeling of the human middle ear using the finite-element method. *The Journal of the Acoustical Society of America* 111: 1306–1317.

Kuypers LC, Decraemer WF & Dirckx JJJ (2006): Thickness distribution of fresh and preserved human eardrums measured with confocal microscopy. *Otology & Neuro-Otology* 27: 256–264.

Kuypers W, Peters TA & Tonnaer ELGM (1999): Nature of the tympanic membrane insertion into the tympanic bone of the rat. *Hearing Research* 128: 80–88

Ladak HM, Decraemer WF, Dirckx JJJ & Funnell WRJ (2004): Response of the cat eardrum to static pressures: mobile versus immobile malleus. *The Journal of the Acoustical Society of America* 116: 3008-3021.

Ladak HM, Funnell WRJ, Decraemer WF & Dirckx JJJ (2006): A geometrically nonlinear finite-element model of the cat eardrum. *The Journal of the Acoustical Society of America* 119: 2859–2868.

Lay DM (1972): The anatomy, physiology, functional significance and evolution of specialized hearing organs of gerbilline rodents. *Journal of Morphology* 138: 41–120.

Lee CY, Rosowski JJ (2001): Effects of middle-ear static pressure on pars tensa and pars flaccida of gerbil ears. *Hearing Research* 153: 146–163.

Lim DJ (1968): Tympanic membrane part II.: pars flaccida. *Acta Oto-Laryngologica* 66: 512–532.

Luo H, Dai C, Gan RZ & Lu H (2009): Measurement of Young's modulus of human
tympanic membrane at high strain rates. *Journal of Biomechanical Engineering* 131,
064501

Maftoon N, He Z, Funnell WRJ & Daniel SJ (2012): Multiple-point vibration
measurements on the gerbil tympanic membrane. 35th Midwinter Research Meeting,
Association for Research in Otolaryngology, San Diego.

Maftoon N, Funnell WRJ, Daniel SJ & Decraemer WF (2013): Experimental study of
vibrations of gerbil tympanic membrane with closed middle-ear cavity. *Journal of
the Association for Research in Otolayngology* 14: 467–481.

Manley GA & Johnstone BM (1974): Middle-ear function in the guinea pig. *The Journal of
the Acoustical Society of America* 56: 571–576.

Motallebzadeh H, Charlebois M & Funnell WRJ (2013): A non-linear viscoelastic model
for the tympanic membrane. *Journal of the Acoustical Society of America* 134:
4427–4434.

Nambiar S (2010): *An experimental study of middle-ear vibrations in gerbils*. Master's
thesis, McGill University, Montréal.

Osguthorpe JD, Lam C (1980): Methodologic aspects of tympanometry in cats.
Otolaryngology--Head and Neck Surgery 89: 1037–1040.

Ravicz ME, Cooper NP & Rosowski JJ (2008): Gerbil middle-ear sound transmission from
100 Hz to 60 kHz. *The Journal of the Acoustical Society of America* 124: 363–380.

Ravicz ME & Rosowski JJ (1997): Sound-power collection by the auditory periphery of the
Mongolian gerbil *Meriones unguiculatus*: III. Effect of variations in middle-ear
volume. *The Journal of the Acoustical Society of America* 101: 2135–2147.

Ravicz ME, Rosowski JJ & Voigt HF (1992): Sound-power collection by the auditory
periphery of the Mongolian gerbil *Meriones unguiculatus*. I: Middle-ear input
impedance. *The Journal of the Acoustical Society of America* 92: 157–177.

Righini GC (2009): *An introduction to optoelectronic sensors*. World Scientific, Singapore.

Rosowski JJ, Cheng JT, Ravicz ME, Hulli N, Montes ME, Harrington E & Furlong C
(2009): Computer-assisted time-averaged holograms of the motion of the surface of

the mammalian tympanic membrane with sound stimuli of 0.4–25 kHz. *Hearing Research* 253: 83–96.

Rosowski JJ, Dobrev I, Khaleghi M, Lu W, Cheng JT, Harrington E & Furlong C (2013): Measurements of three-dimensional shape and sound-induced motion of the chincilla tympanic membrane. *Hearing Research* 301: 44–52.

Rosowski JJ & Lee CY (2002): The effect of immobilizing the gerbil's pars flaccida on the middle-ear's response to static pressure. *Hearing Research* 174: 183–195.

Rosowski JJ, Nakajima HH & Merchant SN (2008): Clinical utility of laser-doppler vibrometer measurements in live normal and pathologic human ears. *Ear and Hearing* 29: 3–19.

Rosowski JJ, Ravicz ME, Teoh SW & Flandermeyer DT (1999): Measurements of middle-ear function in the Mongolian gerbil, a specialized mammalian ear. *Audiology & Neuro-Otology* 4: 129–136.

Ryan A (1976): Hearing sensitivity of the mongolian gerbil, *Meriones unguiculatis*. *The Journal of the Acoustical Society of America* 59: 1222–1226.

Sadé J & Amos A (1997): Middle ear and auditory tube: middle ear clearance, gas exchange, and pressure regulation. *Otolaryngology -- Head and Neck Surgery* 116: 499–524

Teoh SW, Flandermeyer DT & Rosowski JJ (1997): Effects of pars flaccida on sound conduction in ears of Mongolian gerbil: acoustic and anatomical measurements. *Hearing Research* 106: 39–65.

Tondorf J & Khanna SM (1972): Tympanic-membrane vibrations in human cadaver ears studied by time-averaged holography. *The Journal of the Acoustical Society of America* 52: 1221–1233.

von Unge M, Bagger-Sjöbäack D & Brong E (1991): Mechanoacoustic properties of the tympanic membrane: a study on isolated mongolian gerbil temporal bones. *American Journal of Otology* 12: 407–419

von Unge M, Decraemer WF, Bagger-Sjöbäck D & Dirckx JJJ (1993): Displacement of the gerbil tympanic membrane under static pressure variations measured with a real-

time differential moire interferometer. *Hearing Research* 70: 229–242.

Webster DB & Webster M (1972): Kangaroo rat auditory thresholds before and after middle ear reduction. *Brain, Behavior and Evolution* 5: 41–53.

Wever EG & Lawrence M (1954): *Physiological acoustics*. Princeton University Press, Princeton, NJ.

Wever EG, Lawrence M & Smith KR (1948): The middle ear in sound conduction. *Archives of Otolaryngology* 48: 19–35.

Whittemore KR, Merchant SN, Poon BB & Rosowski JJ (2004): A normative study of tympanic membrane motion in humans using a laser Doppler vibrometer (LDV). *Hearing Research* 187: 85–104.

Yang, Xinming & Henson Jr. OW (2002): Smooth muscle in the annulus fibrosus of the tympanic membrane: physiological effects on sound transmission in the gerbil. *Hearing Research* 164: 105–114.

Zheng, Yulian, Ohyama K, Hozawa K, Hiroshi W & Tomonori T. (1997): Effect of anesthetic agents and middle ear pressure application on distortion product otoacoustic emissions in the gerbil. *Hearing Research* 112: 167–174.